Master's thesis

NTNU
Norwegian University of Science and Technology
Faculty of Engineering
Department of Marine Technology

Lars-Petter Solvang Johnsen

Spar Floating Wind Turbine Design Optimization with Concrete Substructures

Master's thesis in Marine Technology
Supervisor: Erin Bachynski-Polić and Peter Rohrer
June 2023

NTNU
Norwegian University of
Science and Technology

Lars-Petter Solvang Johnsen

Spar Floating Wind Turbine Design Optimization with Concrete Substructures

Master's thesis in Marine Technology
Supervisor: Erin Bachynski-Polić and Peter Rohrer
June 2023

Norwegian University of Science and Technology
Faculty of Engineering
Department of Marine Technology

NTNU
Norwegian University of
Science and Technology

NTNU Trondheim
Norwegian University of Science and Technology *Faculty of Engineering*
Department of Marine Technology

THESIS WORK SPRING 2023
for

Stud. Tech. Lars-Petter Solvang Johnsen

Spar floating wind turbine design optimization with concrete substructures
Designoptimering for spar-type flytende vindturbiner av betong

Initial designs and prototypes for floating wind turbines (FWTs) have largely assumed floating substructures made from steel. Recently, Equinor's Hywind Tampen project has departed from that trend and will use large concrete substructures to support 8 MW wind turbines. Some in the industry believe concrete substructures will be even more attractive to designers as wind turbine size increases further. Additionally, concrete structures can have a lower environmental impact, and satisfy potential local content requirements for floating wind farm construction.

This project will require updating an existing design optimization model to assume concrete substructures. This includes modification of the structural model and cost models, as well as consideration of updated objective and constraint functions for the optimization, especially related to fatigue.

1. Literature review into wave and wind loads, FWT dynamics, concrete platform design, and fatigue and extreme strength assessment for concrete structures.
2. Build two numerical models of each of the 10 MW concrete spars designed by Oh et al.: a numerical model in SIMA and in the linearized simplified analysis tool SparOpt based on Hegseth's PhD work.
3. Develop post-processing tools for fatigue and extreme load estimation for the tower and spar (concrete and reinforcement) based on time series of stress.
4. Compare the SIMA and SparOpt results for the different designs, and assess whether or not the SparOpt tool can capture important trends in the responses.
5. Carry out design optimization with a limited number of design variables using the SparOpt tool in order to assess the differences in optimal designs for concrete and steel spars.
6. Report and conclude on the investigation.

The work scope may prove to be larger than initially anticipated. Subject to approval from the supervisors, topics may be deleted from the list above or reduced in extent.

In the project report, the candidate shall present his personal contribution to the resolution of problems within the scope of the project work

Theories and conclusions should be based on mathematical derivations and/or logic reasoning identifying the various steps in the deduction.

The candidate should utilise the existing possibilities for obtaining relevant literature.

Project report format
The project report should be organised in a rational manner to give a clear exposition of results, assessments, and conclusions. The text should be brief and to the point, with a clear language. Telegraphic language should be avoided.

The report shall contain the following elements: A text defining the scope, preface, list of contents, summary, main body of thesis, conclusions with recommendations for further work, list of symbols and acronyms, references and (optional) appendices. All figures, tables and equations shall be numerated.

The supervisors may require that the candidate, in an early stage of the work, presents a written plan for the completion of the work.

The original contribution of the candidate and material taken from other sources shall be clearly defined. Work from other sources shall be properly referenced using an acknowledged referencing system.

The report shall be submitted in electronic format (.pdf):
- Signed by the candidate
- The text defining the scope shall be included (this document)
- Drawings and/or computer models that are not suited to be part of the report in terms of appendices shall be provided on separate (.zip) files.

Ownership
NTNU has according to the present rules the ownership of the project reports. Any use of the report has to be approved by NTNU (or external partner when this applies). The department has the right to use the report as if the work was carried out by a NTNU employee, if nothing else has been agreed in advance.

Thesis supervisors:

Prof. Erin Bachynski-Polić, NTNU, erin.bachynski@ntnu.no
PhD candidate Peter Rohrer, NTNU, peter.j.rohrer@ntnu.no

Deadline: June 11th, 2023, 14:00

Preface

This work presents my master thesis written at the Department of Marine Technology, Norwegian Institute of Science and Technology. It concludes my Master of Science degree within the specialization of Marine Structures, completed during the spring of 2023. The research conducted in this thesis builds upon a preparatory pre-project carried out during the fall of 2022, and it reflects my interest in offshore wind and the exploration of alternative construction materials.

I would like to express my sincere gratitude to my main supervisor, Erin Bachynski-Polić, for her valuable guidance and support throughout this research journey. Her expertise and insightful feedback have been important in shaping the direction of this thesis. Her dedication and unwavering commitment to my academic growth have been truly inspiring.

I would also like to extend my appreciation to my co-supervisor, Peter Rohere, a talented PhD candidate, for his constant availability and assistance. His technical expertise and willingness to lend a helping hand at every step have been immensely valuable. I am grateful for his countless hours discussing ideas, and problems, and providing constructive criticism.

Additionally, I would like to thank the faculty members and researchers at the Department of Marine Technology for creating a stimulating academic environment that fostered my growth. Their contributions and collaborations have been pivotal in shaping my understanding of marine structures and offshore wind technologies.

Lastly, I am thankful to my family and friends, who have supported and encouraged me throughout this academic endeavor. Their belief in my abilities has been a constant source of motivation.

I hope this thesis serves as a meaningful contribution to the field of marine technology, particularly in the context of offshore wind and alternative construction materials. It is my sincere wish that the findings presented herein inspire further research and innovation in this rapidly evolving field.

Abstract

This thesis explores the usefullness of incorporating concrete structures into an optimization model, based on two simplified spar structures developed by Oh et al. [55] to support a 10 MW DTU wind turbine [2]. These models are then incorporated in the linearized frequency domain model developed by Hegseth et al. [34]. A comprehensive analysis of several key aspects was conducted, by comparing the results from the nonlinear and linearized models, including natural periods, potential flow results, spectral comparisons, internal forces, concrete capacity, fatigue analysis, and design optimization using the OpenMDAO framework.

The investigation revealed distinctions between nonlinear and linearized models in terms of wave excitation and added mass effects. The SPAROpt models exhibited lower wave excitation in surge motion at higher wave frequencies, while pitch excitation was overestimated at lower frequencies. The larger spar showed greater damping due to its larger geometry. The constant wind test yielded promising results, with the rotor behaving as expected. The study conducted a decay test to evaluate the natural periods of surge, heave, pitch, and yaw motions. The flexible spar exhibited lower yaw natural periods due to variations in mass distribution. At the tower base, slight variations in the first pitch bending natural frequency were observed among the models.

Spectral comparisons were performed to assess the spectral density of SIMA and SPAROpt models under wave and wind conditions. While SPAROpt had limitations and tended to underestimate specific response parameters, the standard deviation of responses indicated that the relative strengths and variances within the frequency components were preserved. Notable discrepancies were observed in bending during the transition from concrete to steel, resulting in significantly larger excitation in SPAROpt. The analysis of internal forces provided insights into important trends and stresses. The ballast load influenced shear forces while bending moments exhibited expected behavior, with the highest bending moment occurring in the fairlead regions. Axial and shear stresses were affected by variations in thickness and geometric differences.

The concrete capacity assessment demonstrated satisfactory performance, with both SPAR 1 and Spar 2 maintaining ratios below the failure threshold. Short-term axial stresses remained within acceptable limits, and long-term axial stresses consistently remained below the allowable stress threshold. Fatigue analysis indicated that steel tower life was consistent, but concrete hull fatigue varied. SPAR 2 exhibited a shorter fatigue life than SPAR 1, suggesting that a larger cross-sectional area with the same pretension led to larger variations in compression fatigue. However, the expected lifetime of the concrete hull is much larger than what would be dimensioned for an expected hull.

The thesis employed the OpenMDAO framework for design optimization, resulting in improved designs with weight reductions and improved stability and performance characteristics. Despite acknowledging challenges in manufacturability and cost due to the complexity of the optimized geometries, the study showcased the effectiveness of the OpenMDAO framework in optimizing the design of offshore wind turbine structures.

Sammendrag

Denne avhandlingen undersøker gjennomførbarheten av å inkorporere betongstrukturer i en optimaliseringsmodell, basert på to forenklede spar-strukturer utviklet av Oh et al. [55] for å støtte en 10 MW DTU vindturbin [2]. Disse modellene er deretter inkorporert i den lineær frekvensdomenemodellen utviklet av Hegseth et al. [34]. En omfattende analyse av flere nøkkelaspekter ble utført, ved å sammenligne resultatene fra de ikke-lineære og lineære modellene, inkludert naturlige perioder, potensielle strømningsresultater, spektrale sammenligninger, indre krefter, betongkapasitet, tretthetsanalyse, og designoptimalisering ved bruk av OpenMDAO-rammeverket.

Undersøkelsen avslørte forskjeller mellom ikke-lineære og lineære modeller når det gjelder bølgeeksitasjon og tilleggsmasse-effekter. SPAROpt-modellene viste lavere bølgeeksitasjon i surge-bevegelse ved høyere bølgefrekvenser, mens pitch-eksitasjon ble overvurdert ved lavere frekvenser. Den større sparen viste større demping på grunn av dens større geometri. Konstant vindtest ga betryggende resultater, med rotoren som oppførte seg som forventet. Studien gjennomførte en forfallstest for å evaluere de naturlige periodene til surge, heave, pitch, og yaw-bevegelser. Den fleksible sparen viste lavere yaw naturlige perioder på grunn av variasjoner i massedistribusjon. Ved tårnbasen ble det observert små variasjoner i den første pitch bøyningsnaturlige frekvensen mellom modellene.

Spektrale sammenligninger ble utført for å vurdere den spektrale tettheten av SIMA og SPAROpt-modeller under bølge- og vindforhold. Selv om SPAROpt hadde begrensninger og hadde en tendens til å undervurdere spesifikke responsparametere, indikerte standardavviket av responsene at de relative styrkene og variasjonene innen frekvenskomponentene ble bevart. Merkbare avvik ble observert i bøyning under overgangen fra betong til stål, noe som resulterte i betydelig større eksitasjon i SPAROpt. Analysen av indre krefter ga innsikt i viktige trender og påkjenninger. Ballastbelastningen påvirket skjærkreftene, mens bøyemomentene viste forventet oppførsel, med det høyeste bøyemomentet som oppstår i fairlead-regionene. Aksielle og skjærspenninger ble påvirket av variasjoner i tykkelse og geometriske forskjeller.

Vurderingen av betongkapasiteten viste tilfredsstillende ytelse, med både SPAR 1 og SPAR 2 som opprettholdt forhold under sviktgrensen. Korttids aksielle spenninger forble innenfor akseptable grenser, og langtids aksielle spenninger forble konsekvent under den tillatte spenningsgrensen. Tretthetsanalyse indikerte at ståltårnets levetid var konsistent, men betongskrogets tretthet varierte. SPAR 2 viste en kortere tretthetslevetid enn SPAR 1, noe som tyder på at et større tverrsnittsområde med samme forspenthet førte til større variasjoner i kompresjonstretthet. Imidlertid er den forventede levetiden til betongskroget mye større enn det som ville bli dimensjonert for et forventet skrog.

Avhandlingen benyttet OpenMDAO-rammeverket for designoptimalisering, noe som resulterte i forbedrede design med vektreduksjoner og forbedrede stabilitets- og ytelseskarakteristika. Til tross for å anerkjenne utfordringer i produksjon og kostnad på grunn av kompleksiteten i de optimaliserte geometriene, viste studien effektiviteten av OpenMDAO-rammeverket i å optimalisere designet av offshore vindturbinstrukturer.

Table of Contents

List of Figures

List of Tables

Acronyms

ALS	Accidental Limit State.
BEM	Blade Element Momentum.
COB	Center of Buoyancy.
COG	Center of Gravity.
COBYLA	Constrained Optimization BY Linear Approximations
DNV-GL	Det Norske Veritas - Germanischer Lloyd
DOE	Design of Experiments
DOF	Degree of Freedom.
FD	Frequency Domain
FE	Finite Element
FEM	Finite Element Method
FLS	Fatigue Limit State
FOWT	Floating Offshore Wind Turbine
IEA	International Energy Agency
LEFM	Linear Elastic Fracture Mechanics
PC	Prestressed Concrete
RAO	Respons Amplitude Operatør
SLS	Service Limit State
SWL	Still Water Line
TLP	Tension Leg Platform
TD	Time Domain
ULS	Ultimate Limit State

Nomenclature

$\boldsymbol{\omega}$	Vorticity vector
$\boldsymbol{V}$	Velocity vector.
α	Angle.
β_{cc}	Concreates age after 28-days
β	Frequency ratio
δS	nominal stress range
η_j	Random phase angle.
Λ	The logarithmic decrement.
λ	Wave length.
μ	Kinematic viscosity.
∇	Fluid volume.
ν	Poisson's ratio.
ω_0	Natural frequency.
ω_d	Damped natural frequency.
ω_p	Angular peak frequency.
Ω	Angular velocity.
ω	Circular frequency.
ϕ	Velocity potential
ρ_a	Density of air.
ρ	Density of water
σ_d	Standard deviation.
σ_r	Solidity rate.
ξ_d	Damping ratio.
ζ_a	Wave amplitude.
ζ	Wave elevation
a'	Angular induction factor.
A_γ	Normalizing factor.
a	Axial induction factor.
B	Number of blades on wind turbine.
C_d	Drag coefficient.
C_l	Lift coefficient.
C_n	Coefficient normal to rotorplane.
C_t	Coefficient tangential to rotorplane.
c_{cr}	Critical damping.
c	Damping.
dQ	Torque for for an angular ring.
dT	Thurst for for an angular ring.
D	cumulative damage
E	The elasticity modulus.
f_{cm}	The mean concrete compressive strength
f	Frequency.
g	Acceleration of gravity
H_s	Significant wave height.
h	Water depth.
I_t	Turbulence intensity.
I	The moment of inertia
k_w	Wave number.
KC	Keulegan-Carpenter Number
k	Stiffness.
m	Mass.
n_i	Number of cycles

p_0	Atmospheric pressure.
p_D	Dynamic pressure.
p	Pressure
Q	External force.
Re	Reynolds number.
$S(\omega)$	Wave spectrum.
S_{PM}	Modifed Pierson-Moskowitz spectrum.
s	Cement type coefficient
T_p	Peak period.
t	Time
U	Wind speed.
u	Velocity.
v_0	Upstream wind.

1 Introduction

1.1 Background

The energy transition, also known as the shift towards sustainable energy sources, is driven by various factors, including the need to reduce greenhouse gas emissions, the growing adoption of renewable energy technologies, and the increasing demand for clean energy. Offshore wind has emerged as a leading renewable energy source, with annual growth rates of 30% between 2010 and 2018 (IEA, [15]). The offshore wind industry has seen rapid expansion, going from under 1 GW of installed capacity in 2006 to 19 GW in 2017 (IRENA, [37]). However, the offshore wind market still has significant untapped potential. According to the International Energy Agency (IEA), offshore wind has the potential to generate 420,000 TWh annually, which is 11 times the current global energy demand (IEA, [15]).

Offshore wind energy is a crucial contributor to meeting the increasing energy demand while promoting sustainable development. To further develop offshore wind, it will be necessary to investigate the feasibility of installing turbines in previously challenging areas. Currently, most installed wind turbines are bottom-fixed, limiting their mobility, and increasing their visibility due to shallower waters. To address these limitations, there has been significant investment in floating offshore wind turbines (FOWT), which can operate in deeper water and out of sight (Irena, [36]). In a forecast published in 2022 by Det Norske Veritas (DNV), it is predicted that 83% of the world's electricity will come from renewable sources by 2050 (DNV, [61]). As shown in Figure 1.1, global electricity generation is expected to increase its reliance on offshore wind energy. This trend reflects the growing focus on renewable energy sources and the potential for offshore wind to play a major role in global electricity production.

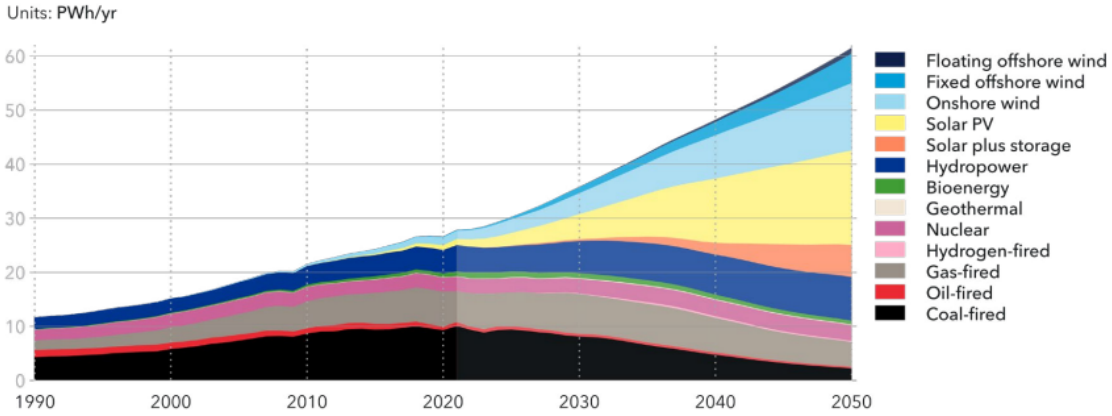

Figure 1.1: The worlds power production by different sectors (DNV, [61])

According to research by WindEurope, there are over 50 FOWT designs being developed globally, with 34 of them located in Europe (WindEurope, [53]). These designs include 62% semi-submersibles and 20% spar buoys. Most FOWT designs currently use steel foundations, with 80% of designs utilizing this material (WindEurope, [53]). Steel is preferred due to its faster assembly with pre-fabricated parts compared to concrete foundations. However, recent studies have shown that concrete foundations may be highly competitive compared to steel in terms of corrosion resistance and low maintenance costs. As a result, floating concrete structures have gained interest from the oil and gas industry. Modern processing and installation methods have also overcome previous limitations associated with concrete installations (Multiconsult, [45]). The use of concrete foundations in FOWTs may therefore be important for the growth of the offshore wind industry.

The objective of this master's thesis is to update an existing design optimization model to consider concrete substructures. To validate the optimization model, a detailed time-domain simulation is compared to the linearized model used by the optimization model.

In addition, the hull is evaluated by regarding the capacity, the trends in load

this master thesis is a continuation of a project report written during the fall of 2022. The project report consists of a literature review of wind and wave loads, FOWT dynamics, fatigue of steel and concrete, and extreme strength assessment for concrete structures. It also included a verification of the linearised model by cosiderin a steel spar.

1.2 Objective

This project investigates the theoretical aspects of environmental loads, dynamics, and fatigue of FOWTs. Further insight into reinforced concrete's material characteristics and properties, including the constructional aspect of marine concrete structures. The key focus of these investigations is to identify parameters and constraints that can be used in an optimization process to design an optimal concrete FOWT.

A case study will be conducted by using a spar substructure, and a 10 MW turbine will be used as a starting point. The goal is to compare the natural periods for surge, pitch, and first tower bending between a nonlinear and a simplified linear model in order to verify and validate the simplified model. This comparison will provide insight into the accuracy and effectiveness of the simplified model and will allow for further add-ons to the simplified model in the form of key parameters and constraints that can be used in an optimization process. By quantifying the differences between the nonlinear and linear models, it will be possible to develop a more accurate and faster design estimation for a FOWT.

1.3 Limitations

- For the simplified model, when cosidering DOFs only the surge, pitch, and 1st bending are considered.
- The mooring is unchanged in this thesis and kept unchanged. Only the fairlead connection point is modified.
- The tower geometry is kept constant for all models, and there is not preform any buckling control of the tower.
- The optimization does not consider Mathieu instability in its constraints.

2 Literature Review

2.1 Brief History

2.1.1 FOWT Concepts

A FOWT is a wind turbine mounted on a floating structure held in place by means of anchoring to the seabed. The three dominating floating support structure classifications are spar, semi-submersible, and Tension Leg Platform (IEA, [15]), as shown in Figure 2.1.

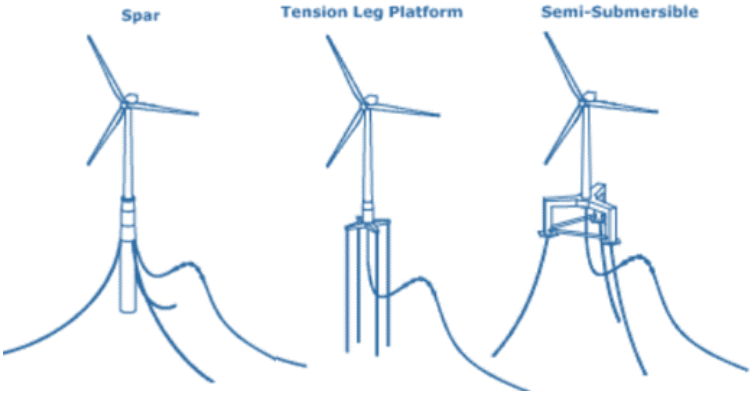

Figure 2.1: The dominating floating support structures (Scheu et al., [4])

Spar Platform

The spar is a tall, slender structure with a deep draft, designed to be ballast stabilized, with its Center of Gravity (COG) placed below its Center of Buoyancy (COB). This yields a high metacentric height and reduces its heave motion. However, its long draft ranging from 70 m and up can result in more complicated logistics for the foundation's assembly, transportation, and installation (WindEurope, [53]).

Semi-Submersible

The semi-submersible is a floating platform stabilized by buoyancy. It consists of columns connected by submerged pontoons, which provide buoyancy. The semi-submersible can experience significant heave motion in rough weather, but heave plates can be added to improve its stability. One of the main advantages of the semi-submersible is its ability to operate in a wide range of water depths (Bachynski, [12]).

Tension Leg Platform

The tension leg platform (TLP) is a floating platform stabilized by vertical mooring lines held in tension by the buoyancy of the platform. This allows the TLP to behave like a rigid structure in the vertical plane, with minimal motion in roll, heave, and pitch (Bachynski, [12]).

Steel is commonly used in the construction of FOWTs due to its strength, durability, and suitability for marine environments. However, it is important to recognize that concrete is another material option for marine construction. Concrete offers several advantages, including its ability to withstand harsh marine conditions and its potential for cost-effective construction.

2.1.2 Reinforced Concrete in Floating Marine Structures

Concrete is one of the oldest man-made building materials. Excavations in the Mediterranean area indicate that concrete made from natural pozzolanic cement has been used for over 2000 years in structures, many of which were exposed to seawater (Juliebø, [40]). Despite its early use in ancient times, this form of concrete fell out of favor during the collapse of the Roman Empire and was not used for many years until the mid-18th century (Camões and Ferreira,[17]). John Smeaton, a British civil engineer, undertook extensive testing of various limes available at the time. Through his research, he discovered that the hydraulicity of lime was related to different minerals either present in the limestone or added, such as pozzolans. He combined this hydraulic lime with powdered brick and pebbles to create the first form of modern concrete, which was used to build the Eddystone Lighthouse along with stone masonry in 1759 (Juliebø, [40]). The benefit of Smeaton's hydraulic lime was that the mortar and concrete set rapidly despite the wet conditions of the site. This early research led to the invention of modern-day Portland cement, developed in 1824 by Joseph Aspdin, and it quickly became the dominant cement used in construction.

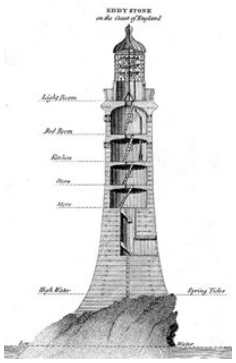

Figure 2.2: Eddystone Lighthouse (Juliebø, [40])

Lambot is credited with the first application of reinforced concrete in floating structures when he in 1848 constructed a boat by putting sand-cement mortar over a framework of iron bars and mesh (Fiorato, [24]). This boat was the first concrete vessel and the earliest known example of reinforced concrete. Although multiple reinforced concrete barges were created after Lambot's early work, the first self-propelled reinforced concrete ship was not constructed until 1917. This vessel was constructed in Norway by N.R. Fougner (Fougner et al. [27]) and is illustrated in Figure 2.3.

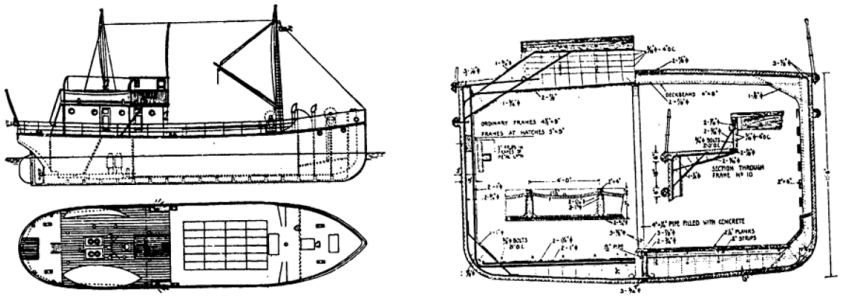

Figure 2.3: M. S. Namsenfjord: deadweight: 180 tonnes, length: 24 m (Fiorato, [24])

The steel shortages that occurred during World War I are a significant factor in the continuous development of concrete ships. In 1918, the U.S. Emergency Fleet Corporation initiated a program to construct twelve reinforced concrete ships primarily made of lightweight concrete. Due to their late completion, none of the warships the Emergency Fleet Corporation produced saw considerable duty during the war. Following the war, there was a surplus of shipping tonnage, and concrete ships could not economically compete with conventional ships (Fiorato, [24]).

After World War I, a few concrete boats were constructed, but it was not until World War II that another large concrete ship program was initiated. Midway through 1941, the United States Maritime Commission launched a project that resulted in building 104 boats, 20 of which were self-propelled. Some vessels from World War I and II saw extended duty, but due to their inappropriate design and weight the concrete ships were decommissioned after the war due to fuel costs and served as more stationary structures such as storage silos, quays, and breakwaters.

Figure 2.4: USS Slema (Kazek, [41])

In the 1970s and 1990s, there were significant advancements in the construction of offshore concrete platforms, particularly in the North Sea. These structures were designed to withstand extreme environmental loads and were installed at depths of up to 300 meters. One of the most well-known and significant of these structures is the Troll-A platform (shown in Subfigure 2.5a), which is located in the Norwegian trench at 303 meters of water depth and is one of the leading gas producers in the North Sea. Subfigure 2.5b shows the first, and currently only, concrete semi-submersible with catenary mooring, while Subfigure 2.5c shows the Heidrun, the first tension leg floater with a concrete hull. Both of these structures are made with high-strength lightweight aggregate concrete and pre-tensioned reinforcement (Gudmestad et al. [20]). These examples demonstrate the feasibility of using concrete in constructing offshore platforms and other marine structures.

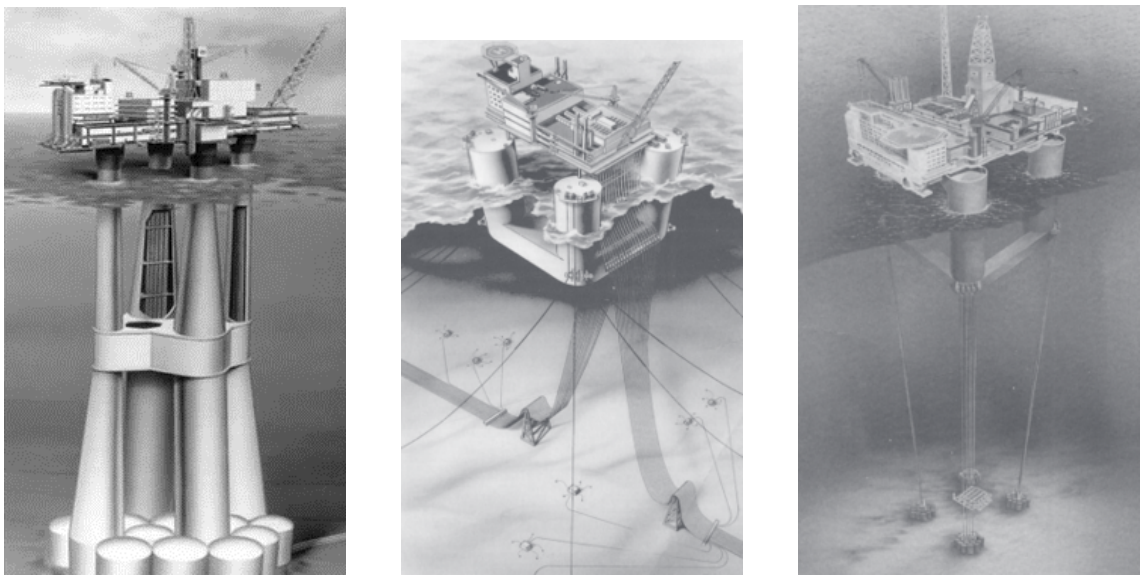

(a) Troll A (b) Troll B (c) Heidrun

Figure 2.5: Concrete hulls (Gudmestad et al. [20])

The recent reapplication of concrete substructures in the design of offshore wind farms is exemplified by the Hywind Tampen project. This project consists of 11 concrete spar structures with a length of 107m, and it is the first concrete slipforming of an offshore project in Norway since the delivery of Troll A in 1995 (Equinor, [21]). Hywind Tampen is the sister project of Hywind Scotland, which consists of 5 steel spar substructures. By comparing the two projects, Equinor was able to reduce the cost by 40% by using larger turbines, concrete substructures, new technology, and a new assembly method (Equinor, [22]).

Figure 2.6: Illustration of Hywind Tampen, (Aker Solutions, [56])

The utilization of concrete in marine construction brings forth several notable benefits, such as its durability, cost-effectiveness, and low environmental impact. By incorporating concrete into the construction of offshore structures, the potential for developing sustainable and economically viable solutions in marine operations is enhanced. Concrete substructures, in particular, offer a solid and stable foundation for offshore wind turbines and other equipment, facilitating improved operational efficiency and reliability within offshore wind farms. However, in order to realize the construction of such structures, careful consideration must be given to the construction possibilities as well as the inherent limitations that exist.

2.2 Construction of Concrete Spar

The construction of concrete spars for FOWT projects in Norway brings forth unique challenges and opportunities that can be analyzed from an optimization standpoint. By considering various factors related to concrete construction and availability, slipform techniques, and slipform rate, optimization strategies can be employed to enhance the efficiency and effectiveness of the construction process.

2.2.1 Concrete Construction and Availability

Marine concrete structures are constructed at inshore facilities/docks with small depth restrictions. This last point is crucial for its further construction because of the variation in length and depths of marine structures. The construction procedure requires the structures to be hydrodynamically stable under various conditions and construction phases (Gudmestad et al. [9]).

Concrete Supplier

The rate at which concrete is placed will determine the minimum number of concrete plants needed for a construction project. Even if the casting rate is within the capacity of a single plant, it is recommended to have multiple plants to ensure a continuous supply of concrete, even in the event of unexpected disruptions. According to Betong Fokus [25], over 180 concrete production facilities in Norway can transport concrete to different regions, as shown in Figure 2.7. However, the concrete plants should be within a reasonable distance from the construction site, and transport times must be considered when planning the concrete supply. Figure 2.8 also illustrates the regions in Norway where low-emission concrete is available, reducing production capacity in the country's northern part.

Figure 2.7: Concrete plants in Norway (Betong Fokus, [25])

Figure 2.8: Reqions that can supply low-emission concrete (Norsk Betongforening, [14])

These factors can have a crucial part when it comes to the objective of minimizing cost and lowering carbon emissions.

2.2.2 Slipform Construction

Description of Slipforming

Slipforming is a concrete casting method commonly used to construct tall vertical structures, such as silos, towers, and oil platforms. It involves using a hydraulic jacking system to gradually raise a form while pouring concrete into it layer by layer, as seen in Figure 2.9. This allows the concrete to set and harden over time, creating a homogeneous layer with good adhesion between the different layers (Jacobsen, [39]).

Slipforming has several advantages over traditional methods of concrete casting. Notably, it allows for the construction of taller structures with fewer joints, thereby enhancing the overall strength and stability of the structure. The method also promotes continuous concrete pouring, making it particularly suitable for watertight structures. Additionally, it can expedite the construction process and lessen the amount of labor required, leading to cost and time efficiency (Gudmestad et al. [20]). A significant advantage of slipforming is the ability to modify the geometry of the concrete structure during the casting process. By strategically altering the structure's shape, engineers can optimize its design for maximum strength, performance, and efficiency.

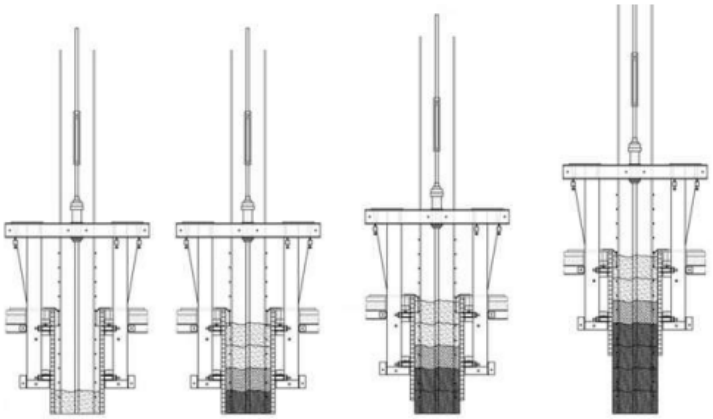

Figure 2.9: The principle of slipforming (Fosså, [26])

Conical Slipforming

Beyond straightforward structures with a constant cross-section, slipforming can be used to create structures with more complex geometries. Specifically, conical slipforming is employed when the structural geometry varies over the structure's height. This technique facilitates changes to the wall thickness, diameter, and inclination angle of the structure, opening opportunities for enhanced performance and reduced cost.

Using conical slipforming, changes in diameter and wall thickness can result in a more efficient distribution of material where it's most structurally necessary. This can lead to considerable reductions in material usage and overall cost. Adjusting the inclination angle can optimize load distribution, contributing to improved structural performance and stability.

While conical slipforming can be utilized in numerous applications, it is generally more costly than standard straight-up slipforming, with a price difference of up to five times (Fuglestad [28]). Also, the slipform can be inclined up to 35 degrees under extreme circumstances, but it's generally not recommended to exceed 20 degrees. The maximum curvature per meter should be 100 mm, with a practical upper limit of 50-80 mm. Due to space constraints, conical slipforming with a diameter of less than 1.5 m should be avoided (Norsk Betongforening [16]). A complete presentation of the restriction is presented in Table 2.1

Table 2.1: Conical slipform parameter restriction, (Norsk Betongforening, [16])

Diameter [m]	**Thickness [m]**	**Height [m]**	**Inclination [deg]**
2.0 - 40.0	0.20 - 1.3	300	20°

The successful execution of conical slipforming depends on the contractor's expertise and experience in incorporating demanding geometries in their construction process. This underlines the significance of the contractor's role in leveraging the potential of slipforming methods to optimize cost, material usage, and structural performance.

According to Fuglestad [28], offshore concrete structures tend to have much higher reinforcement densities of over 300-350 kg/m3. This can make it challenging to ensure the right coverage between seawater and reinforcement for a conical slipform, particularly for structures with steep inclination curves and increasing reinforcement. Fuglestad [28] further mentions that the formwork is always straight in the vertical direction to match the wanted geometry. However, this can lead to increased drag friction between the slipform and the concrete, which can cause cracks and defects on the structure's surface. This can reduce the structure's overall lifespan and performance. As a result, the success of a conical slipform is highly dependent on the contractor's experience and expertise in applying demanding geometries in their construction process.

Slipform Rate

The curing time of concrete is an important factor in slipforming. In some cases, it can be difficult to predict the exact curing time due to variations in background conditions, such as air temperature. The slipform rate can also influence the curing time, and it is often desirable to match the setting time to the slipform rate to ensure that the concrete can harden and set properly. To accomplish this, admixtures can be used to adjust the curing time of the concrete. Admixtures are added to the concrete mix in small amounts to modify its properties and improve its performance. Some admixtures can slow down the curing time, while others can accelerate it. By carefully selecting and using the right admixtures, it is possible to control the curing time of the concrete and ensure that it is suitable for slipforming.

2.3 Optimization Work

In optimal design for FOWTs, the cost of the substructure is a significant factor, representing 15 to 30% of the total CAPEX (Ashuri et al. [7]). Therefore, designing more affordable substructures without compromising performance is crucial. Optimization plays a key role in achieving this goal by using numerical models as a powerful tool for cost-efficient structure design.

Researchers have utilized various techniques to investigate and enhance FOWT designs. Tracy et al. [59] and Bachynski and Moan [9] conducted parametric investigations for FOWTs and Tension Leg Platforms (TLPs), respectively, exploring design possibilities defined by selected parameters. These studies employed frequency analyses and time-domain simulations to examine different designs. Clauss and Birk [30] attempted optimization using the "Direct Search Method," a gradient-free algorithm, to minimize motions and loads on offshore installations.

Gradient-based optimization methods, which efficiently handle a large number of design variables assuming analytical derivatives are available and have fewer local minimums, have been less commonly used in FOWT design. Chew et al. [19] optimized a jacket substructure with 22 design variables using the Sequential Quadratic Programming (SQP) method. Fylling and Berthelsen [29] optimized the shape of the buoy, power cables, and mooring lines using a gradient-based algorithm with finite differences. In both studies, the objective function considered the cost of the optimized elements.

Previous research has mainly focused on the platform and mooring lines, neglecting the tower, control system, and rotor behavior. To accurately predict the system's global response, it is crucial to consider the coupling effects between the floater, tower, controller, and blades. Lemmer et al. [44] optimized a TripleSpar concept floater with a self-tuning controller using the Pattern Search method. Sandner et al. [54] achieved integrated optimization of spar-type FOWTs with a PI-controller, taking rotor speed and tower bending into account as optimization criteria.

Using the OpenMDAO framework, Ashuri et al. [8] optimized the aerodynamic and structural design of the rotor and tower for a 5 MW NREL wind turbine, reducing the Levelized Cost of Energy (LCoE) by 2.3%. Hegseth et al. [34] developed a linearized aero-hydro-servo-elastic model for a 10 MW spar FOWT and performed integrated design optimization of the platform, tower, mooring system, and blade pitch controller. This comprehensive approach emphasized the influence of platform design on the behavior of the tower and controller. The linearized model enabled gradient-based optimization of the structure using analytical gradients.

Hegseth's linearization process involved various techniques to capture the flexible spar's responses accurately. Hydrodynamic loads were linearized using a first-order wave load approximation, incorporating Maccamy-Fuchs theory for estimating wave loading on the cylindrical spar. Constant added mass coefficients based on strip theory were used to account for higher-order wave loads. The consideration of radiation damping is neglected, while viscous damping is calculated through stochastic linearization of the drag term in Morison's equation. Structural dynamics were linearized using Euler-Bernoulli beam elements to analyze the combined bending of the wind turbine tower and hull column and their impact on the system response. Aerodynamic loading was computed using blade element momentum (BEM) theory, which linearized each blade element's lift and drag

forces. The linearized approach simplified calculations and improved computational efficiency by neglecting dynamic wake

This project intends to apply the integrated optimization methodology to concrete Spar buoy from Oh et al. [55], which accommodates the DTU 10 MW reference wind turbine.

3 Aerodynamic

3.1 Wind Description

3.1.1 Wind Resource Variation

Due to the variation in atmospheric pressure, air tends to flow from high to low pressure. The earth's rotation controls the circulation of the atmosphere, while seasonal fluctuations of solar energy cause variations in circulation (Manwell et al. [38]). These considerable spatial variances are crucial for evaluating optimal locations for wind turbines. Figure 3.1 illustrates the average capacity factors for offshore wind along the coastline, which is greater in the north and south, where temperature fluctuations are often greater than at the equator. This is because wind speeds in these regions are often higher, which can provide more power to wind turbines.

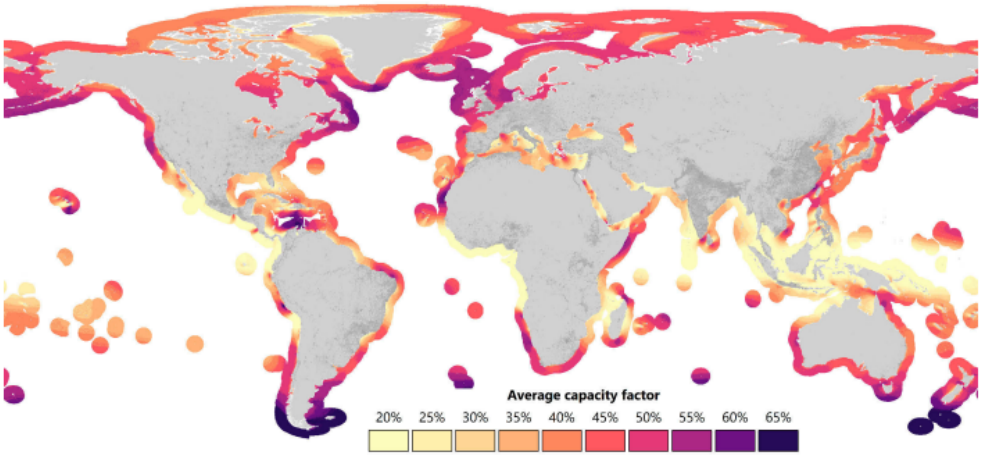

Figure 3.1: Average simulated capacity factors for offshore wind worldwide (GLOBAL.WIND.ATLAS, [31])

In addition to global spatial variations in wind speed and direction, wind turbines also experience local spatial differences that can affect their performance. A variety of factors, including differences in terrain and the presence of nearby structures, can cause these local variations. Figure 3.2 illustrates a typical wind speed distribution, which is referred to as the vertical profile of wind speed or vertical wind shear (Manwell et al. [38]). It further shows how the wind speed can vary with altitude and demonstrates the spatial variance of the wind that can lead to differences in the loads experienced by a wind turbine. As wind turbines continue to grow in size and reach higher altitudes, they will encounter regions with higher wind speeds and more significant spatial variations in the wind. This can increase the loads on the turbine, potentially leading to greater wear and tear on the structure. Figure 3.2 illustrates a transient representation of a wind speed distribution.

In addition to the differences that may be found in space, there can also be differences in time. Variations in time may be divided into four parts: inter-annual, annual, diurnal, and short-term. Short-term fluctuations span over ten minutes and include turbulence and gusts.

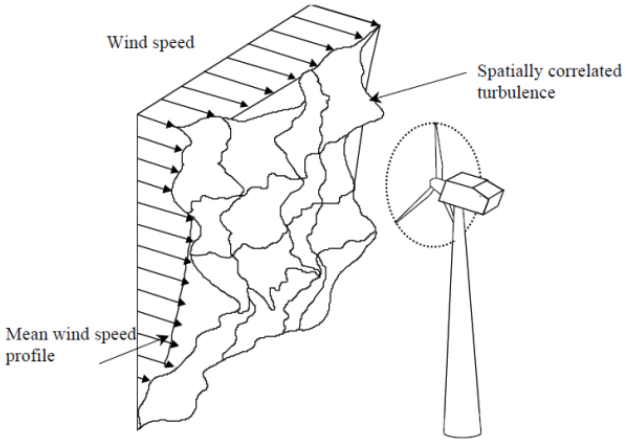

Figure 3.2: Wind velocity profile. (Ormel, [52])

3.1.2 Turbulence

According to Burton [6], turbulence is primarily caused by two factors:

1. Friction with the surface of the earth, which can be thought of as extending as far as flow disturbance caused by topographical features such as hills and mountains.
2. Thermal effects can cause air masses to move vertically due to temperature variations and consequently air density variations.

Tempel [58] explains that the wind speeds in the lower 2 km of the earth's atmospheric boundary layer are affected by surface friction, often called wind shear. This effect reduces the wind speed from a uniformly distributed value to an undistributed value at 2 km, and it stretches down to zero at the earth's surface. According to Manwell et al. [38], the degree to which surface friction affects the wind speed can vary depending on the surface roughness of the terrain. For example, the surface roughness length is 0.20 mm for the calm open sea and 0.50 mm for the blown sea, while large structures in city centers have a roughness length of 3000 mm.

Turbulence intensity is a measure of how dramatically the wind changes over time. It is given as a percentage and is calculated using Equation 3.1, which expresses that the turbulence intensity I_t is equal to the standard deviation σ_d, of the time-varying wind speed U. Higher turbulence intensity is often associated with terrain with a rougher surface, which can affect the performance of wind turbines and other structures that are exposed to the wind.

$$I_t = \frac{\sigma_d}{U} \tag{3.1}$$

The intensity of turbulence is therefore based on altitude and terrain roughness. Higher turbulence intensities are caused by more rugged terrain and lower altitude. Design standards provide turbulence intensity descriptors based on these roughness and altitude factors, and certain sites can be assigned preset turbulence values (Tempel, [58]).

3.1.3 Wind Spectrum

A wind spectrum is a graphical representation of the range of amplitudes, frequencies, and phases in the turbulent wind (Manwell et al. [38]). It is often used to analyze wind turbine behavior and other structures exposed to the wind. According to Burton et al. [6], the von Karman and Kaimal spectra are two commonly used spectra to characterize the spectrum of the longitudinal component of turbulence. The Kaimal spectra are typically better fitted to empirical data of atmospheric

turbulence, while the von Karman spectra provide a good description of wind tunnel turbulence. According to the International Electrotechnical Commission (IEC) standard, the random wind velocity field for the turbulence models must fulfill the Kaimal spectrum for standard wind turbine classes.

Figure 3.3 shows the IEC Kaimal turbulent wind spectrum for different turbulence intensities as a function of frequency in Hz. This figure illustrates how the turbulence intensity can vary with frequency and can be used to predict the effects of turbulence on wind turbines.

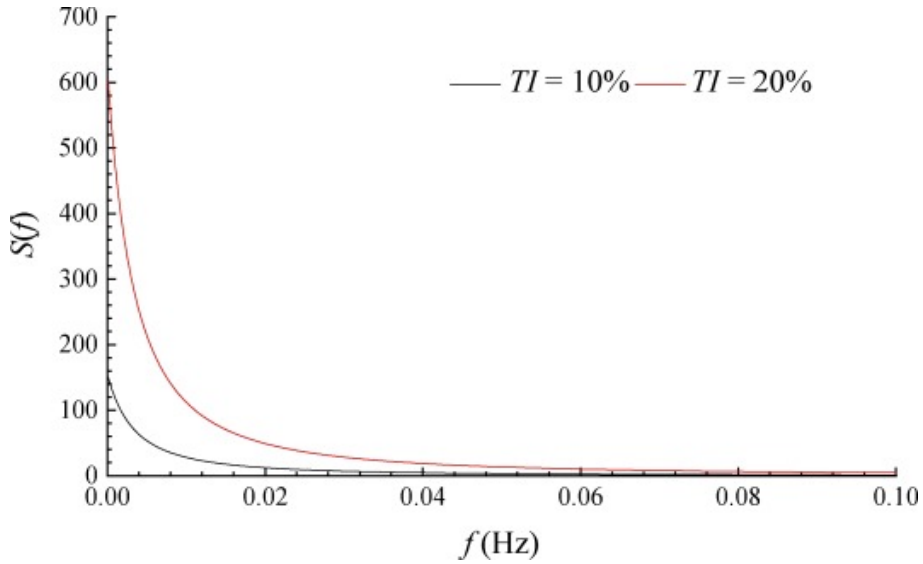

Figure 3.3: IEC Kaimal turbulent wind spectrum (Liange et al. [3])

From Figure 3.3 it is seen that for lower frequencies the oscillations are dominated by the wind. Further, the spectrum increases significantly for large turbulence intensity, leading to higher loads on a structure.

3.2 Blade Element Momentum Theory (BEM)

3.2.1 Method

The BEM theory is a widely-used method for modeling the aerodynamic behavior of wind turbines. It combines the momentum theory with a blade element approach, which allows for a more detailed analysis of the forces acting on each section of the turbine blade. However, the theory relies on several simplifications and assumptions that may not always hold true in real-world conditions. Despite these limitations, the BEM theory has proven to be a valuable tool for predicting turbine performance and optimizing design parameters. The simplifications and assumptions are:

- It is assumed that the 2D flow is uniform.
- The principle of 2D airflow blade theory is applied.
- Wind flow around the turbine blade is in a steady state, which means that it is assumed to be constant and unchanging over time, even though wind gusts are present in reality and the wind is not constant.
- If a blade is separated into distinct components, it is assumed that no interaction occurs between them. Each element of the blade has a unique velocity and direction.
- No deflections are assumed to occur in the blades, which are assumed to be perfectly rigid.

Based on the momentum theory, the thrust and torque for an annular ring can be expressed as:

$$dT = 4a(1-a)\frac{1}{2}\rho_a v_0^2 2\pi r dr \tag{3.2}$$

$$dQ = 4a'(1-a)\frac{1}{2}\rho_a v_0 \Omega r^2 2\pi r dr \tag{3.3}$$

While drag is parallel to the velocity, the lift is perpendicular to it. This velocity is called the relative velocity V_{rel} and is the resultant of the rotor rotation, the incoming wind, the induced axial velocity, and the induced tangential velocity (Bachynski, [10]). Both the lift and drag forces are projected into p_n and p_t as:

$$p_n = Lcos(\phi) + Dsin(\phi), \tag{3.4}$$

$$p_t = Lsin(\phi) - Dcos(\phi), \tag{3.5}$$

Where Figure 3.4 illustrates L and D as the lift and drag forces, respectively. ϕ represents the angle between the rotational plane and the relative velocity.

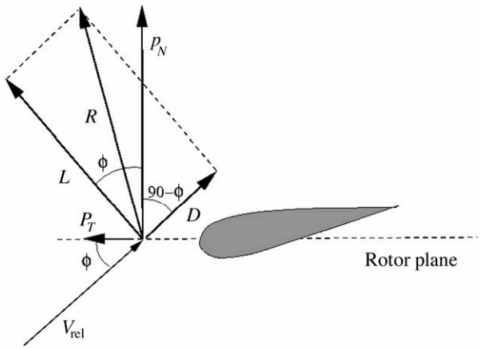

Figure 3.4: Local loads on a blade (Hansen, [33])

The normal coefficient C_n and tangential coefficient C_t are based on Equation 3.4 and 3.5. This will give the equations:

$$C_n = C_l \cos(\phi) + C_d \sin(\phi) \tag{3.6}$$

$$C_t = C_l \sin(\phi) - C_d \cos(\phi), \tag{3.7}$$

where C_l and C_d are the lift and drag coefficients, respectively. The area covered by the blades in the control volume is the region referred to as solidity ratio σ_r and can be expressed by:

$$\sigma_r = \frac{Bc}{2\pi r}, \tag{3.8}$$

where B is the number of blades, c is the chord length, and r is the radial position of the control volume. Since p_n and p_t are force measurements per length, it is possible to express the thrust and torque using Equation 3.6 and Equation 3.7.

$$dT = Bp_N dr = B(L\cos(\phi) + D\sin(\theta))dr \tag{3.9}$$

$$dQ = Brp_T dr = B(L\sin(\phi) - D\cos(\phi))dr \tag{3.10}$$

The expressions for the axial induction factor a and the angular induction factor a' can be derived by setting the equations for thrust and torque equal to each other and combining them with the solidity. This enables the solution for unknown variables and the establishment of relationships between different quantities.

$$a = \frac{1}{\frac{4\sin^2(\phi)}{\sigma C_n} + 1} \tag{3.11}$$

$$a' = \frac{1}{\frac{4\sin(\phi)\cos(\phi)}{\sigma C_t} + 1} \tag{3.12}$$

However, the coefficients for normal force (C_n) and tangential force (C_t) depend on the axial and angular induction factors (a and a'), which are unknown. Therefore, an iterative procedure is needed to solve for a and a' based on the equations for thrust and torque. To do this, we:

- Provide initial starting values for a and a'.
- Perform calculations of ϕ, α, C_l, and C_d using these initial values.
- Update the values of a and a' based on the calculated values of ϕ, α, C_l, and C_d.
- Check for convergence within a given tolerance level and repeat the calculations with updated values until convergence is achieved.

This iterative procedure allows for the determination of the aerodynamic performance of the turbine blade.

3.2.2 Corrections

When using BEM theory, several corrections need to be considered. These corrections are often included in simulations to obtain reasonable results. These corrections are:

Prandtl's tip loss factor: When applying BEM theory, it is assumed that there are infinite blades. However, the tip loss factor developed by Prandtl refutes this assumption. Hansen ([33]) explains that the vortex system in the wake of a rotor with a finite number of blades differs from that of a rotor with an infinite number of blades. Bachynski [10] further explains that this is due to the air's tendency to flow around the tip, following the pressure gradient, which runs from the lower to the upper side. The correctional equation for Prandtl's factor is:

$$F = \frac{2}{\pi}\cos^{-1}\left[\exp(-\frac{B(1-r/R)}{2r\sin(\phi)/R})\right] \tag{3.13}$$

Glauert correction
Once the axial induction factor exceeds about 0.4, the one-dimensional momentum theory is no longer valid. For these cases, there is an empirical relationship between the axial induction factor and the thrust coefficient known as the Glaubert correction factor (Hansen, [33]), which is given by:

$$C_T = \begin{cases} 4a(1-a)F & a \leq \frac{1}{3} \\ 4a(1-\frac{1}{4}(5-3a)a)F & a > \frac{1}{3} \end{cases} \tag{3.14}$$

Furthermore, it is important to note that additional corrections, such as dynamic wake, dynamic stall, and skewed wake, should also be implemented to improve the accuracy of BEM theory.

4 Hydrodynamics

4.1 Linear Potential Flow Theory

Assumption

When describing the ocean environment, some basic assumptions must be made when considering free surface fluid flow. The main points are described by Faltinsen [23] as follows:

1. The fluid is assumed incompressible and inviscid
2. The flow is irrational
3. The velocity potential ϕ describes the fluid velocity vector

$$\mathbf{V}(x, y, z) = \nabla\phi \equiv \mathbf{i}(\frac{\partial\phi}{\partial x}) + \mathbf{j}(\frac{\partial\phi}{\partial y} + \mathbf{k}(\frac{\partial\phi}{\partial z}) \tag{4.1}$$

The velocity potential has no physical meaning, but it is introduced because of its convenient use in the mathematical analysis of irrotational fluid. The vorticity vector is described as

$$\omega = \nabla \times \mathbf{V}. \tag{4.2}$$

Since the fluid is incompressible, the fluid volume ∇ does not change. This implies that $(\nabla \cdot \mathbf{V} = \mathbf{0})$. In addition, the velocity potential has to satisfy the Laplace equation:

$$\frac{\partial^2\phi}{\partial x^2} + \frac{\partial^2\phi}{\partial y^2} + \frac{\partial^2\phi}{\partial z^2} = 0. \tag{4.3}$$

The pressure p follows Bernoulli's equation, where the z-axis is defined vertically and positively defined upwards. For unsteady, irrotational, and inviscid fluid motion, the Bernoulli equation can be expressed as:

$$p + \rho g z + \rho\frac{\partial\phi}{\partial t} + \frac{\rho}{2}|\nabla\phi| = C, \tag{4.4}$$

where C is the arbitrary function of time, ρ is the density of water, and g is the gravitational acceleration.

Boundary conditions

Other general issues affecting free surface fluid flow problems emerge when the boundary conditions are described. Two points should be made here.

Kinematic boundary condition

The Kinematic boundary conditions for a stationary body in a moving fluid are impermeable:

$$\frac{\partial\phi}{\partial n} = 0 \tag{4.5}$$

Here $\frac{\partial}{\partial n}$ identifies the differentiation along the normal to the body surface, defined positive into the fluid (Faltinsen [23]). The free surface boundary condition implies that a particle

on the free surface is assumed to stay on the free surface. This means that it always satisfies Equation 4.7 and $\frac{DF}{Dt} = 0$. The free surface can be defined by:

$$z = \zeta(x, y, t), \tag{4.6}$$

where ζ is the wave elevation. Furthermore, a new function F can be defined as:

$$F(x, y, z, t) = z - \zeta(c, y, t) = 0 \tag{4.7}$$

The last step is to apply the kinematic boundary condition equations as follows:

$$\frac{\partial}{\partial t}(z - \zeta(x, y, t)) + \nabla\phi \cdot \nabla(z - \zeta(x, y, t)) = 0 \text{ , (Faltinsen, [23])} \tag{4.8}$$

Dynamic free surface condition

For this condition, the water pressure is assumed to be equal to the constant atmospheric pressure p_0 on the surface for $z = \zeta$. Equation 4.4 can therefore be written as:

$$p = -\rho\left(\frac{\partial\phi}{\partial t} - \frac{1}{2}V^2 - gz\right) + c(t) = p_0 \tag{4.9}$$

Furthermore, one can set $c(t) = p_0$ as an integration constant to get the boundary condition on $z = \eta$ so it becomes:

$$\rho\left(\frac{\partial\phi}{\partial t} + \frac{1}{2}V^2 + g\zeta\right) = 0 \tag{4.10}$$

However, it is essential to emphasize that linearization leads to a simplification of the problem. Thus, it is applied to the nonlinear free surface described above. Due to this, the marine structure has zero forward speed and zero current moving through them. If linear wave theory is applied, the velocity potential is proportional to the wave amplitude only if the wave amplitude is small relative to the characteristic wavelength and body dimension. By applying linearity to the free-surface from $z = \zeta(x, y, t)$ to $z = 0$, the following free-surface equation applies:

$$\frac{\partial\zeta}{\partial t} = \frac{\partial\phi}{\partial z} \quad \text{(Kinematic condition)} \quad \text{on} \quad z = 0 \tag{4.11}$$

$$g\zeta\frac{\partial\phi}{\partial t} = 0 \quad \text{(Dynamic condition)} \quad \text{on} \quad z = 0 \tag{4.12}$$

By combining the two equations, the following equation ends up to be

$$\frac{\partial^2\phi}{\partial t^2} + g\frac{\partial\phi}{\partial z} = 0 \tag{4.13}$$

According to Faltinsen [23] the velocity potential oscillates harmonically in time with circular frequency ω, this makes it possible to write Equation 4.13 as:

$$-\omega^2\phi + g\frac{\partial\phi}{\partial z} = 0 \quad \text{on} \quad z = 0. \tag{4.14}$$

4.2 Linearized Wave Theory

Linear wave theory can be derived by assuming that the free surface has an infinite horizontal extent and that the seabed is horizontal. The free surface condition can be combined with the Laplace equation to derive the seabed condition, which is expressed as follows:

$$\frac{\partial \phi}{\partial z} = 0 \quad \text{on} \quad z = -h, \tag{4.15}$$

where h is the water depth. In addition, the velocity potential can be expressed as:

$$\phi = e^{kz}(Acos(kx) + Bsin(kx))cos(\omega t + \alpha), \tag{4.16}$$

in which the Laplace equation will be satisfied. The quantities A, B, and α are arbitrary constants.

Space and temporal changes are necessary for the velocity potential to describe propagating waves. The equations presented in Table 4.1 can be used to describe the parameters of regular sinusoidal propagating waves for deep water. Deepwater denotes a depth of water that is larger than half the wavelength, $h > \frac{1}{2}\lambda$, where λ is the wavelength. However, Faltinsen [23] describes that depth has little effect on the wave phase in deep water.

Table 4.1: Linear wave theory equations for infinite water depth.

Velocity potential	$\phi = \frac{g\zeta_a}{\omega} e^{k_w z} \cos(\omega t - k_w x)$
Wave number	$\frac{\omega^2}{g} = k_w$
Wavelength	$\lambda = \frac{g}{2\pi} T^2$
Wave profile	$\zeta = \zeta_a \sin(\omega t - k_w x)$
Dynamic pressure	$p_D = \rho g \zeta_a e^{k_w z} \sin(\omega t - k_w x)$
Velocity x-component	$u_x = \omega \zeta_a e^{k_w z} \sin(\omega t - k_w x)$
Velocity z-component	$u_z = \omega \zeta_a e^{k_w z} \cos(\omega t - k_w x)$
Acceleration x-component	$\dot{u_x} = \omega^2 \zeta_a e^{k_w z} \cos(\omega t - k_w x)$
Acceleration z-component	$\dot{u_z} = -\omega^2 \zeta_a e^{k_w z} \cos(\omega t - k_w x)$

Since the waves are linear, there are no non-linearities. In contrast to second-order solutions that produce sharper crests and shallower troughs, the perfect linear waves have equally sized troughs and crests. Greco, [32] explains that even though regular linear waves do not accurately represent ocean waves, they do serve to characterize more general waves.

4.3 Ocean Waves

Ocean waves come in a variety of sizes and shapes. The sea surface is therefore considered stochastic rather than characterized based on a single wave. The frequency and probability domains can be used to determine the statistical characteristics of waves. Deep-water wave heights have a Gaussian distribution, and shallow-water waves can be represented by a probabilistic distribution.

4.3.1 Statistical Description of Wave

By assuming that the sea surface is composed of a large number of long-crested waves, the wave elevation of a long-crested irregular sea, propagating along the positive x-axis, can be expressed as:

$$\zeta = \sum_{i=1}^{N} \zeta_{a,j} \sin(\omega_j t - k_{n,j} x + \epsilon_j) \tag{4.17}$$

where $\zeta_{a,j}$, ω_j and ϵ_j are the wave amplitude, circular frequency, and phase angle of wave component number j, respectively. The phase angles are uniformly distributed between 0 and 2π and

remain stable over time. Faltinsen [23] explains that the wave amplitude ζ_a can be expressed by using a wave spectrum $S(\omega)$

$$\frac{1}{2}\zeta_{a,j}^2 = S(\omega_j)\Delta\omega_j. \tag{4.18}$$

$\Delta\omega_j$ represents a constant frequency difference between successive frequencies. Figure 4.1 illustrates the relationship between the frequency domain representation for waves by a wave spectrum and the time domain solution. In the frequency domain, however, the wave is characterized by its frequency and amplitude.

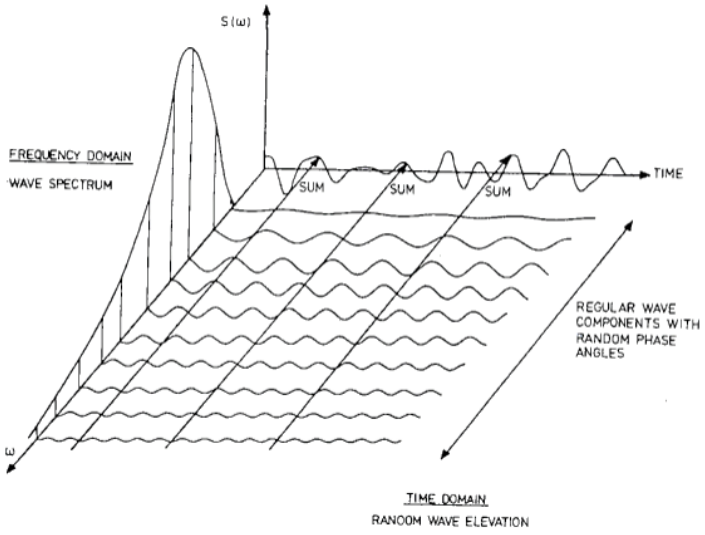

Figure 4.1: Connection between frequency domain and time domain representation of waves in a long-crested short-term sea state (Faltinsen, [23]).

4.3.2 Wave Spectra

When employing the wave spectrum, it is assumed that the ocean can be characterized as a stationary random process. The sea condition is described by the peak period T_p and the significant wave height H_s, which are considered to be constant if the sea is stationary. According to DNV-RP-C205, [62], a short-term description of the sea surface is assumed stationary for a duration of 20 minutes to 3-6 hours.

Real wave spectra may frequently be represented by idealized wave spectra. There are several wave spectrum suggestions for accurately describing ocean waves, such as:

- Modified Pierson-Moskowitz (recommended by 15th ITTC for fully-developed sea)
- JONSWAP (recommended by 17th ITTC for limited fetch).

The two-wave spectra mentioned above are illustrated in Figure 4.2.

The equations for the Pierson-Moskowitz spectrum is given by

$$S_{PM}(\omega) = \frac{5}{16}H_s^2\omega_p^4\omega^{-5}\ exp\left(-\frac{5}{4}\left(\frac{\omega}{\omega_p}\right)^{-4}\right), \tag{4.19}$$

where $\omega_p = \frac{2\pi}{T_p}$, is the angular peak frequency and the JONSWAP spectrum is given by

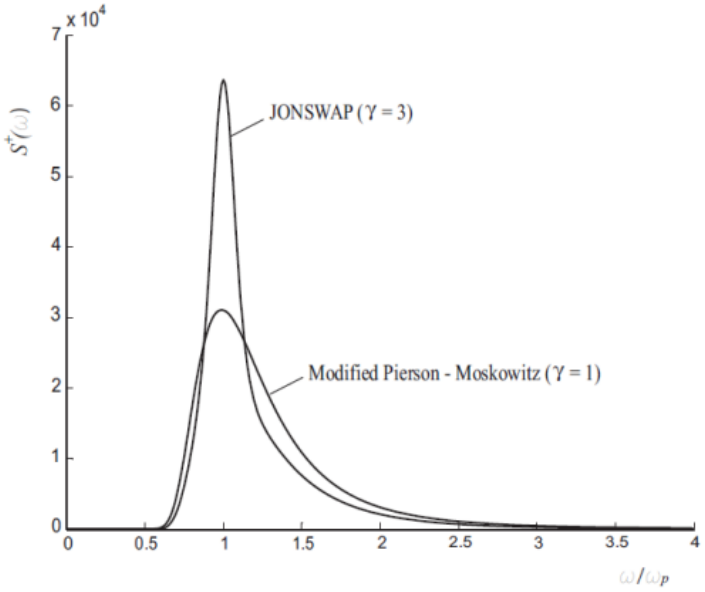

Figure 4.2: Example wave spectra with JONSWAP and Modified Pierson Moskowitz spectrum (Naess & Moan, [47])

$$S_J(\omega) = A_\gamma S_{PM}(\omega)\gamma \; exp\left(-0.5\left(\frac{\omega-\omega_p}{\sigma_d\omega_p}\right)^2\right). \tag{4.20}$$

A_γ is the normalization factor, γ is the non-dimensional peak shape parameter, and σ_s is the spectral width parameter (DNV, [62]). It is also important to mention that the JONSWAP spectrum is anticipated to provide an accurate representation for $3.6 < \frac{T_p}{\sqrt{H_s}} < 5$.

4.4 Wave Body Interaction

According to Faltinsen [23], the motion of a FOWT can be divided into four categories: wave-frequency motion, high-frequency motion, slow-drift motion, and mean drift. The DOFs of a FOWT are defined in the inertial reference frame, and the oscillatory translations and rotational motions of the FOWT are represented by surge, sway, heave, roll, pitch, and yaw, as shown in Figure 1 (Greco, [32]). These translations can be described using η_j, where j is the mode number. Therefore, the motion of any point on the body of the FOWT can be expressed as a combination of these DOFs.

$$s = (\eta_1 + z\eta_5 - y\eta_6)\boldsymbol{i} + (\eta_2 - z\eta_4 + x\eta_6)\boldsymbol{j} + (\eta_6 + y\eta_4 - x\eta_5)\boldsymbol{k} \tag{4.21}$$

4.4.1 Static Load

In a state of static equilibrium, a floating structure will experience hydrostatic pressure normal to the submerged surface. The gravitational force acting on the structure's mass will balance the vertical forces, and the gravitational force will equal the buoyancy force. This is the most fundamental load condition for a floating vessel.

$$F_{weight} = F_{buoyancy} \tag{4.22}$$

Hydrostatic loads can be calculated on a body by integrating the pressure distribution along the

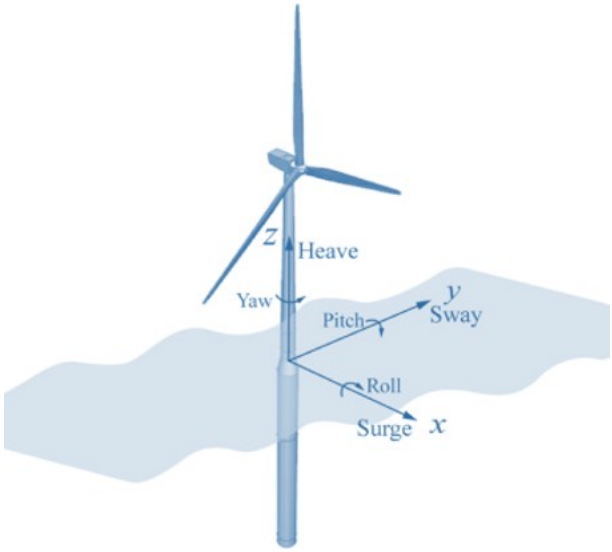

Figure 4.3: Schematic diagram of Cartesian coordinate system with translational and rotational motions (Yue et al. [5])

wet surface. In the case of a linear problem, the quadratic velocity component in Bernoulli's equation (Equation 4.4) makes it possible to determine the pressure as:

$$p = -\rho \frac{\partial \phi}{\partial t} - \rho g z, \tag{4.23}$$

where the first term is the dynamic load, and the last is the hydrostatic load. If a structure is assumed at rest, the dynamic part of the equation is zero.

In addition to wave loads, the static loads resulting from the current flow must also be considered. These loads can influence the form and magnitude of the incident waves and are typically approximated by mean values. The pressure distribution on the structure due to the current flow can also generate drag forces and vortex shedding, leading to asymmetric pressure distributions around the structure. These effects must be carefully considered in the design of marine structures.

4.4.2 Dynamic Loads

Due to the fact that results in an irregular sea can be produced by superimposing results from regular wave components, it is necessary to evaluate the presence of incident sinusoidal regular waves with a small wave steepness. For the following theory, steady-state conditions are assumed. Therefore, a structure's linear dynamic loads and motions are assumed to oscillate harmonically at the same frequency as the wave loads that excite the structure (Faltinsen, [23]). The overall hydrodynamic force exerted on a floating structure consists of three components.

$$F_{hydrodynamic} = F_{hydrostatics} + F_{Diffraction} + F_{radiation} \tag{4.24}$$

The two last terms of Equation 4.24 are the diffraction and radiation problem.

Diffraction occurs when the structure is fixed, and there are incoming regular waves (see left part of Figure 4.4). The loads are wave excitation forces consisting of Froude-Kriloff and diffraction forces (Faltinsen, [23]).

Radiation occurs when a structure is forced to oscillate at the frequency of the wave excitation without incident waves (see the middle part of Figure 4.4). As the body moves, waves are radiated, and the body is subjected to hydrodynamic loads characterized by damping, added mass, and

restoring terms (Greco, [32]). The restoring terms relate to the hydrostatic pressure, while the added mass and damping terms relate to the dynamic pressure resulting from the body motions.

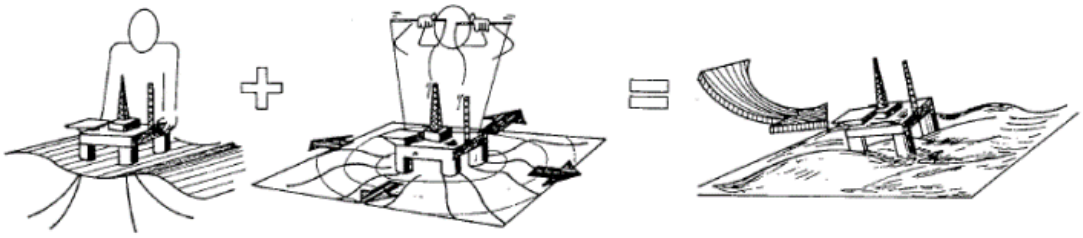

Figure 4.4: The illustration of diffraction and radiation problem (Faltinsen, [23])

4.4.3 Restoring Force and Moments

According to Faltinsen [23], hydrostatic and mass considerations determine the restoring forces acting on a freely floating body. When the submerged volume of the body exhibits symmetry in the x-z plane, only certain coefficients will have non-zero values, and they are expressed as

$$C_{33} = \rho g A_{wp} \tag{4.25}$$

$$C_{35} = C_{53} = -\rho g \iint_{A_{wp}} (x) ds \tag{4.26}$$

$$C_{44} = \rho g V (z_B - z_G) + \rho g \iint_{A_{wp}} (y^2) ds = \rho g V \overline{GM}_T \tag{4.27}$$

$$C_{55} = \rho g V ((z_B - z_G)) \rho g \iint_{A_{wp}} (x^2) ds = \rho g V \overline{GM}_L \tag{4.28}$$

The waterplane area is represented by A_{wp}, the volume of water displaced by the body is denoted as V, and z_G and z_B indicate the center of gravity and buoyancy positions, respectively. The transverse and longitudinal metacentric heights are also denoted as $\bar{GM}_T$ and $\bar{GM}_L$.

It is important to note that if the mass of the body, denoted as M, is not equal to the product of buoyancy (ρV), the previously mentioned equations labeled as C44 and C55 become invalid. Therefore, the equations C44 and C55 can be expressed as follows:

$$C_{44} = \rho g V z_B - M g z_G + \rho g I_{wp_y} \tag{4.29}$$

$$C_{55} = \rho g V z_B - M g z_G + \rho g I_{wp_x} \tag{4.30}$$

4.4.4 Morison Equation

Morrison's equation frequently captures wave excitation, added mass effects, and viscous forces on slender circular structures. It is a long-wave approximation where the structure's diameter (D) should be small in relation to the wavelength λ. Morison is said to be valid for $\frac{\lambda}{D} \geq 5$. The equation consists of two terms representing the drag and inertial forces of the body. The equation is expressed as

$$f_N(t) = \rho \frac{\pi D^2}{4} dz C_M a + \frac{1}{2} \rho C_D dz u|u|, \tag{4.31}$$

where C_M and C_D are the mass and drag coefficients calculated empirically and dependent on several factors. Faltinsen [23] describes these factors as:

Reynolds number

$$R_e = \frac{u_{max} D}{\nu} \tag{4.32}$$

Roughness number

$$\epsilon = \frac{k}{D} \tag{4.33}$$

Keulegan-Carpenter number

$$KC = \frac{v_{max} T}{D} \tag{4.34}$$

Frequency parameter - Oscillatory viscous flow

$$\beta = \frac{R_e}{KC} = \frac{D^2}{\nu T} \tag{4.35}$$

Where:

v_{max}: Maximum particle velocity

T: Wave period [s]

μ: Kinematic viscosity $[\frac{m^2}{s}]$

D: diameter [m]

k: Characteristic cross-sectional dimension of the roughness on the body surface

Nevertheless, Re and KC depend on velocity and wave period (only KC), so they will vary during simulations. It is deemed impractical to account for this, given that it would not contribute to a comparison of the models, given that doing so would yield no benefit. Instead, constant values for Cd and Cm are used. All models employ the exact same values. Figure 6-6 in DNV-RP-C205 [7] is used to calculate the drag coefficient, assuming a roughness of 10^4 and a post-critical flow regime. So, $C_D = 0.80$. $C_M = 1 + C_A$, where C_A is the added mass coefficient, denotes the mass coefficient. As KC decreases with water depth, low KC values are anticipated for the majority of the spar. C_A can be assumed to be independent of KC for low KC values (< 3) and set to 1. Thus, C_A equals 1 and C_M equals 2.

Morison's equation can be modified to consider the current and moving body and calculate wind loads, where ρ represents the density of the considered fluid.

4.4.5 MacCamy-Fuchs Theory

When a body's size is significantly greater than the wavelength, it causes wave diffraction that disturbs the water's surface. Given that Morison's is valid when $\frac{\lambda}{D} > 5$ (Faltinsen, [23]), the slenderness of the structure in relation to the wavelength is of critical relevance. Therefore the inertia coefficient C_M needs to be adjusted if diffraction occurs because the structure affects the incoming waves.

By assuming a circular cross-section, the first-order wave excitation force can be calculated by using the analytical expression developed by MacCamy and Fuchs (Hegseth, [34]). Therefore an expression of force per unit length $dF(z)$ for a regular wave with unit amplitude is given by

$$dF(z) = \sum_{i=1}^{N} \frac{4\rho g \zeta_a \cosh(k(z+h))}{k\cosh(kh)} G\cos(\omega t - \epsilon - \alpha). \tag{4.36}$$

where

$$G = \frac{1}{\sqrt{(J_1'(ka))^2 + (Y_1'(ka))^2}} \tag{4.37}$$

$$tan\alpha = \frac{J_1'(ka)}{Y_1'(ka)} \tag{4.38}$$

where Y' and J' are the derivatives of the Bessel function. With this modification in the hydrodynamic model, MacCamy & Fuchs theory can provide reasonable predictions of the diffraction problem and lead to more accurate estimations for wave loads.

5 Structural Dynamics and Design

The dynamic behavior of a FOWT with a flexible tower, and rotating turbine moving in waves exhibits a complex interaction. The wind turbine experiences aerodynamic forces from the wind and hydrodynamic forces from the waves and current, as a result of these external loads, the FOWT experience displacement and oscillations.

5.1 Body Oscillations

As the structure moves, internal elastic energy forces are generated to return the structure to its initial position. Once the structure has reached equilibrium, the energy is transformed back into kinetic energy, which causes it to move in the opposite direction. The system's kinetic energy is once again transformed back into internal forces. This energy exchange allows for infinite repetition of the motion.

Vibration is also a type of motion that repeats itself after a certain amount of time. The time period is the length of time it takes for one cycle to complete, and the frequency is the number of cycles per unit of time. Without any external forces acting on the system, initial displacement causes free vibrations that oscillate at the system's natural frequency. When an external force is applied at the same frequency as the natural, the system will receive energy on a constant basis from the external force, which results in a persistent rise in response amplitude, which can excite resonance (Larsen and Bachynski, [43]).

To express oscillation, natural frequency, and resonance in a straightforward manner, a Single Degree of Freedom (SDOF) mass-spring-damper illustrated in Figure 5.1, can be used. The expansion of an SDOF system into a multi-DOF system is possible with a matrix-based equation of motion.

5.1.1 One Degree-of-Freedom System

Newton's second law of motion can determine the equilibrium between the external force, internal restoration, and damping force (Langen and Sigbjørnsson,[42]). The equation of motion for a system with one-DOF is given by:

$$m\ddot{u} + c\dot{u} + ku = Q(t) \tag{5.1}$$

Where m is the mass, k is the spring element expressing the stiffness, c is the damping element, and $Q(t)$ is the external force creating a displacement u as illustrated in Figure 5.1.

Figure 5.1: Illustration of one DOF system (Langen and Sigbjørnsson, [42])

5.1.2 Free Oscillation

The free oscillation occurs when a system vibrates in response to an initial displacement or velocity applied to the body without the presence of external forces. This vibrating system can experience two possible outcomes.

1. There is no damping $c = 0$, and the exchange of potential energy is kept constant, meaning that $Q(t) = 0$. This means the system maintains the vibration until the end of time.
2. There is damping, and the vibration will progressively decrease until the system stops.

Damping is defined as the system's ability to dissipate energy. Therefore, water is one of the most important sources of damping for an offshore structure. Viscous damping is the term used to describe the damping that occurs when a system vibrates in a fluid.

For free oscillation, the force $Q(t)$ is equal to zero. The equation of motion can then be given as:

$$m\ddot{u} + c\dot{u} + ku = 0. \tag{5.2}$$

Furthermore, the characteristic solution for a non-trivial solution can be expressed as:

$$s = \omega_0 \left(-\frac{c}{2m\omega_0} \pm \sqrt{\left(\frac{c}{2m\omega_0}\right)^2 - 1} \right), \tag{5.3}$$

where s is a complex constant and ω_0 is the natural frequency in $\frac{rad}{s}$, which can be found by

$$\omega_0 = \sqrt{\frac{k}{m}}. \tag{5.4}$$

Depending on the amount of damping, there are three distinct sorts of solutions to Equation 5.3. According to Larsen and Bachynski, [43], the three forms of damping are:

1. Sub-critical damping
2. Critical damping
3. Supercritical damping

It's important to mention that there won't be any oscillation if the damping is equal to the critical damping. The equation for critical damping c_{cr} is

$$c_{cr} = 2m\omega_0 = 2\sqrt{mk} \tag{5.5}$$

In practice, marine structures would never have damping of such magnitude, but c_{cr} serves as a good reference. Therefore, the equation of damping ratio ξ_d is presented as:

$$\xi_d = \frac{c}{c_{cr}} = \frac{c}{2m\omega_0} \tag{5.6}$$

The damping ratio can be used to determine supercritical and sub-critical damping. Damping is supercritical for $\xi_d > 1$, and the system exhibits a substantially damped motion without oscillation. For $\xi_d < 1$, damping is sub-critical, being the most typical probable condition for actual structures (Larsen and Bachynski, [43]). For a damped system, the natural frequency ω_0 is transformed into the damped natural frequency ω_d given by:

$$\omega_d = \omega_n \sqrt{1 - \xi_d^2} \tag{5.7}$$

In accordance with the damped natural frequency, the damped natural period is expressed as:

$$T_d = \frac{T_d}{\omega_d} \tag{5.8}$$

Figure 5.2, represents the free oscillation of a sub-critically damped system, including a representation of the damped natural period. It can be observed that the initial displacement, which is shown with a capital U in the figure, initiates an oscillatory motion that eventually decreases until it reaches zero. This is due to the damping in the system, which is causing the decay. The system's displacement problem has a solution that can be expressed as

$$u(t) = e^{-\xi_d \omega_d t}(A \sin(\omega_d t) + B \cos(\omega_d t)), \tag{5.9}$$

where A and B are integrational constants, which can be found when the initial conditions are known.

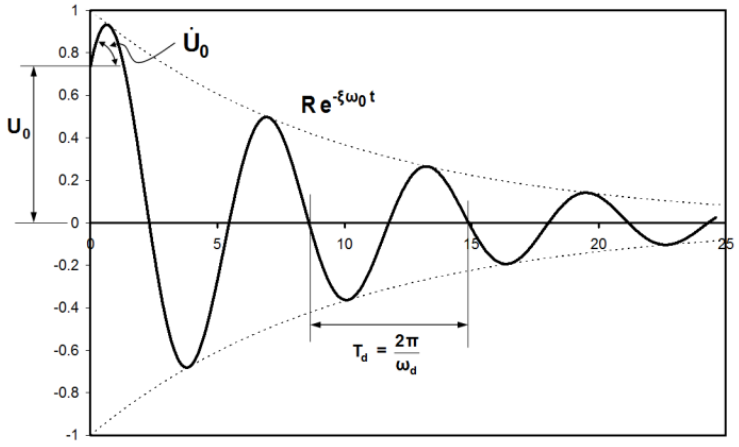

Figure 5.2: Free oscillation of sub-critically damped system, (Larsen and Bachynski,[43])

5.1.3 Forced Oscillation with Simple Harmonic Load

Based on Equation 5.1, the equation of motion of a harmonically varying load Q_0 and circular frequency ω is

$$m\ddot{u} + c\dot{u} + ku = Q_0 \sin(\omega t). \tag{5.10}$$

The ratio of the amplitude of the resulting harmonic response to the static displacement is known as the Dynamic Load Factor (DLF), expressed as:

$$DLF = |\frac{u_{max}}{u_{st}}| = \frac{1}{[(1-\beta^2)^2 + (2\xi_d\beta)^2]^{\frac{1}{2}}}, \tag{5.11}$$

where β is the frequency ratio, which can be found by:

$$\beta = \frac{\omega}{\omega_n} \tag{5.12}$$

If the imposed frequency of a floating spar reaches its natural frequency, the system will experience resonance. This can result in significant motion amplitudes, especially for FOWTs. Additionally, if any of the system's degrees of freedom have natural periods within the wave frequency spectrum, they may be excited by wave motion. Nonlinear effects may also become significant and cause high or low-frequency motion during prolonged periods of motion.

5.1.4 Measurement of Damping

A decay test can be used to determine the natural periods and damping of a structure. This type of test involves applying an initial offset to the system and observing its oscillatory behavior without disturbance. The logarithmic decrement technique (Larsen and Bachynski,[43]) can be used to calculate the natural periods by assuming that the amplitudes follow a logarithmic decline, according to the following equation:

$$\Lambda = \frac{1}{n} ln \frac{u_i}{x_{i+1}} \tag{5.13}$$

Where Λ represents the logarithmic descent, u_i is the initial amplitude, and u_n is the amplitude with n peaks away from u_i. As the logarithmic decrement is proportional to the damping ratio, it can be described as:

$$\Lambda = 2\pi\xi_d \frac{\omega_0}{\omega_d}. \tag{5.14}$$

According to Larsen and Bachynski [43], ξ_d is often considered as a small number, and the following approximation can therefore be made:

$$\omega_0 \approx \omega_d. \tag{5.15}$$

By inserting Equation 5.15 into Equation 5.14 gives the following expression:

$$\Lambda = 2\pi\xi_d \tag{5.16}$$

Furthermore, it can be rearranged and inserted into Equation 5.13, which yields

$$\xi_d \simeq \frac{1}{2\pi n} ln \frac{x_0}{x_n}. \tag{5.17}$$

The damped natural frequency is derived from the decay test period of oscillation, and the natural angular frequency may be calculated by rearranging Equation 5.7 giving the expression:

$$\omega_n = \frac{\omega_d}{\sqrt{1-\xi_d^2}} \tag{5.18}$$

It is now possible to calculate the natural period T_n and the natural frequency f_n by using:

$$T_n = \frac{2\pi}{\omega_0} \tag{5.19}$$

$$f_n = \frac{1}{T_n} \tag{5.20}$$

5.2 Structural Modeling

Structural dynamic analysis of a floating flexible structure can be performed at different levels of accuracy, ranging from a simple linear rigid body approach to more detailed nonlinear beam and finite element models. The non-linearity models are often applied to materials, blades, and force boundary conditions (Bachynski, [11]). The more general elements are considered as:

- 2D - Bar Elements: Bar with axial force applied to the mooring systems.
- 2D - Beam Elements: Beam with axial force, bending and torsional moment applied to the tower and blades.

There are many different flexible dynamic models, which will be discussed accordingly.

5.2.1 Beam Formulation and Euler-Bernoulli

According to the Euler-Bernoulli beam theory, the material is linear elastic according to Hooke's law, and plane sections stay plane as well as perpendicular to the neutral axis. Furthermore, equilibrium equations are developed by assuming equilibrium in the x-direction for an infinitely small beam element. As a result, the equations for shear force and moment are given as

$$q(x) = \frac{dV}{dx} \tag{5.21}$$

and

$$V(x) = \frac{dM}{dx} \tag{5.22}$$

By considering an infinitely small beam element under bending with a small angle between the z-axis and the bar element local coordinate system, the curvature of the beam κ can be estimated as

$$\kappa = \frac{d^2v}{dx^2}, \tag{5.23}$$

where v is the transverse displacement. $\frac{d^2v}{dx^2}$ is the transverse displacement change per unit length. Furthermore, an expression of curvature can be written as

$$\kappa = \frac{M}{EI}, \tag{5.24}$$

where E represents the elasticity modulus, and I represent the moment of inertia. By combining Equation 5.23 and Equation 5.24, one can obtain the following expression

$$\frac{d^2v}{dx^2} = \frac{M}{EI}. \tag{5.25}$$

By combining the equilibrium equations, Equation 5.21 with Equation 5.22, result in

$$q(x) = -\frac{d^2M}{dx^2}. \tag{5.26}$$

The Euler Bernoulli equation can be found by inserting Equation 5.26 with Equation 5.25

$$-q(x) = \frac{d^2}{dx^2}(EI\frac{d^2v}{dx^2}) \tag{5.27}$$

By taking the derivative of Equation 5.27, an expression for the moment and shear force can be established:

$$M = -EI\frac{d^2v}{dx^2} \tag{5.28}$$

$$V = \frac{d}{dx}\left(EI\frac{d^2v}{dx^2}\right) \tag{5.29}$$

The bending stress σ_b can be determined if the load-induced displacement has been established. For pure bending, the equation becomes

$$\sigma_b = \frac{M_z}{I} = -zE\frac{d^2v}{dx^2}, \tag{5.30}$$

where z is the distance between the neutral axis and an observed point.

5.2.2 Nonlinear Beam Element

A nonlinear beam element is a type of structural element used in Finite Element Analysis (FEA) to model the behavior of beams that exhibit nonlinear behavior. This type of element is commonly used to model the behavior of beams under large deformations, such as those that occur when a structure is subjected to significant loads or impacts. Nonlinear beam elements can be used to accurately predict the response of a structure too complex loading conditions by using beam, shell, or solid elements.

5.2.3 Time Domain Finite Element (FE) Formulation

The time domain FE formulation involves dividing the structure into a set of discrete elements, each of which is described by a set of equations that describe its behavior. The externally applied load equals the virtual work absorbed by the inertial, dissipative, and inertial forces (Bachynski, [11]), and can be written as

$$\boldsymbol{M_g}\ddot{D} + \boldsymbol{B_g}\dot{D} + R^{int} = R^{ext}, \tag{5.31}$$

where $\boldsymbol{M_g}$ and $\boldsymbol{B_g}$ are the global element mass and damping matrices, respectively. Further, D, R^{int}, and R^{ext} are the displacement vector, internal reaction force, and excitation loads, respectively. The latter includes aerodynamic, hydrodynamic, and controller loads. This system describes a coupled second-order differential equation that behaves continuously in time.

5.3 Control System

The main objective of operating a wind turbine is to minimize operational costs while maximizing power output. The operating cost of a wind turbine largely depends on the conditions under which it produces power. Figure 5.3 shows the relationship between mean rotor speed, generator power, generator torque, and blade pitch angle as a function of wind speed. The different regions in the figure represent the different operating modes of the controller. Optimizing the wind turbine's operating conditions makes it possible to reduce operational costs and increase power output.

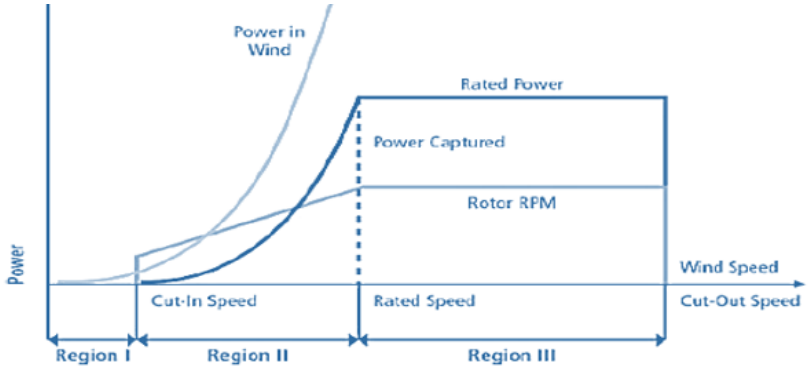

Figure 5.3: Operational strategy for a variable-speed pitch-regulated wind turbine. (Bachynski, [12])

The curve has three regions: Regions II and III represent the partial load zone and the full load region, respectively. When the wind speed is lower than the cut-in speed, the wind turbine produces no energy since the operation cost exceeds the power production's value. Furthermore, when wind speeds are above the cut-out wind speed, the wind turbine is shut down to prevent the systems from wind overloads. The following is a description of what happens in the two power-producing regions:

Region II:
The partial load area is between the cut-in and rated wind speeds. The wind turbine in this region is programmed to produce as much power as feasible. To attain the highest power coefficient, the control system increases the rotor speed as the wind speed increases.

Region III:
The full load region is found between the rated wind speed and the cut-out wind speed. It indicates that the output power is kept at a rated value to decrease structural stresses and hence fatigue damages.

A Wind turbine uses blade pitch to regulate the rotational speed to control the power production and loads. When the wind speed exceeds the maximum rated speed, the wind turbine's control system adjusts the blade pitch to maintain the rotor speed within working limitations. This control method, known as pitch regulation, is crucial in maximizing energy capture while minimizing loads.

5.4 Limit States

The concrete hull is controlled for preliminary sizing under different environmental loads when establishing a preliminary model analysis. A limit state is a condition beyond which a structure or structural component will no longer satisfy the design requirements. In the limit state method, partial factors are applied to the loads and to the characteristics resistance of the elements. The limit state method includes the following.

1. Ultimate Limit State (ULS): Represents the maximum capacity of a structure when subjected to extreme forces, considering its structural strength and the potential for failure.

2. Fatigue Limit State (FLS): pertains to the risk of structural failure caused by repeated or cyclic loading over time. It focuses on the structural integrity and endurance under such loading conditions.

3. Accidental Limit State (ALS): The Accidental Limit State requires that a structure is designed to withstand unforeseen or accidental loads without experiencing collapse or significant damage. It emphasizes the robustness and resilience of the structure.

4. Service Limit State (SLS): Encompasses criteria that ensure the structure's normal use, functionality, and durability throughout its intended service life. It aims to maintain the structure's performance and safety under expected operational conditions.

For this master thesis, the limit states considered are ULS in terms of buckling of the concrete hull, and FLS in terms of fatigue of the concrete hull and steel tower.

5.4.1 Concrete

The structural design of the Prestressed Concrete (PC) floater is based on the results of a time-domain analysis. Equations are employed to assess ultimate strength by considering the yielding of PC steel, bending and shear cracks, and shell buckling.

Pretension and Concrete Capacity

The necessary pretension to avoid cracks in the surface of the concrete can be computed using

$$P_e = \frac{\frac{M_d}{W_t} - \sigma_{tb} - \frac{N_d}{A_c}}{\frac{1}{A_c} + \frac{e}{W_t}}, \tag{5.32}$$

where P_e is the required amount of pretension, M_d and N_d are the maximum bending and axial force, W_t is the section modulus, A_c is the concrete area, e is the horizontal distance from the pretension wire to the center of the cross-section, and σ_{tb} is the flexural tensile strength (Oh et al. [55]). σ_{tb} is estimated by using concrete design strength f_{ck} as shown in Equation 5.33.

$$\sigma_{tb} = 0.56\sqrt{f_{ck}} \tag{5.33}$$

The bending crack occurrence is evaluated using the ratio between the axial stress and the allowed compressive stress. The evaluation carried out by EC2 [1] involved assessing short-term stress σ_S and long-term stress σ_L, as defined in Equation 5.34 and 5.35, respectively.

$$\sigma_S = \frac{P_{max} + N_d}{A_c} + \frac{M_d}{W_t} \tag{5.34}$$

$$\sigma_L = \frac{P_{max} + N_d}{A_c} \tag{5.35}$$

where P_{max} is the maximum priestesses tension force

To avoid cracks in the longitudinal direction, micro-cracks, or creep deformations that can lead to unacceptable effects on the structure, compressive stresses in the concrete must be limited. If the stress level for the given load combination exceeds the critical value, cracks may occur in the longitudinal direction. This can lead to a reduction in the durability of the concrete, and therefore, compressive stresses should be limited for concrete in environmental classes XD, XF, and XS. The long-term $\sigma_c(L)$ and short-term $\sigma_c(S)$ allowable compressive stress is therefore reduced using Equation 5.36 and 5.37 represent the respective stresses.

$$\sigma_c(L) = 0.45 f_{ck} \tag{5.36}$$

$$\sigma_c(S) = 0.60 f_{ck} \tag{5.37}$$

The evaluation of the shear crack incidence was conducted by means of the stress ratio between σ_1, as defined in Equation 5.38, and the tensile strength of the concrete.

$$\sigma_1 = \frac{(\sigma_x + \sigma_y)}{2} + \frac{1}{2}\sqrt{((\sigma_x - \sigma_y)^2 + 4\tau^2} \tag{5.38}$$

The axial stress is represented by σ_x, the circumferential stress is defined by σ_y, and the shear stress is characterized by τ. The estimation of σ_y is derived from the hydrostatic pressure. The calculation of the tensile strength of concrete, denoted as f_t, is performed using Equation 5.39

$$f_t = 0.23(f_{ck})^{\frac{2}{3}} \tag{5.39}$$

Another important design consideration is the thickness of the concrete in relation to water pressure. Ensuring that the total internal pressure does not exceed $\sigma_c(L)$ is crucial. It is worth noting that concrete has a significantly higher capacity, but for long-term stress, this limit is imposed. The minimum required thickness, denoted as t_{min}, can be calculated using the following equation:

$$t_{min} = \frac{\rho g d D_{ext}}{2 \cdot \sigma_c(L)}, \tag{5.40}$$

where d is the draft of the considered location and D_{ext} is the external diameter. In accordance with the EC2 [1], water-tight concrete should also have a thickness greater than 0.3 m.

Shell Buckling

Based on a reference [16], the shell buckling of the concrete structure was evaluated individually for water pressure, shear stress, and axial stress. First, the risk of shell buckling from water pressure was evaluated. With the use of Equation 5.41, the maximum permissible pressure to shell buckling was discovered.

$$P_{k0} = \frac{n^2 - 1}{12} \cdot \frac{E_c}{1 - \upsilon^2} \cdot \left(\frac{t_c}{r_o}\right)^3 \tag{5.41}$$

where P_{k0} is the upmost permissible pressure, n is the number of buckling lobes, E_c is the Young's modulus, υ is the Poisson's ratio for concrete, t_c is the wall thickness, and r_o is the section's outer radius. Shell buckling due to shear stress was evaluated using the maximum torsional shear stress τ_{k2} calculated with Equation 5.42, where r_i is the inner radius and T_k is the maximum torsional moment calculated with Equation 5.43, where P_w is the water pressure.

$$\tau_{k2} = \frac{2 T_k r_o}{\pi(r_o^4 - r_i^4)} \tag{5.42}$$

$$T_k = 0.85 T_{k0} \left(1 - \frac{P_w}{P_{k0}}\right)^{\frac{3}{4}} \tag{5.43}$$

$$T_{k0} = \frac{1}{3}\sqrt{\frac{2}{3}(n^2 - 1)} \cdot \frac{\frac{E_c}{\pi}}{(1 - \upsilon^2)^{\frac{3}{4}}} \cdot \sqrt{2 r_0 t_c^5} \tag{5.44}$$

Shell buckling due to axial stress was evaluated by calculating the maximal axial stress under torsional shear, $\sigma_k^{'}$, with Equation 5.45.

$$\sigma_k^{'} = \sigma_k \left(1 - \left(\frac{\tau_t}{\tau_{k2}}\right)^n\right) \tag{5.45}$$

where τ_t is the shear stress and σ_k is the axial compression buckling stress derived from Equation 5.46.

$$\sigma_k = \frac{E_c}{\sqrt{3(1-\upsilon^2)}} \cdot \frac{t_c}{r_o} \cdot 0.4 \tag{5.46}$$

5.4.2 Fatigue

All structures subjected to dynamic loads experience fatigue. These loads may include variations in temperature, corrosion, wind, and wave loads such as those encountered on FOWT. This is especially true for metal-constructed structures. The welds of these structures are especially vulnerable to fatigue.

Stages of Crack Growth

If the loads exceed a specific threshold, they can cause microscopic cracks in the structure that grow over time until a critical point is reached and the structure fractures. It is crucial to note that these stresses alone are inadequate to cause a structure to fracture. However, if the entire lifetime is considered, such as 10^8 cycles, it may significantly affect the structural integrity of the offshore structure. During this time span, a growing crack can be observed in three distinct periods (Berg and Ås,[13]):

1. N_i: Initiation time
2. N_g: Crack growth
3. Final failure
   The total fatigue life: $N_T = N_i + N_g$

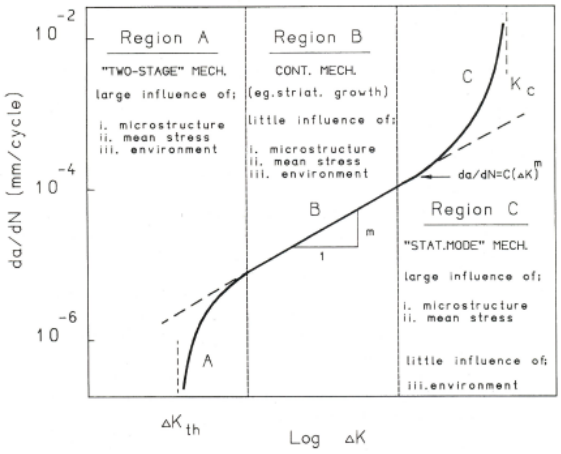

Figure 5.4: Schematic crack growth rate curve (Berg and Ås, [13])

The crack growth rate under a cyclic loading condition should be discussed before discussing SN curve theory. Since the values are significantly below the material's yield stress in these conditions,

Linear Elastic Fracture Mechanics (LEFM) can be used to predict how quickly cracks will form. This situation is illustrated by area region B in Figure 5.4. The crack growth relation for a given cyclic stress is

$$\Delta K = \Delta S \sqrt{\pi a} F(a), \tag{5.47}$$

where ΔS is the nominal stress range, a is the initial crack length, and $F(\alpha)$ is the form function of the stress intensity factor. The form factor depends on external geometry, loading configuration, crack length, and geometry.

Focusing on the finite life region, region B in Figure 5.4 is considered when computing fatigue assessments. The crack growth curve in region B will be approximated by a straight line given the Paris-Erdogan crack growth relation, also known as Paris's law:

$$\frac{da}{dn} = C(\Delta K)^m, \tag{5.48}$$

where C and m are material parameters dependent on the type of fatigue detail.

The S-N Curve

The S-N curve can be used to compare the dynamic stresses against the number of cycles for a distinct measurement. The parameters used are empirically derived by defining the fatigue resistance of a structure. Therefore, for the finite life region, the data can be defined as:

$$N(\Delta S)^m = A, \tag{5.49}$$

where A is a constant. The SN diagram is a log-log scale equation for the stresses and cycles. This means that Equation 5.49 can be turned into Equation 5.50, where the slope of the SN curve is expressed as $-\frac{1}{m}$.

$$log\Delta S = -\frac{1}{m} logN + \frac{1}{m} logA \tag{5.50}$$

The Haibach Model

Structures subjected to environmental loads may experience stress ranges above and below the fatigue limit, which can lead to crack growth. The cycles above the fatigue limit are known as active cycles. As the crack grows, the fatigue limit decreases, increasing more active cycles. Using a fatigue limit obtained from constant amplitude testing in cumulative calculations can result in a non-conservative design. On the other hand, ignoring the fatigue limit completely can lead to a too-conservative design. To account for the influence of a developing crack on the fatigue limit in cumulative damage estimates, Haibach developed a fracture mechanics model based on a fictional extrapolation of the SN curve with a slope of $(2m-1)^{-1}$. This model is applicable to stationary load histories, which is a reasonable approximation for wave-loaded structures like ships and offshore structures that experience many cycles (Berg and Ås, [13]). The SN curve is illustrated in Figure 5.5.

Irregular Load History

It is essential to emphasize that when evaluating fatigue capacity, it is important to consider the irregular load histories to which the structure will be subjected. One crucial factor to consider is

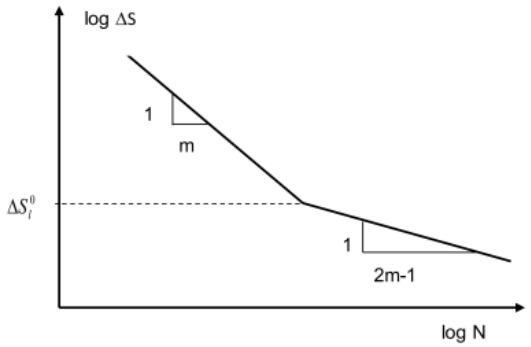

Figure 5.5: SN curve extrapolation for calculating cumulative damage, (Berg and Ås, [13])

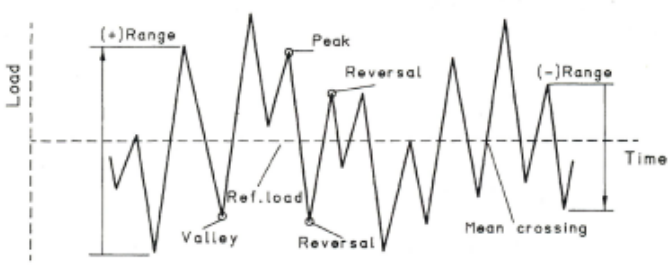

Figure 5.6: Term definitions for irregular load histories, (Berg and Ås, [13])

the variation in loading amplitude for steel structural components. As illustrated in Figure 5.6, the loading is stochastic, and this can significantly impact the structure's fatigue life.

The terms are described by Berg and Ås, [13] as:

- **Valley:**
  This is the instance where the first derivative of the load time history changes from negative to positive.
- **Peak:**
  This is the instance where the first derivative of the load time history changes from positive to negative.
- **Reversal:** The occurrence where the first derivative of load time history changes sign.
- **Mean Crossing:** The number of times that load time history crosses the mean loads level during a given length of the history.
- **Range:** The algebraic difference between a successive valley and peak loads.
- **Irregular Factor:** Irregularity defines the ratio between mean crossings with a positive slope and the number of peaks and valleys.

The cumulative damage analysis plays a crucial role in adding up and counting this irregular loading, also known as spectrum loading. The most often used counting methods are rain-flow counting, peak counting, level crossing counting, and basic range counting (Berg and Ås, [13]).

The rain-flow counting technique ensures that all peaks, including those with small amplitudes, are considered in the analysis. It is important to ensure that the cyclic stress-strain loops generated by the loading procedure are also taken into account during this process. These closed stress-strain loops, known as hysteresis loops, represent the dissipated energy due to material movement dislocation. The fatigue damage caused by a closed loop in a variable amplitude loading history is

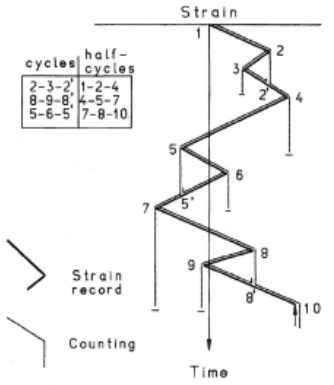

Figure 5.7: Rainflow analogy (Berg and Ås, [13])

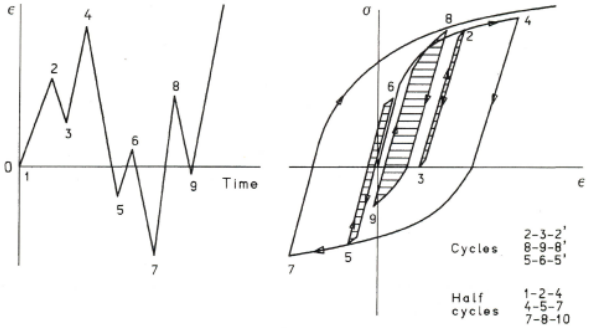

Figure 5.8: Formation of a hysteresis loop, (Berg and Ås, [13])

similar to the damage caused by a cycle with the same stress range in a constant amplitude fatigue test (Berg and Ås, [13]). Figure 5.8 illustrates the generation of a hysteresis loop.

Cumulative damage always represents a given value for a stochastic load history. The Palmgren-Miner (linear) summation is used, although multiple ways exist to compute cumulative damage from SN records. This method assumes that the damage caused by one cycle is constant for a given stress range (Berg and Ås, [13]).

$$D = \frac{1}{N} \tag{5.51}$$

Where N is the number of times the cycle leads to failure.

Further, the following is assumed in the failure criterion for the constant amplitude test.

$$D_{fail} \geq 1 \tag{5.52}$$

If various stress ranges ΔS_i are taken into account, each of which has a unique number of cycles n_i, the cumulative damage ratio is given by the following linear damage rule established by Palmgren and Miner:

$$D_{tot} = \sum_i \frac{n_i}{N_i} \tag{5.53}$$

The following Figure 5.9 represents this linear damage summation.

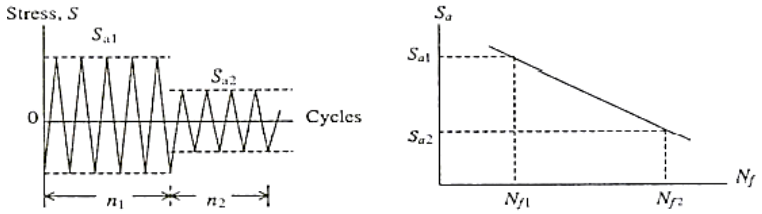

Figure 5.9: L: Stress blocks for constant amplitude. R: Stress blocks SN curve, (Berg and Ås, [13])

The resulting loads on a FOWT are given as axial loads and bending moments for dynamic analyses. The resulting stress in the tower and hull can then be calculated by

$$\sigma = \frac{N_x}{A} + \frac{M_y}{I_y} r \sin\theta + \frac{M_z}{I_z} r \cos\theta \tag{5.54}$$

Where N_x is the axial force, M_y, M_z is the bending moment about the local y- and z-axis. and (r, θ) is the location of interest on the cross-section in polar coordinates.

The time history of stress at a given point is computed in the SIMA analysis. With this data, Rainflow counting can be performed to compute the number of stress cycles.

For steel structures, the number of cycles until failure can be calculated based on the following equation:

$$log(N) = log(\bar{a} - mlog(\Delta\sigma(\frac{t}{t_{ref}})^k) \tag{5.55}$$

Where t_{ref} is the reference thickness and is the thickness exponent (= 25 mm for welded connections), and t is the actual thickness considered the potential fatigue crack will grow. It is important to know that this is applieble for reinforced concrete

5.4.3 Reinforced Concrete Under Fatigue

While the addition of steel reinforcement increases the tensile strength of concrete, making it more resistant to failure under large loads, it does not make the material immune to fatigue. In fact, reinforced concrete is susceptible to fatigue failure when it is subjected to repeated loading over time.

Offshore Concrete Structures DNV-OS-C502

Despite its limitations for concrete, a Palmgren-Miner rule is still used in the field, as specified by DNV - Offshore concrete structures, [60]. The standard studies the concrete and reinforcing individually.

Accordingly, the applied stresses are arranged in stress blocks with a constant amplitude corresponding to n_i stress cycles as provided in Equation 5.53, which is based on the cumulative linear damage theory. As shown in Table 5.1, the cumulative damage ratio depends on the accessibility for inspection and repair or whether it is positioned above or below the splash zone.

Concrete checking

Consequently, the service life of concrete exposed to cyclic loads may be calculated using the SN given in Equation 5.56.

Table 5.1: Cumulative damage ratios (DNV, [60])

No access for inspection and repair	*Below or in the splash zone (limited access) and with inspections planned*[1)]	*Above splash zone (readily accessible) and with inspections planned*[2)]
0.33	0.5	1.0

1) In typically harsh environments (e. g. the North Sea or equivalent) structural details exposed to seawater in the splash zone are normally considered to have no access for inspection and repair, i.e. the limit for the cumulative damage ratios shall be reduced to 0.33.
2) For reinforcement, which cannot normally be inspected and repaired, the limit for the cumulative damage ratio above the splash zone is 0.5.

$$logN = C_1 \frac{1 - \frac{\sigma_{max}}{C_5 f_{rd}}}{1 - \frac{\sigma_{min}}{C_5 f_{rd}}} \tag{5.56}$$

where:

f_{rd}: Compression failure strength

σ_{max}: Largest numerical compressive stress, taken as the average value within each stress-block

σ_{min}: The numerically least compressive stress, taken as the average value within each stress block. When σ_{min} is tension, it should be taken as zero when calculating the design life.

C_5: Fatigue strength parameter. For concrete, C_5 shall be taken equal to 1.0.

C_1: Shall be taken as:

- 12.0: For structure in air
- 10.0: For structures in water for those stress blocks containing stress variation in the compression-compression range
- 8.0: Structures in water for those stress blocks containing stress variation in the compression-tension range.

Furthermore, if the computed design life log N is greater than the value of X indicated by Equation 5.57, the design life can be improved by multiplying log N by the factor C_2 stated in Equation 5.58.

$$X = \frac{C_1}{1 - \frac{\sigma_{min}}{C_5 \cdot f_{rd}} + 0.1 \cdot C_1} \tag{5.57}$$

$$C_2 = 1 + 0.2(logN - X) > 1 \tag{5.58}$$

Steel reinforcement checking

$$logN = C_3 - C_4 log\Delta\sigma \tag{5.59}$$

Where:

$\Delta\sigma$: Is the stress variation of the reinforcement [MPa]

C_3&C_4: Factors dependent on the reinforcement type, bending radius, and corrosive environment.

σ_{max}: in the reinforcement shall be less than $\frac{f_{sk}}{\gamma_s}$, where γ_s is taken from Table 5.3

Table 5.2: Material coefficients for different materials (DNV, [60])

Material	*Symbol*	*Ultimate ULS*	*Fatigue FLS*	*Accidental ALS*	*Serviceability SLS*
Reinforced concrete/grout[3] (steel)	γ_c	1.50[1] (1.35)[2]	1.50[1] (1.35)[2]	1.30[1] (1.20)[2]	1.00
Steel reinforcement	γ_s	1.25[1] (1.15)[2]	1.10[1] (1.00)[2]	1.10[1] (1.00)[2]	1.00
Fibre reinforced concrete/grout	γ_c	1.50[1] (1.35)[2]	1.50[1] (1.35)[2]	1.30[1] (1.20)[2]	1.00
Plain concrete/grout,	γ_c	1.80	1.80	1.50	1.00

1) Design with these coefficients allows for tolerances in accordance with [6.3.6] or alternatively on cross-sectional dimensions and placing of reinforcements that do not reduce calculated resistance by more than 10%. If specified tolerances are in excess of those given in [6.3.6] or the specified tolerances lead to greater reductions in calculated resistance, the excess tolerances or the reduction in excess of 10% shall be accounted for in resistance calculations. Alternatively, material coefficients may be taken according to those given under note 2.

2) When the design is based on dimensional data that include specified tolerances at their most unfavourable limits, structural imperfections, placement tolerances as to positioning of reinforcement, then these material coefficients may be used. When these coefficients are used, any geometric deviations from the approved-for-construction drawings shall be evaluated and considered in relation to the tolerances used in the design calculations.

3) Material factors for reinforced grout may be used in design where the grout itself is reinforced by steel reinforcement or where it may be demonstrated that steel reinforcement or anchor bolts in the surrounding structure contribute to reinforce the grout (see [6.20]).

Table 5.3: Level of stress variations (DNV, [60])

	Level of stress variations [MPa]		
	$\Delta\sigma > 235$	$235 > \Delta\sigma > 65$	$65 > \Delta\sigma > 40$
C_3	15.7	13.35	16.97
C_4	4.5	3.5	5.5

Other Fatigue Standards

Many different and similar fatigue life prediction standards are available, and these will be listed under.

- Fatigue life according to NS-EN-1992-1-1
- Fatigue life according to Model Code 2010
- Fatigue life according to DNV - Guidelines for Design of Wind Turbines

5.5 Stochastic Analysis

Wind and wave loads will produce irregular responses on the FOWT that will change over time. Two approaches are thus provided when working with such data.

5.5.1 Time-Domain Analysis

The first is the Time Domain (TD) analysis, which considers how the data's amplitude changes over time. Given that it analyzes a large amount of data, this method will produce accurate results. As a result, complex problems like nonlinear and transient effects can be taken into account. The main disadvantage of this approach is that it takes a long time to compute.

5.5.2 Frequency-Domain Analysis

On the other hand, Frequency Domain (FD) analysis can be considered. Loads and responses are estimated in the FD using harmonic analytic methods or Laplace and Fourier transformations to solve equations of motion. Working with data such as load spectrum, response analysis, damage computation, and other analyses is convenient. However, FD analysis requires linearizing of the nonlinear term, which can result in an inaccurate solution. Furthermore, this analysis does not consider transient responses or nonlinear load effects from hydrodynamics and aerodynamics. However, a hybrid method considers both TD and FD analyses. In this scenario, Fast Fourier Transform (FFT) should be used to shift from one domain to another while maintaining reliability.

6 Material Characteristics

6.1 Concrete

Concrete is a type of composite material that is made up of different components. The main ingredients of concrete are aggregates, such as sand and gravel, and cement, which is a fine powder made from a mixture of minerals (Jacobsen, [39]). When water is added to the mixture of cement and aggregate, it reacts with the cement to form a paste that binds the aggregate together into a solid stone-like mass. The different components of concrete are shown in Figure 6.1. The proportions of the various components in a concrete mixture and how it is mixed and cured can affect its mechanical properties and performance.

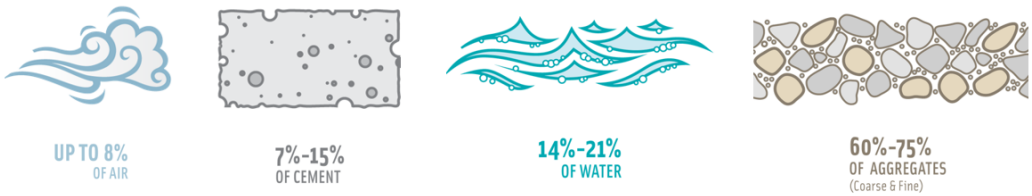

Figure 6.1: Components of concrete (PCA, [18])

In addition to its basic components, concrete can also contain other materials such as admixtures and reinforcement. Admixtures are added to the mix to improve workability, increase strength, or alter setting time. Overall, concrete is a complex and versatile material that is essential to modern construction. Its strength, durability, and cost-effectiveness make it a popular choice for a wide range of applications.

6.1.1 Characteristic Strength

When expressing the compressive and tensile strength of the concrete, the Eurocode 2 [1], and the European Standard EN 206-1 [50], relate the characteristics of the concrete material in great detail. Figure 6.1 also lists the relevant mechanical properties of concrete as well as compressive and characteristic strengths for f_{ck}. Depending on the type of cement, temperature, and curing circumstances, the compressive strength of the concrete decreases with age. Specifically, Equation 6.1 may be used to predict the compressive strength of concrete at different ages with a mean temperature of 20°Celsius and curing in line with EN 12390 (Jacobsen, [39]).

$$f_{cm}(t) = \beta_{cc}(t) f_{cm}, \tag{6.1}$$

where $f_{cm}(t)$ is the mean concrete compressive strength after t days, f_{cm} is the mean concrete compressive strength after 28 days, and β_{cc} is the concrete's age-dependent coefficient in days.

$$\beta_{cc}(t) = exp\left[s\left[1 - \left(\frac{28}{t}\right)^{\frac{1}{2}}\right]\right] \tag{6.2}$$

where:

t: Concrete age in days.

s: Cement type coefficient

(a) Class R: 0.20, Class N: 0.25, Class S: 0.38

The elastic deformation of the concrete is another crucial factor to consider. More specifically, the modulus of elasticity, E_{cm}, is established in Figure 6.1 for concretes using quartzite aggregates. This is because the component's modulus of elasticity determines the concrete's elasticity. According to Jacobsen [39], values for aggregates made of limestone and sandstone should be decreased by 10% and 30%, respectively, and raised by 20% if basalt aggregates are used. A variant of such a modulus can also be discovered by:

$$E_{cm}(t) = \left(\frac{f_{cm}(t)}{f_{cm}}\right)^{0.3} E_{cm} \tag{6.3}$$

Where $E_{cm}(t)$ is the value at (t) days, and E_{cm} is the value at 28 days.

Table 6.1: Concrete characteristics, (NS-EN 206, [50])

Strength classes for concrete															Analytical relation / Explanation
f_{ck} (MPa)	12	16	20	25	30	35	40	45	50	55	60	70	80	90	
$f_{ck,cube}$ (MPa)	15	20	25	30	37	45	50	55	60	67	75	85	95	105	
f_{cm} (MPa)	20	24	28	33	38	43	48	53	58	63	68	78	88	98	$f_{cm} = f_{ck}+8$(MPa)
f_{ctm} (MPa)	1,6	1,9	2,2	2,6	2,9	3,2	3,5	3,8	4,1	4,2	4,4	4,6	4,8	5,0	$f_{ctm}=0{,}30\times f_{ck}^{(2/3)} \leq$ C50/60 $f_{ctm}=2{,}12\cdot\ln(1+(f_{cm}/10))$ > C50/60
$f_{ctk,\ 0.05}$ (MPa)	1,1	1,3	1,5	1,8	2,0	2,2	2,5	2,7	2,9	3,0	3,1	3,2	3,4	3,5	$f_{ctk;0.05} = 0{,}7\times f_{ctm}$ 5% fractile
$f_{ctk,0.95}$ (MPa)	2,0	2,5	2,9	3,3	3,8	4,2	4,6	4,9	5,3	5,5	5,7	6,0	6,3	6,6	$f_{ctk;0.95} = 1{,}3\times f_{ctm}$ 95% fractile
E_{cm} (GPa)	27	29	30	31	33	34	35	36	37	38	39	41	42	44	$E_{cm} = 22[(f_{cm})/10]^{0.3}$ (f_{cm} in MPa)
ε_{c1} (‰)	1,8	1,9	2,0	2,1	2,2	2,25	2,3	2,4	2,45	2,5	2,6	2,7	2,8	2,8	see Figure 3.2 $\varepsilon_{c1}(^0/_{00}) = 0{,}7\ f_{cm}^{0.31} < 2.8$
ε_{cu1} (‰)	3,5									3,2	3,0	2,8	2,8	2,8	see Figure 3.2 for $f_{ck} \geq 50$ Mpa $\varepsilon_{cu1}(^0/_{00})=2{,}8+27[(98-f_{cm})/100]^4$
ε_{c2} (‰)	2,0									2,2	2,3	2,4	2, 5	2,6	see Figure 3.3 for $f_{ck} \geq 50$ Mpa $\varepsilon_{c2}(^0/_{00})=2{,}0+0{,}085(f_{ck}-50)^{0.53}$
ε_{cu2} (‰)	3,5									3,1	2,9	2,7	2,6	2,6	see Figure 3.3 for $f_{ck} \geq 50$ Mpa $\varepsilon_{cu2}(^0/_{00})=2{,}6+35[(90-f_{ck})/100]^4$
n	2,0									1,75	1,6	1,45	1,4	1,4	for $f_{ck} \geq 50$ Mpa $n=1{,}4+23{,}4[(90-f_{ck})/100]^4$
ε_{c3} (‰)	1,75									1,8	1,9	2,0	2,2	2,3	see Figure 3.4 for $f_{ck} \geq 50$ Mpa $\varepsilon_{c3}(^0/_{00})=1{,}75+0{,}55[(f_{ck}-50)/40]$
ε_{cu3} (‰)	3,5									3,1	2,9	2,7	2,6	2,6	see Figure 3.4 for $f_{ck} \geq 50$ Mpa $\varepsilon_{cu3}(^0/_{00})=2{,}6+35[(90-f_{ck})/100]^4$

6.1.2 Exposure Classes

Concrete is used in different places and for various purposes. Therefore, the environmental stresses to which the concrete is exposed will be of varying art and strength. Deterioration of concrete structures can result in corrosion-induced carbonation, chloride attack, freeze/thaw attack, or attack from chemical substances. In most situations, the concrete is subjected to more than one of these exposure classes. In Figure 6.2, a detailed recommendation is provided for selecting the correct exposure class. for offshore marine structures class designation four in Table 6.2 is of relevance.

Table 6.2: Exposure classes (NS-EN 206, [50])

Class designation	Description of the environment	Informative examples where exposure classes may occur
1 No risk of corrosion or attack		
X0	For concrete without reinforcement or embedded metal: all exposures except where there is freeze/thaw, abrasion or chemical attack For concrete with reinforcement or embedded metal: very dry	Concrete inside buildings with very low air humidity
2 Corrosion induced by carbonation		
XC1	Dry or permanently wet	Concrete inside buildings with low air humidity Concrete permanently submerged in water
XC2	Wet, rarely dry	Concrete surfaces subject to long-term water contact Many foundations
XC3	Moderate humidity	Concrete inside buildings with moderate or high air humidity External concrete sheltered from rain
XC4	Cyclic wet and dry	Concrete surfaces subject to water contact, not within exposure class XC2
3 Corrosion induced by chlorides		
XD1	Moderate humidity	Concrete surfaces exposed to airborne chlorides
XD2	Wet, rarely dry	Swimming pools Concrete components exposed to industrial waters containing chlorides
XD3	Cyclic wet and dry	Parts of bridges exposed to spray containing chlorides Pavements Car park slabs
4 Corrosion induced by chlorides from sea water		
XS1	Exposed to airborne salt but not in direct contact with sea water	Structures near to or on the coast
XS2	Permanently submerged	Parts of marine structures
XS3	Tidal, splash and spray zones	Parts of marine structures
5. Freeze/Thaw Attack		
XF1	Moderate water saturation, without de-icing agent	Vertical concrete surfaces exposed to rain and freezing
XF2	Moderate water saturation, with de-icing agent	Vertical concrete surfaces of road structures exposed to freezing and airborne de-icing agents
XF3	High water saturation, without de-icing agents	Horizontal concrete surfaces exposed to rain and freezing
XF4	High water saturation with de-icing agents or sea water	Road and bridge decks exposed to de-icing agents Concrete surfaces exposed to direct spray containing de-icing agents and freezing Splash zone of marine structures exposed to freezing
6. Chemical attack		
XA1	Slightly aggressive chemical environment according to EN 206-1, Table 2	Natural soils and ground water
XA2	Moderately aggressive chemical environment according to EN 206-1, Table 2	Natural soils and ground water
XA3	Highly aggressive chemical environment according to EN 206-1, Table 2	Natural soils and ground water

6.1.3 Durability Classes

The European Standard EN 206-1 [50], divides concrete into different durability classes based on the environmental conditions and external stresses to which it will be exposed. These classes are defined in terms of the required levels of strength, permeability, and other characteristics of the concrete. The standard also provides guidelines for the composition of concrete mixtures, including the appropriate ratios of cement, water, and aggregate, as well as the use of additives such as air-entraining agents and water-reducing agents (Jacobsen, [39]).

The more challenging the external conditions and stresses that a concrete structure will be subjected to, the more robust and durable the concrete mixture must be. This may require higher-strength cement, lower water-to-cement ratios, and specialized additives to improve the concrete's resistance to freeze-thaw damage, chemical attack, and other forms of deterioration. Table 6.3 shows how the different durability classes and exposure conditions can be used to guide the selection of concrete mixtures for specific applications.

Table 6.3: Concrete mixture criteria for given exposure classes. (NS-EN 206, [50])

	Exposure classes																	
	No risk of corrosion or attack	Carbonation-induced corrosion				Chloride-induced corrosion						Freeze/thaw attack				Aggressive chemical environments		
						Sea water			Chloride other than from sea water									
	X0	XC 1	XC 2	XC 3	XC 4	XS 1	XS 2	XS 3	XD 1	XD 2	XD 3	XF 1	XF 2	XF 3	XF 4	XA 1	XA 2	XA 3
Maximum w/c[c]	–	0,65	0,60	0,55	0,50	0,50	0,45	0,45	0,55	0,55	0,45	0,55	0,55	0,50	0,45	0,55	0,50	0,45
Minimum strength class	C12/15	C20/25	C25/30	C30/37	C30/37	C30/37	C35/45	C35/45	C30/37	C30/37	C35/45	C30/37	C25/30	C30/37	C30/37	C30/37	C30/37	C35/45
Minimum cement content[c] (kg/m^3)	–	260	280	280	300	300	320	340	300	300	320	300	300	320	340	300	320	360
Minimum air content (%)	–	–	–	–	–	–	–	–	–	–	–	–	4,0[a]	4,0[a]	4,0[a]	–	–	–
Other requirements	–	–	–	–	–	–	–	–	–	–	–	Aggregate in accordance with EN 12620 with sufficient freeze/thaw resistance				–	Sulfate-resisting cement[b]	

[a] Where the concrete is not air entrained, the performance of concrete should be tested according to an appropriate test method in comparison with a concrete for which freeze/thaw resistance for the relevant exposure class is proven.

[b] Where sulfate in the environment leads to exposure classes XA2 and XA3, it is essential to use sulfate-resisting cement conforming to EN 197-1 or complementary national standards.

[c] Where the *k*-value concept is applied the maximum w/c ratio and the minimum cement content are modified in accordance with 5.2.5.2.

The six durability classes specified in the European Standard EN 206-1 have the designations shown in Table 6.4, where the letter M denotes the mass ratio and the letter F indicates exposure to freeze/thaw conditions. The two-digit numbers represent the most significant mass ratio for each class. Table 6.4 also indicates which durability classes satisfy the requirements for each exposure class, as indicated by a cross (X). In general, choosing the most cost-effective option among the durability classes that meet the requirements for a given exposure class is common. For example, for an internal house wall exposed to mild conditions (XC1), choosing the M60 durability class is typical, as this provides adequate performance at a reasonable cost. Choosing a higher-strength class such as M45 would be unnecessarily expensive in this case (Jacobsen, [39]).

Table 6.4: Selection of durability classes depending on exposure classes, (NS-EN 206, [50])

Exposure classes	Durability Classes					
	M-90	M-60	M-45	MF-45	M-40	MF-40
X0	X	X	X	X	X	X
XC1, XC2, XC3, XC4, XF1		X	X	X	X	X
XD1, XS1, XA1, XA2, XA4			X	X	X	X
XF2, XF3, XF4				X		X
XD2, XD3, XS2, XS3, XA3					X	X
XSA	Composition of concrete and protective measure to be defined separately. (verify at least M40)					

6.2 Steel Rebar Characteristics

Steel reinforcement, also known as rebar, is a common addition to concrete. It is typically high-strength steel and added as bars or mesh. The steel reinforcement is placed within the concrete and provides additional tensile strength to the material. This allows concrete to support larger loads and resist bending, shear, and tension forces. Two main types of steel reinforcement are used in concrete construction: passive and pre-stressed (Juliebø, [40]).

Passive reinforcement is the most common type, and it is used in most reinforced concrete structures. This type of reinforcement is placed within the concrete and remains inactive until loads are applied to the structure. When loads are applied, the steel reinforcement provides additional tensile strength to the concrete, allowing it to support larger loads and resist forces such as bending, shearing, and tension.

Pre-stressed reinforcement is another type of steel reinforcement used in concrete construction. In this type of reinforcement, the steel is placed within the concrete in a pre-stressed condition, meaning that it is under tension before any loads are applied. This provides additional tensile strength to the concrete and helps it to resist tensile forces. Pre-stressed reinforcement is typically used when the concrete is subjected to large tensile loads, such as long-span structures.

The effect of pre-stressed reinforcement on a concrete element can be seen in Figure 6.2. In case (a), passive reinforcement is shown, where the steel bars are placed within the concrete but remain inactive until loads are applied. In cases (b) and (c), pre-stressed reinforcement is shown, where the steel bars are placed in a pre-stressed condition before any loads are applied. After the loads are applied, the pre-stressed reinforcement helps the concrete resist tensile forces, as shown in case (c).

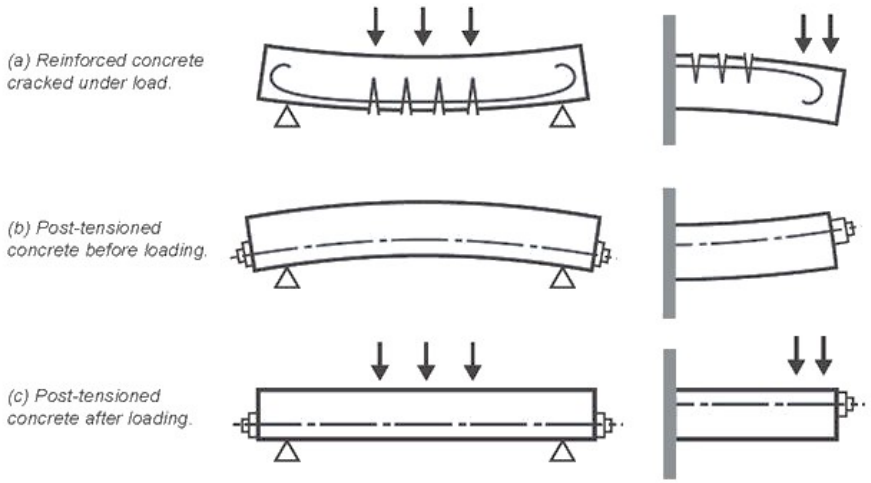

Figure 6.2: Principle of Prestressing, (Omib, [51])

According to Eurocode 2 [1], the steel reinforcement yield strength range f_{yk} should be between 400 MPa and 600 MPa. Additionally, the reinforcement should have adequate bendability to use the minimum mandrel diameter specified in Table 8.1 of Eurocode 2. These requirements ensure that the reinforcement is strong and flexible enough for use in concrete construction.

6.3 Material Composition for Spar

Based on the information above, it is now possible to determine what concrete quality best suits the structure in this thesis. The concrete quality B60 has been chosen for the concrete hull. This quality was selected based on the recommended combination with the durability class for the structure. The combination is based on recommendations from Norcem [49]. B60 is a dense concrete that is advantageous to use in constructions that are exposed to chlorides. The foundation is placed in seawater, so dense concrete is needed to prevent seawater from penetrating the reinforcement and causing corrosion.

The exposure class for the spar was obtained from Table 6.2 and set to XS3. This exposure class is chosen because the hull is of the marine structure type with tidal, splash, and spray zones. From Table 6.3, the minimum expected strength class for constructions in exposure class XS3 is set to B35. With the selected strength class of B60, the requirement is met. When the exposure class XS3 is selected, the requirement for durability is also set. Table 6.4 specifies the maximum durability class for constructions in XS3, which is M40 or MF40. This means that the concrete must have a water-cement ratio of less than or equal to 0.4. A low water-cement ratio indicates a higher cement content in the recipe and produces denser concrete. Dense concrete prolongs the reinforcement's penetration period, meaning it takes longer for the reinforcement to begin corroding.

The concrete's requirements for frost resistance must also be considered if the structure is exposed to subzero temperatures. Based on this, there is a risk of frost in the concrete. To take this into account, the durability class MF40 is chosen. This choice imposes a requirement on the concrete recipe. It must contain at least 4% air in its fresh state. To achieve 4% air in the concrete, an air-inducing agent is used in the concrete mixture. It is worth noting that a value of 6% is not desirable because it does not provide greater frost resistance but lower strength (Norcem, [48]). It is also important to note that the size and distribution of air-pores determine the frost resistance of the concrete (Norcem, [48]).

The material properties, including characteristic strength, safety factor, and Young's modulus, are summarized in Table 6.5, and will be used for the structural capacity in Section 9.6.2.

Table 6.5: Material properties: characteristic strength, safety factor, and Young's modulus

Material	$f_{ck}[MPa]$	γ_m	**E [GPa]**
Concrete	60	1.5	33.5
Post-tensioning steel	1540	1.15	190
Reinforcement steel	400	1.15	200

7 Optimization

Optimization aims to find the “optimal” design given a set of prioritized criteria or constraints. For example, birds optimize the shape of their wings in real-time, and dogs may determine ideal trajectories. Even more broadly, many physical laws, such as the idea of minimum energy, are related to optimization. Optimization sometimes means "improvement," although it is a more specific concept. Mathematically it is about finding the best feasible solution by changing variables that can be controlled and are often subject to constraints (Martins and Ning [46]). This section will review some important aspects of optimization described by Martins and Ning [46].

7.1 Formalism

To find the best design, an objective function f is needed. This function is a scalar quantity that can be computed for a given design variable vector x and is used to determine whether one design is better than another. The objective function can either be minimized or maximized, depending on the specific problem. Mathematically, the optimization problem can be expressed as follows:

$$\begin{aligned} \text{minimize} \quad & f(x) \\ \text{by varying} \quad & \underline{x}_i \leq x_i \leq \overline{x}_i \quad i = 1, ..., n_x \\ \text{subject to} \quad & g_j(x) \leq 0 \qquad j = 1, ..., n_g \\ & h_l(x) = 0 \qquad l = 1, ..., n_h \end{aligned} \tag{7.1}$$

The objective function measures a system's performance concerning some parameters selected by the designer. In most engineering sectors, numerous objectives are at risk, the most common of which are high performance and cheap costs. The objective function is then the result of a trade-off between these.

7.2 Optimization Methods

It is necessary to distinguish between gradient-free and gradient-based methods. Offshore engineering has predominantly utilized the former because they are simpler to employ. In addition, they can explore the design space defined by the number of design variables in use and are, therefore, likely to locate the global minimum of f in the region. These techniques include particle swarm, genetic algorithms, and the Nelder-Mead method (Martins and Ning [46]).

Gradient-based methods rely on the computation of the gradient of f to converge toward a minimum. As a result, they require differentiable objectives and constraint functions and their respective derivatives with the design variables. Despite these additional efforts, they outperform their gradient-free equivalents as the number of design variables increases. One disadvantage is that functions with highly irregular behavior are more likely to converge to a local minimum than a global minimum. This research intends to incorporate one of the most advanced gradient-based methods, the Sequential Quadratic Programming (SQP) algorithm (Martins and Ning [46]).

7.3 Design of Experiments (DOE)

DOE is a systematic method used to plan and execute experiments in order to collect data and gain insights into the relationship between input variables (factors) and the output response of a system. DOE enables the efficient exploration of the design space, enables the understanding of the effects of various factors, and facilitates the optimization of system performance. While DOE is a valuable design exploration and optimization method, it does not automatically ensure constraint satisfaction. It is important to carefully analyze and understand the reasoning behind constraint violations, refine the experimental design or model assumptions if necessary, and take appropriate corrective actions.

7.4 ScipyOptimizeDriver with COBYLA Algorithm

The ScipyOptimizeDriver in OpenMDAO provides an interface to the SciPy library's optimization algorithms. COBYLA (Constrained Optimization BY Linear Approximations) is one such algorithm, which is a gradient-free optimization method appropriate for problems with bound constraints. COBYLA is an algorithm without derivatives established on the Sequential Quadratic Programming (SQP) technique. It updates linear approximations of the objective and constraint functions iteratively within a trust region surrounding the current design point. This algorithm is beneficial for problems with objective and constraint functions that are non-differentiable or noisy.

The integration of COBYLA with ScipyOptimizeDriver provides numerous benefits. It permits the resolution of optimization problems with bound constraints without requiring derivative data. Additionally, COBYLA can effectively manage functions that are not smooth or noisy. However, it is essential to note that COBYLA is a gradient-free algorithm, meaning it may require more function evaluations than gradient-based methods. This can be computationally expensive for situations with many design variables or costly objective and constraint functions. In addition, COBYLA may perform inadequately for highly nonlinear and nonconvex optimization problems.

ScipyOptimizeDriver with the COBYLA algorithm provides a flexible and efficient method for gradient-free optimization problems with bound constraints. It allows for the exploration and optimizes complex design spaces within the OpenMDAO framework and is employed as the primary optimization technique in this thesis.

8 Modeling

This section provides an overview of the different models employed in the study. Firstly, the properties and geometry of the 10 MW spar are based on Oh.et al [55] are introduced in Section 8.1. Subsequently, the DTU 10 MW wind turbine is discussed in Section 8.2 with the tower characteristics presented in Section 8.3, and the mooring configuration is outlined in Section 8.4. The rigid, flexible, and linearized models are comprehensively summarized in Section 8.5. Following that, the modeling procedure involving GeniE, HydroD, WAMIT, and Riflex is described in Section 8.6. Lastly, the process of generating wind files using TurbSim is elaborated upon in Section 8.7.

8.1 10 MW Spar

The structures used in this study are based on a parametric design developed by Oh et al., which included three different spar designs with varying diameters and thicknesses. The two most recent spar designs were selected for this research, and the structural properties can be found in Table 8.1.

Table 8.1: SPAR Geometry

Parameter	**SPAR 1**	**SPAR 2**
Length [m]	145	145
Outer diameter [m]	16	17
Wall thickness [m]	0.45	0.55
Draft [m]	120	120
$M_{concrete}$ [kg]	7968709	10303236
$M_{ballast}$ [kg]	15005575	15858885
COG_z [m]	-76.5	-75.5
COB_z [m]	-60	-60
I_{XX}, I_{YY} $[kgm^2]$	2.0841e+11	2.3233e+11
I_{ZZ} $[kgm^2]$	8.9346e+08	1.1989e+09

8.2 The DTU 10 MW Reference Wind Turbine

The present study employs the DTU 10 MW reference wind turbine as the basis for analyzing the spar floater. The DTU 10 MW turbine, developed by the Technical University of Denmark, is extensively described in the publication by Bak et al. [2]. Notably, this turbine design is primarily intended for land-based applications. The design properties of the turbine, including relevant specifications and characteristics, are documented in Table 8.2, while a visual representation of the turbine can be found in Figure 8.1.

Table 8.2: Structural values for DTU 10 MW, [2])

Description	**Value**
Rating [MW]	10
Rotor orientation, configuration	Upwind, 3 blades
Rotor, Hub diameter [m]	178.3, 5.6
Hub height [m]	119
Cut-in, Rated, Cut-out wind speed [m/s]	4, 11.4, 25
Cut-in, Rated rotor speed [RPM]	6, 9.6
Rated tip speed [m/s]	90
Rotor mass [kg]	446E+03
Tower mass [kg]	628E+03

Figure 8.1: DTU 10 MW [2]

8.3 Tower

The tower weight from Oh et al. [55] was the only known parameter. Thus the turbine tower design from Hegseth [35] was utilized as a basis for modification. To align the tower weight with the findings of Oh et al., a multiplication factor of 1.19 was applied. As a result, the exact weight was achieved, with the corresponding diameters and wall thicknesses detailed in Table 8.3.

Table 8.3: 10 MW tower properties

Elevation wrt. SWL [m]	Outer Diameter [m]	Wall thickness [m]
25.0	8.30	0.0452
35.5	8.02	0.0431
46.0	7.74	0.0409
56.5	7.46	0.0386
67.0	7.18	0.0367
77.5	6.90	0.0345
88.0	6.62	0.0324
98.5	6.34	0.0302
109.0	6.06	0.0281
119.5	5.78	0.0259
130.63	5.50	0.0238

8.4 Mooring Configuration

The configuration of the mooring was determined based on the work of Oh et al. [55]. Figure 8.2 illustrates a catenary mooring system with three lines positioned at 120-degree angles. Table 8.4 outlines the specific parameters of this mooring system. In addition, the fairlead and anchor positions are shown in Table 8.5.

Table 8.4: Mooring parameters (*Taken from Oh et al. [55])

Parameter	Value
D_{moor} [m]	0.111
$z_{fairlead}$ [m]	-22.0*
L_{moor} [m]	850*
x_{moor} [m]	800*
EA_{moor} [N]	1.11e+09*
m_{moor} [kg/m]	224.8*

Table 8.5: Fairlead and anchor locations

Point	X	Y	Z
Fairlead 1 [m]	0.0	0.0	-22.0
Fairlead 2 [m]	0.0	0.0	-22.0
Fairlead 3 [m]	0.0	0.0	-22.0
Anchor1 [m]	850	0	-200
Anchor2 [m]	-425	736.12	-200
Anchor3 [m]	-425	-736.12	-200

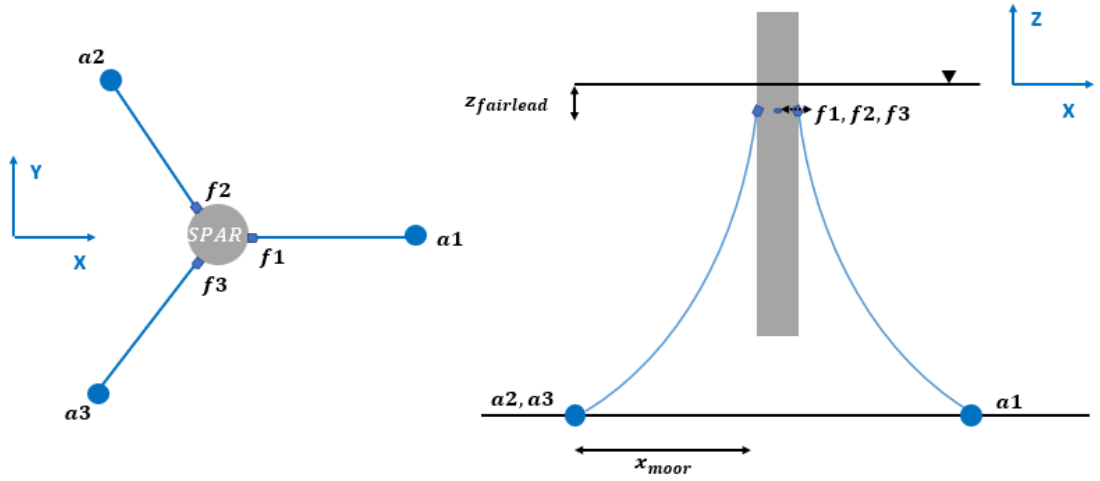

Figure 8.2: Anchor (a1, a2, a3) and fairlead (f1, f2, f3) locations in a mooring configuration

8.5 Models

Examining the different models being considered is essential before exploring the modeling approach detailed in Section 8.6. A comprehensive overview of all the models can be found in Table 8.6. Firstly, the Rigid model utilizes a GeniE panel model to represent a SIMO-body, accompanied by a stiff hull based on linear potential flow theory (PFT). More details about this model can be found in Section 8.5.1. Next, the flexible model incorporates RIFLEX components to emulate an elastic spar as discussed in Section 8.5.2, where WAMIT is utilized to generate radiation and diffraction loads for the FLEX design. Lastly, the SPAROpt model, presented in Section 8.5.3, provides a linear representation of the system with a flexible hull, employing a MacCamy-Fuchs Theory (MCF) wave model. It is important to note that the number of elements and DOF vary among these models, contributing to their distinct characteristics and capabilities.

Table 8.6: Structural models consepts

Name	**Rigid SPAR**	**Flexible SPAR**	**SPAROpt**
Tower Elasticity	Flexible	Flexible	Flexible
Hull Elasticity	Rigid	Flexible	Flexible
DOF's	6	6	3
Wave load model	PFT	PFT	MCF
Wind load model	BEM	BEM	LBEM

8.5.1 Rigid Model

The panel model for the Rigid spar hull was generated in GeniE using the measurements provided in Table 8.1. This panel model represents a continuous and rigid structure, disregarding any elasticity effects. To determine the hydrodynamic properties based on linear potential flow theory, a WADAM analysis was conducted using HydroD. The analysis output provided frequency-dependent added mass, damping, excitation, and hydrostatic stiffness data. However, since the values obtained from HydroD did not consider the presence of the concrete wall and ballast, an alternative method outlined in Section 4.4.3 was employed to calculate and update the values of C_{44} and C_{55}. Additionally, the HydroD moment of inertia was substituted with calculated values to ensure accuracy. Finally, a value for C_{66} was included to prevent numerical instability.

The quadratic drag is not accounted for in the WADAM analysis. Instead, the hull incorporates "slender elements" to incorporate this feature. The coefficient of quadratic drag ($C_D = 0.8$) is determined by Section 4.4.4. The SIMO body is then enhanced with a panel model, hydrodynamic features, and the inclusion of slender elements.

8.5.2 Flexible Model

The initial stage in the flexible Spar design involved developing a panel model in GeniE based on the geometry shown in Section 8.1, wich is created in the same manner as the Rigid model. To generate the required input files for the WAMIT integration, a WADAM analysis was performed using HydroD. For each panel, WAMIT was employed to compute frequency-dependent added mass, damping, and excitation forces. These values were then incorporated into SIMA's RIFLEX components utilizing the "Potential flow library" feature. The RIFLEX model utilized the "Potential flow with quadratic drag load coefficients" to account for quadratic drag. Consequently, no added mass coefficients were employed in FlexPFT.

8.5.3 SPAROpt Model

The model used in SPAROpt is a slender flexible beam. Each beam element has its own diameter, length, and thickness. In order to obtain hydrodynamic loads, the model uses MCF theory. The aerodynamic load model is based on a linearized BEM (LBM) model. The structural behavior is a combination of FEA and beam theory.

The FEA model captures the complex behavior of the structure, while the beam theory model provides a simplified description for overall system analysis. The FEA model analyzes the structure's stresses and deformations when subjected to different loads and portrays the structure's components, such as the tower, platform, and mooring system. The structure is represented as a collection of linked beams with lumped masses and stiffness attributes using the beam theory model. This reduces the structure's degrees of freedom to a reasonable amount, allowing for efficient system-level analysis. This model considers only three degrees of freedom: surge, pitch, and the first tower moment bending, as illustrated in Figure 8.3.

The support structure is modeled as a slender flexible beam with varying cross-sectional properties. The model is regarded as unsuitable for local blade response, and rotor design is considered outside the scope of the current work. The dynamic response of the blades is assumed to have a small effect on the support structure response and is therefore considered rigid. Consequently, the RNA is replaced by a point mass and inertia, with resultant aerodynamic loads acting on the tower top.

The main difference between SPAROpt and other models in SIMA is that SPAROpt serves two functions: fast frequency domain linearization for hydro-servo-elastic analysis, but does not allow for non-linearities. In contrast, SIMA is a time-domain tool that allows for nonlinearity but is also an aero-hydro-servo-elastic tool. The second function is that SPAROpt uses an OpenMDAO framework that is wrapped into the optimization model.

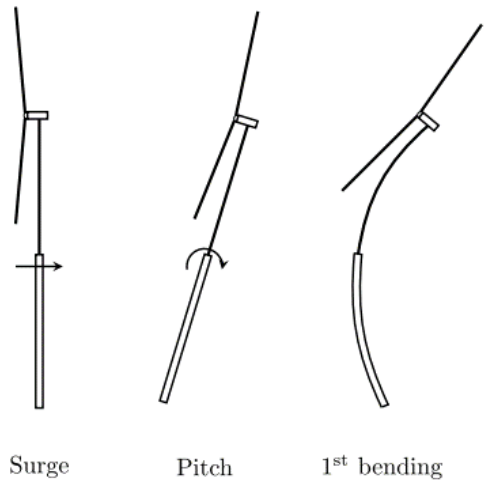

Figure 8.3: Structural DOFs considered in the SPAROpt model (Hegseth et al. [34])

8.6 Modelling Procedure

The modeling aspect of this thesis is described in this section. Section 8.6.1 provides a detailed explanation of the GeniE-modeling technique for panel models. Section 8.6.2 details the procedure for obtaining hydrodynamic attributes in HydroD. In addition, Section 8.6.3 explains the WAMIT integration procedure. Section 8.6.4 introduces RIFLEX elements used for modeling elasticity in towers and spars. Last, how the SPAROpt model is generated in Section 8.6.5.

8.6.1 GeniE

Panel models for the rigid spars were generated using GeniE. To reduce computational efforts, only one-fourth of the spar was modeled, taking advantage of the symmetry about the x and y-axis. The diameters of the spars were determined based on Table 8.1. Notably, no thickness or material density was considered for the structure, resulting in an underestimation of the mass moment of inertia (I) around the origin by HydroD, since the concrete walls and ballast were not included in the model. While the mass of the ballast was accurately accounted for, HydroD uses seawater instead of concrete. To ensure that the hull's surface experiences hydrodynamic loads and pressure, it was modeled as a wet surface, and a dummy hydrodynamic load was applied. The mesh utilized had an element length of 1 m, as shown in Figure 8.4b. Figure 8.4a showcases the panel model used for the Spar. Similarly, panel models for SPAR 2 were generated following the same methodology, except for the differing geometry. Additionally, GeniE was employed to create panel models for the Flexible spar designs, which were only used in HydroD to generate input files for WAMIT. It is important to note that these panel models were not utilized in the SIMA analyses of the Flexible spar. The modeling approach for the Flexible spar panel models was similar to that of the rigid models.

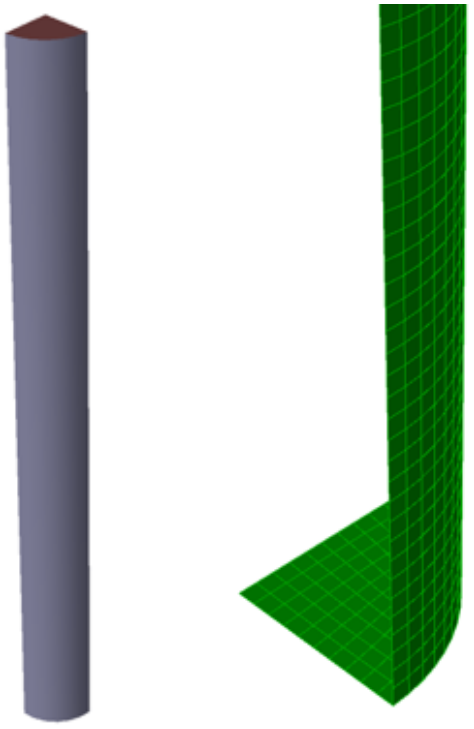

(a) Spar

(b) Mesh visualized

Figure 8.4: GeniE panel model

8.6.2 HydroD

The panel model was developed using GeniE, and HydroD was employed to derive the hydrodynamic characteristics. To address the fact that only a quarter of the spar was modeled in GeniE, the initial step involved implementing symmetry along the xz- and yz-axis. The desired draft was achieved without any trim by setting the SWL and trim to zero. The "Fill from buoyancy" feature in HydroD was utilized to accomplish the specified SWL and trim, generating the necessary input values. However, the COG was not at the correct height since HydroD employs seawater instead of the actual ballast density (3800 kg/m^3). This disparity will be corrected during the SIMA analysis. Nevertheless, given that the model's primary objective is to obtain hydrodynamic attributes, this discrepancy will have minimal impact on the resulting hydrodynamic data.

After confirming the accuracy of the draft and ensuring no trim, a specific direction and frequency set were defined. The range of directions spanned from 0 to 90 degrees in 15-degree increments, while the wave periods ranged from 4 to 20 seconds with a 0.5-second increment, and from 21 to 60 seconds with a 1-second increment. For the flexible designs, the input files for WAMIT were generated by selecting the "Save temp. WAMIT files" option prior to conducting the analysis. Finally, the WADAM analysis was executed within HydroD as the concluding step.

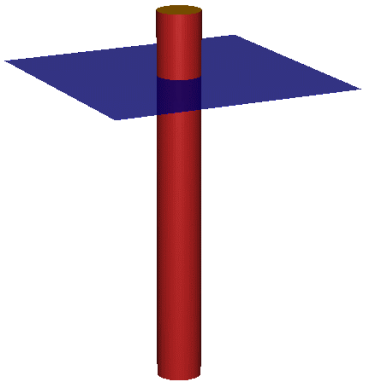

Figure 8.5: Spar visualization in HydroD

8.6.3 WAMIT

Upon generating the WAMIT input files in HydroD, certain modifications were necessary to ensure the proper information storage. The water depth was standardized to 200 m, wave periods and directions were aligned with those utilized in HydroD (Section 8.6.2), and COG of the entire FOWT assembly was incorporated based on the data from Oh et al., further validated by calculations derived from the COG points of all components. Additionally, it was crucial to specify the execution of the radiation and diffraction problems. The WAMIT analysis was subsequently performed, and the resulting output files were employed in a custom MATLAB script. This script harnessed the WAMIT results to transform the, ultimately generating WAMIT-type output files for each section. Before executing the MATLAB script, certain adjustments were made to align with the specific case's geometry. The script was designed based on the assumption of equal panel spacing throughout the entire spar, which was set at 4 m to align with the meshing and draft length.

The script obtained separate output files for each panel, encompassing frequency-dependent added mass, damping, and excitation forces. Another in-house program, SIMATOOL, was employed to create input files suitable for integration into the new feature in SIMA, the potential flow library. By specifying the hydrodynamic load formulation of the cross-sections as "Potential flow with quadratic drag load coefficients," it became possible to assign the hydrodynamic loads obtained from WAMIT to RIFLEX cross-sections through this approach.

8.6.4 SIMA

Figure 8.6 illustrates the SIMA model of the FOWT, featuring the spar design, turbine tower, RNA, and mooring for the rigid and flexible spar. In the case of rigid spars, the platform is incorporated as a "body" with specifications imported from HydroD. As previously explained, HydroD provides an estimated system mass based on the draft, excluding the concrete walls and ballast. When assembling the SIMA model, the tower and turbine are mounted on the platform. The platform body is modeled with the "gravity included" option, which ensures that SIMA finds equilibrium based on the weight and buoyancy of the modeled elements. However, this approach leads to the double counting of the tower and turbine weight, resulting in the FOWT sinking. To rectify this issue, two steps are taken.

Firstly, the platform is updated with its own mass coefficients, COG, and moment of inertia, as specified in Table 6.12, to account for the concrete walls and ballast. Secondly, a buoyancy force equal to the total mass force is applied at the platform's COB to restore equilibrium. Consequently, the FOWT determines its correct draft based on the registered weight and submerged volume.

One of the properties imported from HydroD is hydrostatic stiffness. C_{33} is accurate among the imported stiffness values. However, C_{44} and C_{55} must be adjusted using the equations mentioned in Section 4.4.3, considering only the parts relevant to the platform body. With the "gravity included" option, the equation simplifies to only the first term:

$$C_{44} = C_{55} = \rho g I_{wp} \tag{8.1}$$

Table 8.7: Hydrostatic stiffness data for the two models

Hydrostatic Coefficients	**SPAR 1**	**SPAR 2**
C_{33} $[N/m]$	2.0217e+06	2.2823e+06
C_{44} [Nm]	3.2348e+07	4.1225e+07
C_{55} [Nm]	3.2348e+07	4.1225e+07

For the flexible spars, RIFLEX elements with axisymmetric cross-sections are employed. Table 8.8 provides the two flexible spar's mass coefficients, external and internal cross-section area, gyration radius, and geometric stiffness.

Table 8.8: Cross-sectional properties for the two models

Parameter	**SPAR 1**	**SPAR 2**
Mass coefficient [kg/m]	54958.2	71057
Ext. area $[m^2]$	201.1	227.0
Int. area $[m^2]$	179.1	198.6
Gyration radius [m]	5.50	5.82
Axial stiffness [N]	7.364e+11	9.522e+12
Bending stiffness $[Nm^2]$	2.228e+13	3.224e+14
Shear stiffness [N]	3.069e+11	3.968e+12
Torsional stiffness $[Nm^2/rad]$	1.857e++13	2.687e+14

Since the spar geometry remains unchanged, a single section is created and replicated to form the structure. Froude-Krylov scaling is disregarded in the tangential direction (vertical direction in this case) for the spars, as explained in Section 4.6.3. Quadratic drag coefficients (Cd = 0.8) are incorporated for the spar models. The load formulation "Potential flow with quadratic drag load coefficients" is utilized. The beam formulation, which describes the behavior of these RIFLEX elements, can be found in Section 5.2.1. Bar elements with axisymmetric cross-sections represent the mooring lines and only deform in the axial direction [31].

Input values for the mooring, use the mass coefficient (224kg/m), external cross-section area (0.0097 m2), gyration radius (0.027 m), and axial stiffness (1.11 GN) are provided for the mooring lines. The blades, nacelle, and shaft are also modeled as beam elements. Although these components were not explicitly developed for this project, they were sourced from existing in-house models.

Since minimal attention was given to analyzing these parts of the FOWT, they will not be further elaborated upon.

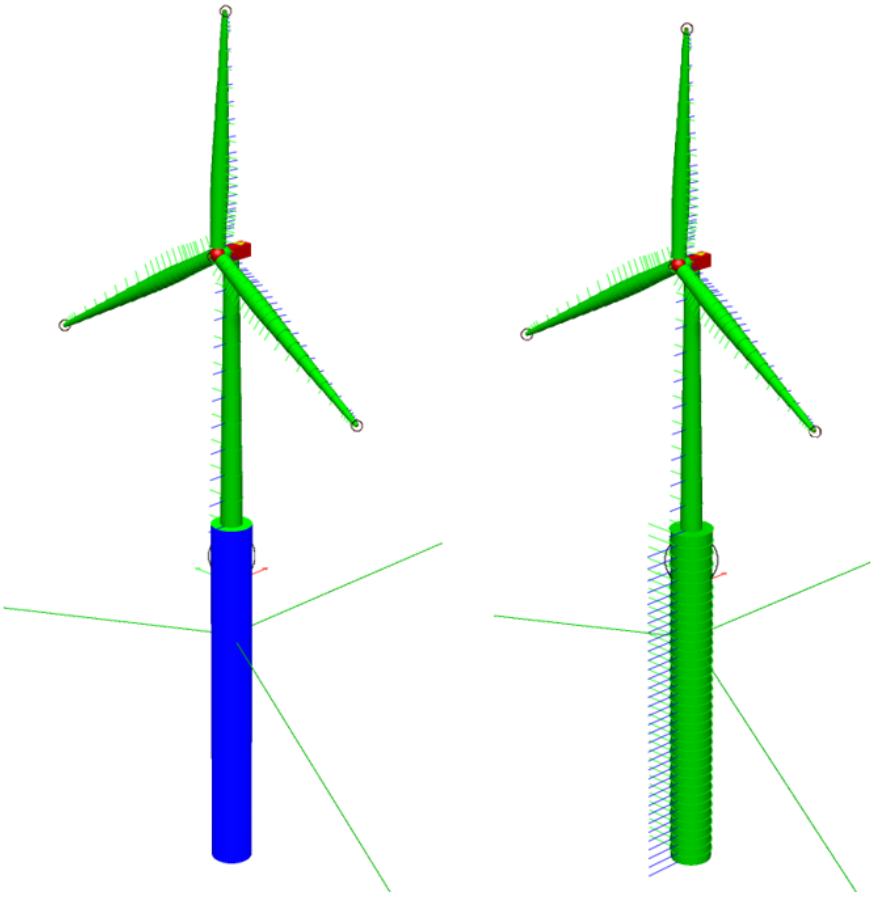

(a) RIGID (b) FLEXIBLE

Figure 8.6: Spar models visualized in SIMA

RIFLEX Correction

The axial forces from SIMA in RIFLEX need to be corrected because the current approach applies buoyancy and weight at the center of each section, overlooking the influence of pressure distribution. In reality, the buoyancy in an undeflected position for a spar is determined by both the pressure distribution at the bottom and the tapered segment. As a result, an adjustment is necessary to account for the upward force F_B applied at the bottom to ensure accurate modeling.

To obtain a more precise representation of the buoyancy and weight distribution, Souza and E.E. Bachynski-Polić have discussed an alternative methodology and derived the corresponding formulas (Souza and Bachynski-Polić, [57]). Their work provides insights into considering the pressure distribution at the bottom and the tapered segment when calculating the buoyancy forces in an undeflected position.

8.6.5 SPAROpt

The initial approach involves modifying the model by updating its geometry, mooring system, and ballast density. The original model only considers a steel hull. Thus a new material library was incorporated into the code. This library encompasses all the necessary material properties, such as the strength of concrete, rebar, and tension wire.

To begin with, the first step focuses on establishing a concrete library. This involves calculating the characteristic properties of concrete, including its density, compressive and tensile strength, and elasticity modulus. Additionally, the quality of the reinforcement is also implemented within this library. Once the structural properties are defined, a confirmation study is conducted to compare the structural properties of the concrete hull, COG of the ballast, COB, and the natural periods.

A distinctive feature of the SPAROpt model is that, through the process of modifying the design, all the necessary properties are adjusted to correspond with the considered geometry. However, it should be noted that a significant amount of time was dedicated to debugging to ensure the model's accuracy.

8.7 Controller & Wind Files

An in-house controller was provided for the 10 MW control system, and no modifications were performed on the controller. The controller setting determines the wind turbine's behavior and how it responds to variations in the wind, tip-speed ratio, and other factors. The control system aims to reduce loads for higher wind speeds and minimize power loss for low wind speeds.

The wind files employed in the simulations were generated using TurbSim, which is a stochastic, full-field turbulence simulator. These wind files were explicitly required for the irregular wave tests, and the wind speeds and turbulence intensities from Table 9.3 and Table 9.5 in Section 9.4 and Section 9.5 were utilized. Table 8.9 shows the parameters used to generate the TurbSim files in accordance with the Kaimal spectral model.

Table 8.9: TurbSIM inputs

Time-step	0.05 s
Hub Height	134 m
Grid height	200 m
Grid width	200 m
Vertical grid-point matrix dimensions	32
Horizontal grid-point matrix dimensions	32
Surface roughness length	0.0003 m

9 Result

In this section, the properties of FOWTs were thoroughly evaluated and compared. Firstly, the excitation, added mass, and damping behavior were assessed in Sections 9.1.2 to 9.1.3. The results from constant wind tests were used to verify that the turbine behaved as expected, as referenced in Section 9.2. A decay test was performed to establish the natural periods, as Section 9.3 explains. Additionally, a brief maximum pitch and nacelle acceleration test was conducted to confirm if the model behaved according to Oh et al., as described in Section 9.4.

A spectral comparison was conducted to identify if the simplified models in SPAROpt captured significant trends when compared to the nonlinear analysis in SIMA, as detailed in Section 9.5. The maximum internal forces were extracted and used to assess the ultimate strength, considering factors such as the yielding of the PC steel, the occurrence of bending cracks, shear cracks, and shell buckling of the concrete, as discussed in Section 9.6.2.

A 1-hour fatigue calculation for irregular waves with turbulent wind conditions was carried out to study the fatigue damage and life expectancy for both the steel tower and concrete hull, as presented in Section 9.7. Finally, an optimization process was performed with the objective of reducing the spar weight while considering a limited number of design variables and extreme environmental loads, (Section 9.8).

9.1 Potential Flow Result

A comparison is presented between the nonlinear flexible models (SPAR 1 and 2) and the linearized frequency domain analysis models (SPAROpt 1 and 2). Before presenting the potential flow results, it is important to note that the Response Amplitude Operator (RAO) is not included due to the simplified modeling discussed in Section 8.6.1 and Section 8.6.2. The incorrect consideration of structural mass and ballast material would lead to inaccurate RAO values. Furthermore, certain results were not considered in SPAROpt, and in those cases, the corresponding graph is not visible in the results, particularly for damping analysis.

9.1.1 Excitation

Surge

The surge excitation is depicted in Figure 9.1. The dashed lines representing the SPAROpt models demonstrate surge excitations that closely resemble the HydroD model's behavior (solid line), with a minor deviation observed for low wave frequencies ($\omega < 0.5$ rad/s). As the frequency increases, the surge excitation becomes more significant for the HydroD model.

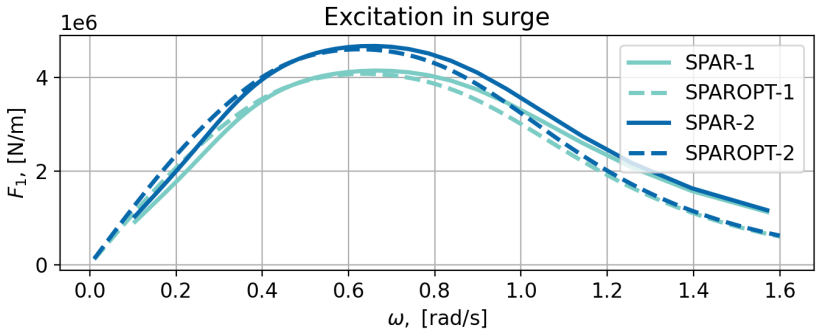

Figure 9.1: Wave excitations in surge

Heave

Regarding heave excitations, as illustrated in Figure 9.2, both SPAR 1 and 2 exhibit similar behavior, although larger excitations are observed in the latter case.

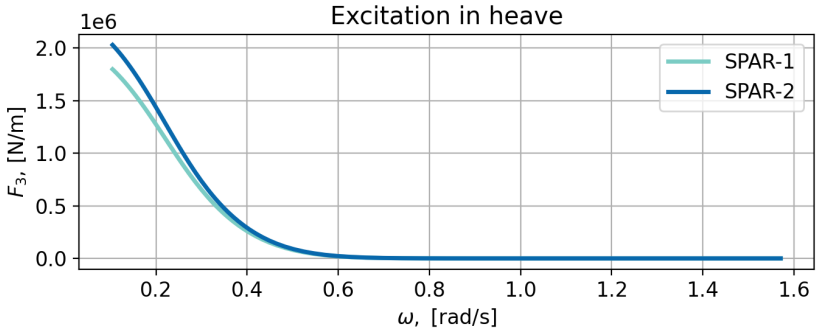

Figure 9.2: Wave excitations in heave

Pitch

The excitation in pitch, depicted in Figure 9.3, reveals that SPAROpt models exhibit slightly larger excitation at lower frequencies. However, for higher frequencies, the results obtained from the SPAROpt models align closely with the results from Wadam.

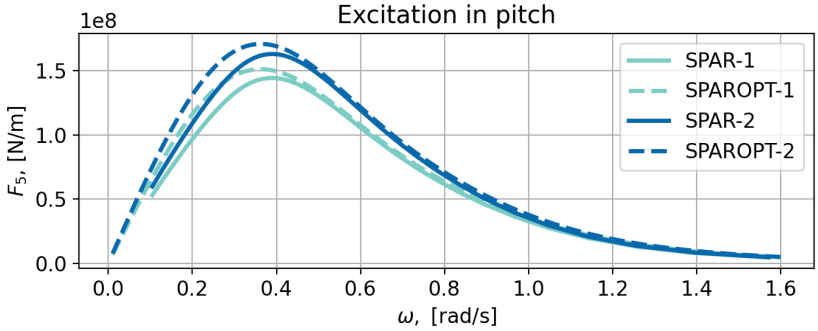

Figure 9.3: Wave excitations in pitch

9.1.2 Added Mass

The added mass coefficients exhibit variations based on the wave load model employed. Notably, the SPAROpt models utilize strip theory-based added mass calculations. Consequently, noticeable discrepancies emerge between the PFT and SPAROpt models at specific frequencies. Hence, this analysis incorporates the results from both the WAMIT simulations employing Flexible Spar and the SPAROpt simulations. It is important to note that the symmetry of the spars in the xz- and yz-plane allows the surge and pitch-added mass coefficients to represent sway and roll, respectively. Therefore, the following analysis focuses solely on the surge, heave, pitch, and coupled surge-pitch added mass coefficients.

Surge

Figure 9.4 illustrates that the added mass in the surge direction closely aligns with the system's total mass, resulting in 24.4 thousand tonnes for SPAR 1 and 27.6 thousand tonnes for SPAR 2. A distinction arises between the SPAROpt and Wamit models, as SPAROpt employs an approximation for the added mass. The discrepancy between SPAROpt and Wamit amounts to 13%, at 0.5 rad/s.

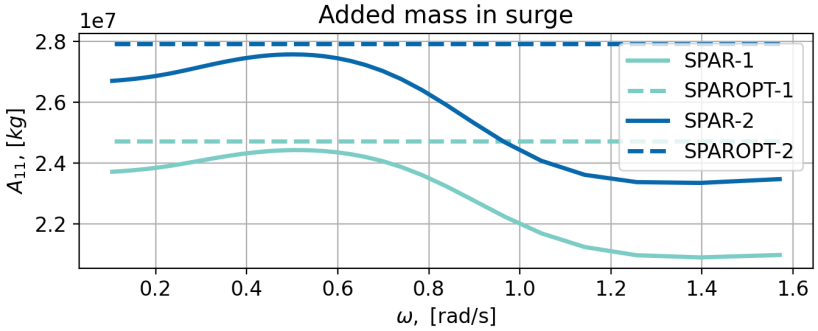

c

Figure 9.4: Added mass in surge for the different simulation models

Heave

The added mass in the heave direction is presented in Figure 9.5. Notably, the SPAROpt code utilizes a simplified formulation by approximating the added mass through the consideration of a sphere, resulting in slightly larger values. As expected, the two models exhibit distinct added mass values, further emphasizing the influence of different geometries.

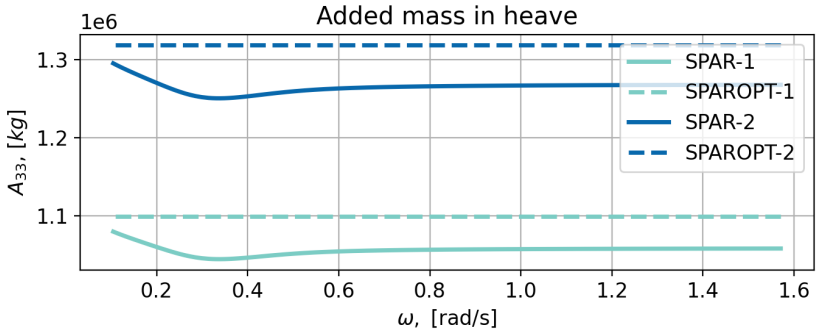

Figure 9.5: Added mass in heave for the different simulation models

Pitch

Figure 9.6 depicts the added mass in the pitch direction. The results consistently demonstrate that the SPAROpt models exhibit larger added mass values compared to the Wamit models.

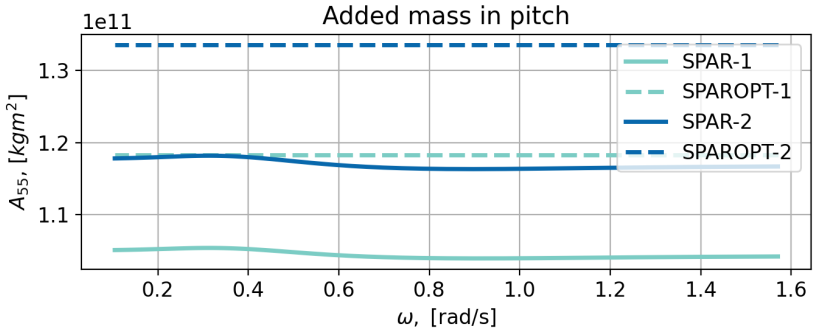

Figure 9.6: Added mass in pitch for the different simulation models

Surge-Pitch

The behavior of the coupled added mass during surge-pitch, as depicted in Figure 9.7, deviates significantly between the SPAROpt and Wamit models. In contrast to the previously discussed added mass results, it is noteworthy that the SPAROpt model exhibits greater values than the WADAM model for surge-pitch, with a difference of 9% at $\omega = 0.4$ rad/s.

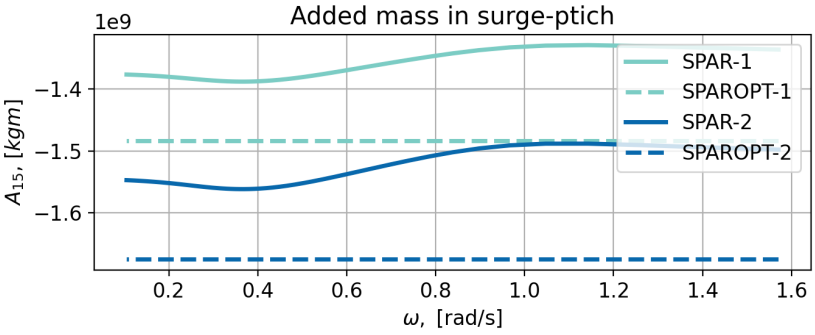

Figure 9.7: Added mass in surge-pitch for the different simulation models

9.1.3 Damping

The damping obtained from Wamit for the two models is presented here. For the same reasoning as for added mass, the same DOFs are presented.

Surge

Figure 9.8 illustrates the damping in surge B_{11}. The results obtained from WADAM indicate that SPAR 1 exhibits lower damping than SPAR 2, particularly in the region of $\omega = 1.0$ rad/s. This finding aligns with expectations since both spars possess similar shapes but differ in diameter. Additionally, wave excitation in surge is more pronounced for SPAR 2 within this frequency range. At the lowest and highest frequencies, the damping values for both models coincide, reflecting similar excitation conditions.

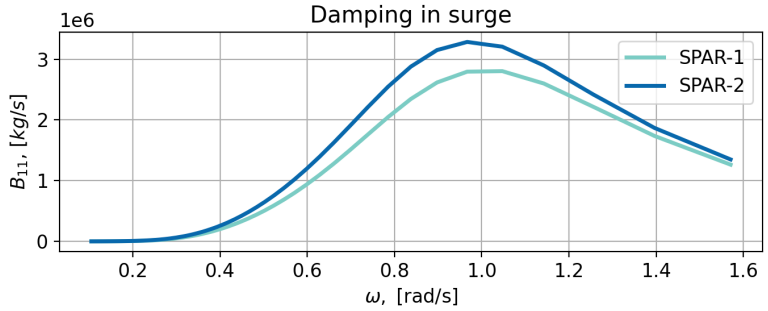

Figure 9.8: Damping in surge for different models

Heave

The damping in heave B_{33} is presented in Figure 9.9. Again, the two models experience similar behavior for the higher frequency. The excitation in heave is larger for SPAR 2 than 1, but this is expected since it has a larger diameter. B_{33} is moving towards zero for higher frequencies since no waves are generated by the spars for such frequencies.

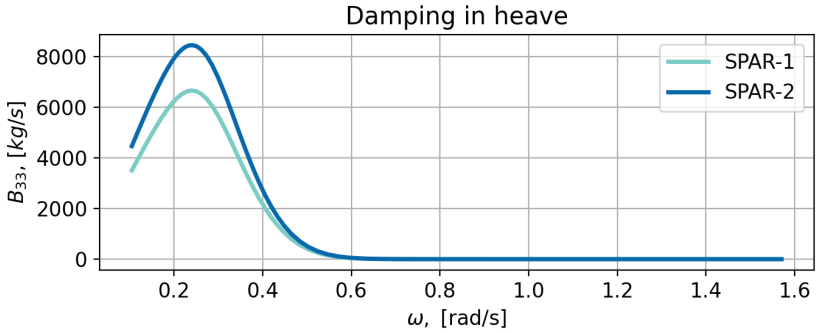

Figure 9.9: Damping in heave for different models

Pitch

Figure 9.10 reveals the same trend for the two spars where the geometry is the leading factor to difference, with a difference of approximately 30%

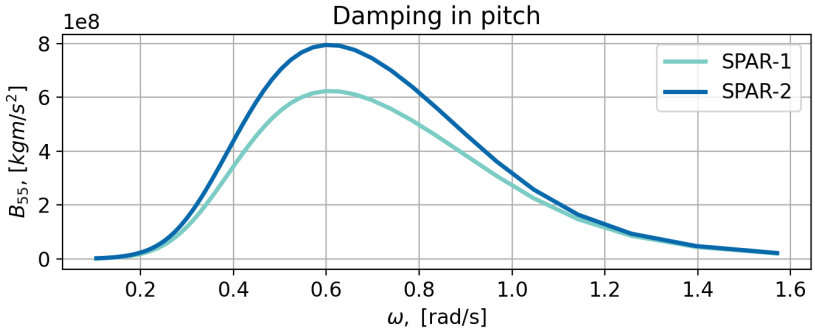

Figure 9.10: Damping in pitch for different models

Surge-Pitch

The surge pitch damping B_{15} is illustrated in Figure 9.11, SPAR 2 has approximately 20% larger damping than SPAR 1 in surge-pitch.

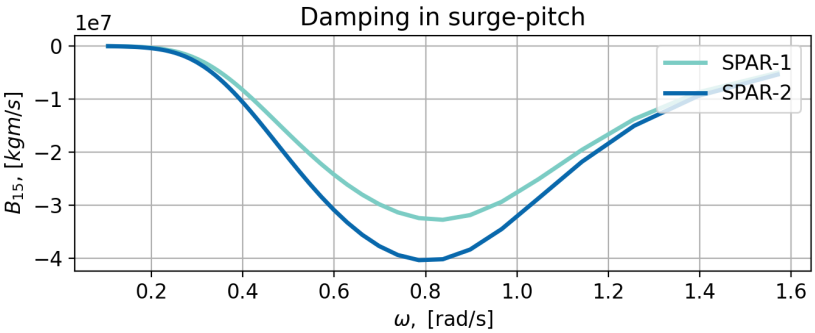

Figure 9.11: Damping in surge-pitch for different models

9.2 Constant Wind Test

Constant uniform wind tests are conducted to evaluate the performance of the FOWT and controller. Wind speeds between 4 m/s and 24 m/s were applied, with an additional step at a rated wind speed of 11.4 m/s. Each wind speed was simulated for 800 s, excluding the first wind speed, which was simulated for an additional 600s. Table 9.1 contains the SIMA settings for the constant wind simulation.

Table 9.1: Simulation parameters for constant wind tests, SIMA.

Simulation length	10000 s
Simulation time step	0.005 s
Wave/body response time step	0.1 s
Turbine condition	Operational
Wind input	Constant
Wave conditions	$H_s = 0.001$ m, $T_p = 20$ s

The uniform constant wind test is distinguished by a small or almost zero change in wind speed throughout the entire diameter of the wind turbine disc. Furthermore, no vertical or lateral speed fluctuation is anticipated, and a constant wind speed is regarded throughout the whole running period. As a result, the goal is to generate a continuous flow with changes in mean wind speed to construct the so-called wind turbine performance curve.

Constant Wind Results

As seen in Figure 9.12a, the rotor is behaving according to the cut-in and rated rotor speeds (C. Bak et al.[2]). The blade pitch is initially non-zero to maximize power output at low wind speeds. It then increases as the wind speed increases to reduce structure vibrations while maintaining the rated power, as seen in Figure 9.12a. In the same figure, the torque increases until it reaches the rated wind speed, where it stabilizes at the rated value. Figure 9.12b illustrates that thrust increases proportionally to the square of wind speed until it reaches the rated wind speed. The blade pitch control is activated at the rated wind speed, resulting in a decrease in thrust. In the same figure, the power increases with the cube of the wind speed, then stabilizes at the rated power.

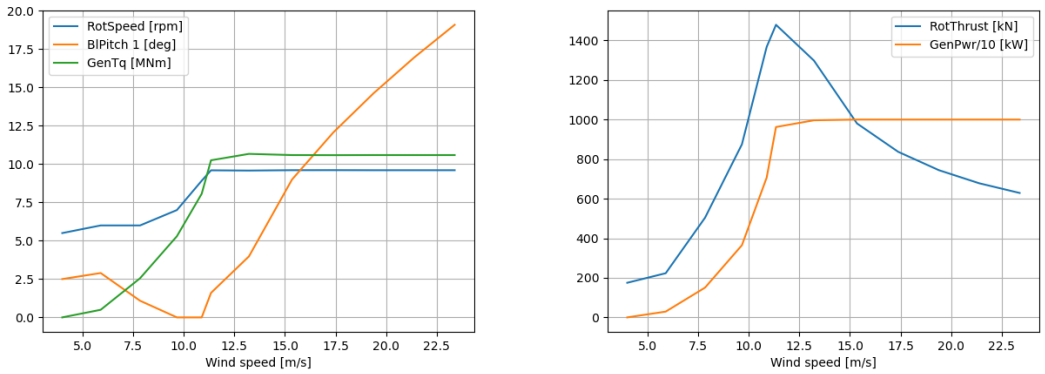

(a) Mean rotor speed, blade pitch, and torque

(b) Rotor thrust and mean generator power

Figure 9.12: 10 MW wind turbine performance curves

9.3 Decay Test

The decay tests were carried out to establish the natural periods for all the spars, in the absence of wind.

9.3.1 Simulation Inputs

The initial movement of the platform was accomplished by applying a ramp force, then a constant force, and finally releasing all of the force being applied. After fifty seconds had passed, the ramp force was activated in order to give the system sufficient time to reach a steady state. The force and moments for each motion are listed in Table 9.2. In the decay tests, the turbine is stopped, and its blades are oriented at a 90-degree angle.

Table 9.2: Forces and moments applied to the FOWT.

Motion	**Force/Moments [kN/kNm]**	**Ramp duration [s]**	**Constant force duration[s]**	**Simulation length [s]**
Surge	1000	100	200	1200
Sway	1000	100	200	1200
Heave	3000	50	100	800
Roll	180000	50	100	800
Pitch	180000	50	100	800
Yaw	17000	50	100	400

In SPAROpt, the environmental condition is set to $H_s = 1$ m, $T_p = 20$ s, and U = 1 m/s, and no force is applied.

9.3.2 Decay Results

Figure 9.13 presents the natural periods for all models, offering valuable insights into their structural behavior. It is important to clarify that the natural periods shown in this figure are specific to the structures examined in this thesis, as no natural periods were available from Oh et al. study. As the spars exhibit symmetry in the xy-plane, the figure highlights the natural periods for surge, heave, pitch, and yaw, considering these dimensions to be of greater significance (sway and roll can be regarded as less important and are equivalent to surge and pitch, respectively).

The natural surge period for each model is consistently higher than the frequency of wave excitation. The value of surge (T_{11}) is associated with added mass, which is determined differently depending on the wave calculation technique. The SPAROpt models exhibit a larger added mass in surge (A_{11}), leading to a longer natural period. However, the difference is small.

The natural period in heave (T_{33}) is identical across all models.

In the case of pitch, the natural period (T_{55}) displays slightly more variability compared to heave. Additionally, it is influenced by both added mass (A_{55}) and hydrostatic stiffness (C_{55}). When calculating C_{55} for the spar in HydroD, the absence of concrete walls or ballast leads to an underestimated value. This issue was rectified in SIMA, and the discrepancy may be attributed to the correction implemented in SIMA. The RIFLEX formulation is utilized in flexible models but exhibits similar behavior. The SPAROpt models exhibit a slightly lower T_{55} compared to the SIMA models. One possible explanation for this is the modification of stiffness in SIMA, which could have contributed to the observed difference. However, it is worth noting that the larger added mass in the SPAROpt models should have resulted in a longer pitch period.

None of the models individually account for yaw stiffness. This resulted in numerical instability, necessitating the setting of a hydrostatic stiffness coefficient in yaw as $C_{66} = 150, \text{MNm}$ for all models for practical purposes. The results show that C_{66} has distinct effects on rigid and flexible

models. The natural periods in yaw for the rigid variants are 14% higher. However, since both models employ the same C_{66}, this may indicate that the mass distribution in the flexible models is different from the rigid spars.

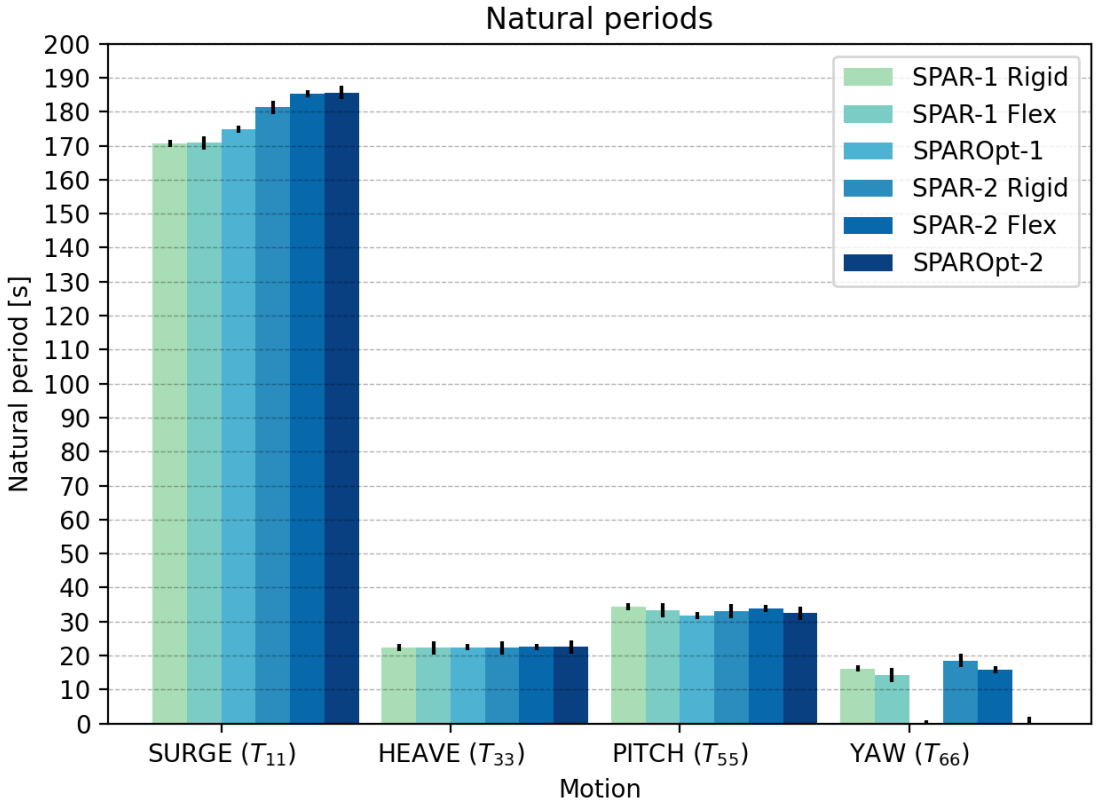

Figure 9.13: Decay test result for all models

9.3.3 Tower Base Fore-aft Bending Natural Period

The natural bending period in pitch can be determined by using the pitch decay test result for the tower base fore-aft bending moment, as shown in Figure 9.14. This result can be converted to natural angular frequency and compared to the frequencies of the 1P and 3P rotors. These frequencies are calculated by determining the minimum and maximum rotor speeds that the wind turbine will experience during constant wind tests.

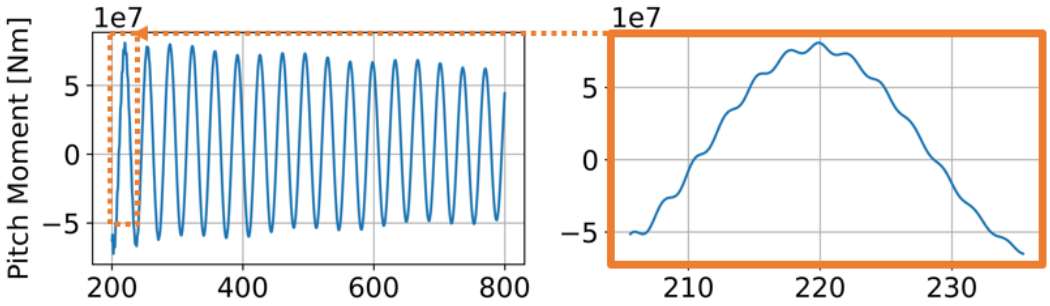

Figure 9.14: For-aft pitch bending moment at tower base.

In the first bending mode analysis, it is observed from the recorded natural periods for all spars (as depicted in Figure 9.15) that the natural frequencies fall within the 3P region. This renders the tower susceptible to blade rotation resonance, which can gradually weaken both the tower and the spar. However, such behavior was anticipated since the turbine under consideration is intended for land-based use. To mitigate this issue, a recommended approach involves modifying the thickness of the tower to enhance its stiffness, thereby shifting it outside the 3P region. This adjustment aims to reduce the occurrence of additional stress. Comparison among the rigid, flexible, and SPAROpt models reveals consistent predictions for the period, indicating a coherent alignment of the models in both the time and frequency domains. To maintain consistency with the study conducted by Oh et al., the wind turbine is being retained in its current state.

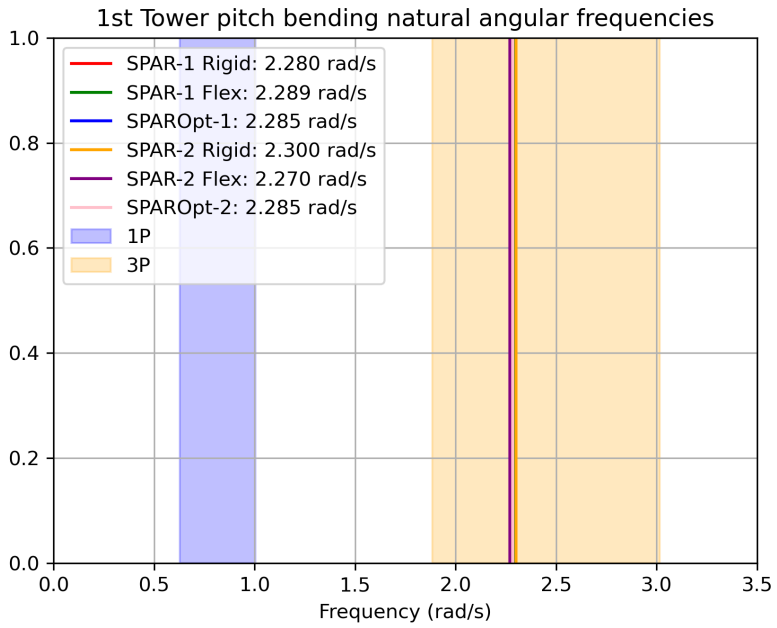

Figure 9.15: Moment of forward-aft bending at tower base compared to 1P and 3P

9.3.4 Structures Normalized Mode Shape and Curvature

The normalized 1st mode shape obtained from SPAROpt for both spars is depicted in Figure 9.16a. The mode shape clearly illustrates the influence of increased stiffness in the slightly larger SPAR 2. A similar trend is observed in Figure 9.16, where the curvature of the hull and tower is presented. It is evident that the smaller SPAR 1 experiences a slightly larger curvature due to its smaller cross-section. Notably, the steel tower between the two models exhibits the same curvature, as expected due to their identical geometry. In addition, it also shows that the concrete hull has very little curvature.

The transition from the concrete hull to the steel tower reveals a significant discontinuity, primarily attributed to the considerable reduction in cross-sectional area. This discontinuity poses a notable challenge in achieving favorable outcomes. Additionally, the presence of such a discontinuity at the location of curvature further complicates the retrieval of satisfactory results. Notably, the region demonstrating the highest curvature aligns with the location experiencing the most significant tension.

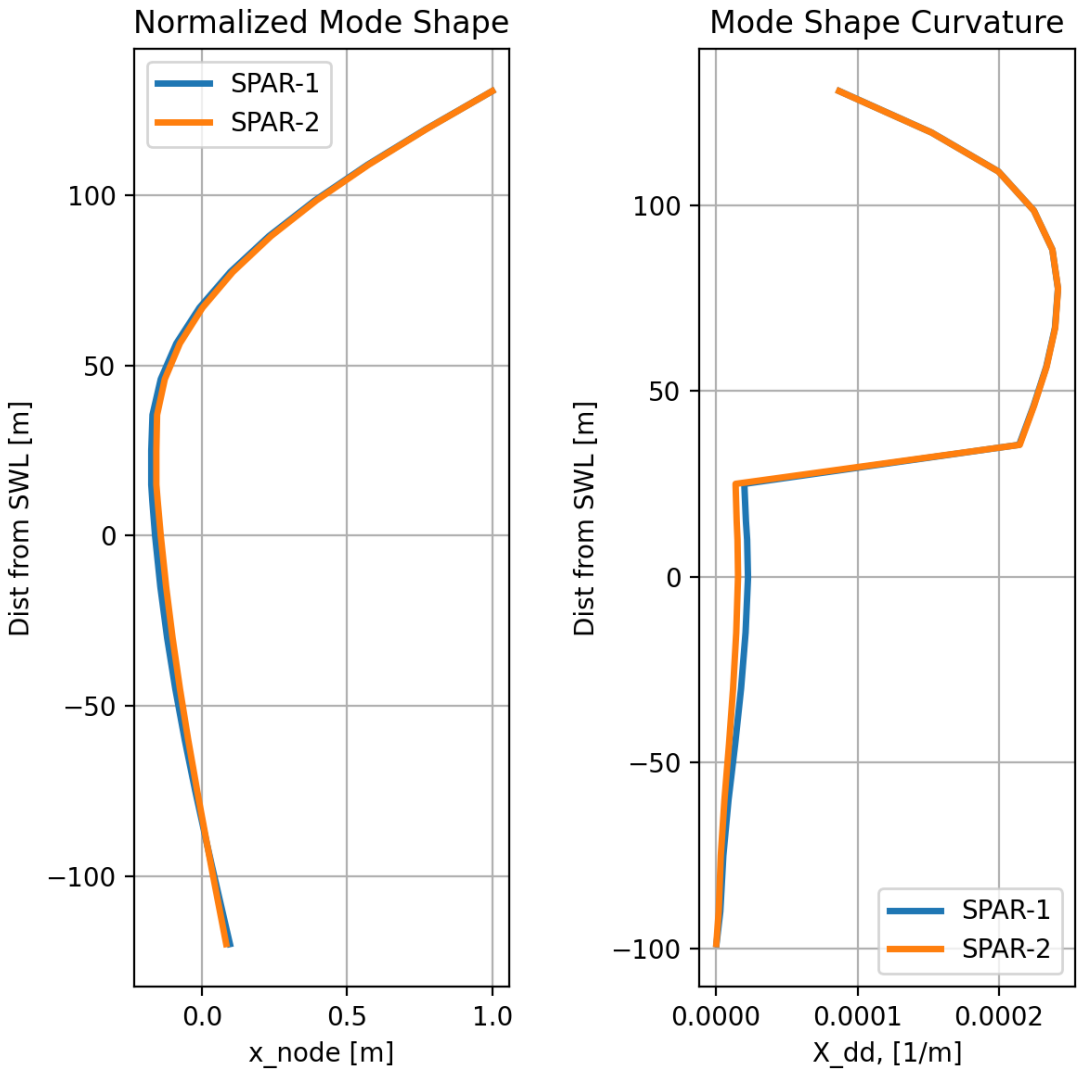

(a) Normalized mode shape tower and hull

(b) Structural curvature tower and hull

Figure 9.16: Mode shape and curvature of structure

9.4 Reference Model Test

Prior to proceeding with the model, a performance study was undertaken to authenticate its efficacy. The validation test was conducted in accordance with the experiment carried out by OH et al., with the objective of determining the maximum pitch angle and its corresponding maximum nacelle acceleration under combined wind and wave conditions, with a singular constant wave period as outlined in Table 9.3. The wave simulations were generated using a 3-parameter JONSWAP spectrum within the SIMA software, while the wind turbine was configured to operate under typical conditions.

Table 9.3: Environmental conditions for spectral analysis

Condition number	$\mathbf{V_{hub}}$**[m/s]**	**Turbulence Intensity [%]**	$\mathbf{T_p}$**[s]**	$\mathbf{H_s}$**[m]**
1				11.1
2	11.1	14.90	11.71	12.7
3				14.3
4				11.1
5	15.00	13.48	11.71	12.7
6				14.3

A maximum pitch at CoG and maximum nacelle acceleration were conducted, leading to the results presented in Table 9.4. It is evident that there exists a considerable discrepancy in the maximum pitch values. However, it is crucial to acknowledge that Oh et al. utilized different analysis methods compared to those employed in this thesis. Furthermore, modeling errors or simplifications may have been introduced that could have had a more significant impact than initially anticipated. It is important to acknowledge that relying on maximum values as a basis for results, as done in the reference study conducted by Oh et al., introduces a sensitive statistic. This statistic exhibits greater variability compared to measures such as standard deviation. The trend observed in nacelle acceleration demonstrates similarities.

Table 9.4: Refrence model validation result (* Results form Oh.et al [55])

	SPAR 1	**Spar 1***	**SPAR 2**	**Spar 2***
Max.Pitch @ COG	8.90	10.25	8.17	10.25
Max.Acc @ nacelle	4.45	4.40	4.38	4.30

As this result represents the only available validation data, it was concluded that the design should proceed without modifications.

9.5 Spectral Comparison Between SIMA and SPAROpt

An important aspect of this thesis is to determine whether the simplified SPAROpt analysis can effectively capture significant trends in the response. A comprehensive comparison can be made by utilizing the Power Spectral Density (PSD) obtained from both SIMA and SPAROpt. The PSD provides valuable insights into the power distribution across various frequencies, playing a crucial role in understanding the dynamic response of structures under specific loading conditions. The strength and limitations of each approach are evaluated by comparing the results from time-domain and frequency-domain analyses, enabling a comprehensive assessment of the structural behavior. Furthermore, analyzing the spectra is one of the only ways to effectively compare time-domain and frequency-domain results, highlighting each method's unique advantages and drawbacks.

To conduct the study, three environmental conditions with a duration of one hour, representing below, at, and overrated wind speeds, are generated and presented in Table 9.5. These conditions are designed to isolate distinct structural behaviors and effects typically observed under such circumstances. A side-by-side comparison is presented between the two considered structures (SPAR 1 and SPAR 2) for both SPAROpt and SIMA.

Table 9.5: Environmental conditions for spectral analysis

Condition number	H_s **[m]**	T_p **[s]**	V_{hub} **[m/s]**	**Turbulence Intensity [%]**
LC1	3	8	6	23.6
LC2	4	9	10	18.3
LC3	6	12	18	16.1

Before conducting a combined wind and wave test, separate tests were conducted to isolate the responses of each environmental factor and to observe if the SPAROpt projected the same result. The complete results from the three analyses can be found in Appendix A, but a short summary of the independent wave and wind tests will be presented here.

Wave Only

The wave verification shows agreement in the shape of the responses from SPAROpt, though SPAROpt seems to underestimate the wave-frequency peak for surge, pitch, tower bending moment, and hull bending moment. In addition, SPAROpt seems to underestimate the resonant peaks for surge and pitch, whereas SIMA, shows a clear resonant behavior. This may be due to the fact of the simplified modeling of the mooring and that SPAROpt does not consider the drift force. Although the magnitudes differ, the standard deviation's similarity suggests that the relative strengths and variances within the frequency components are preserved.

Wind Only

Both SIMA and SPAROpt exhibit peak resonant responses for natural frequency for wind-only conditions. However, there are discrepancies observed in the predictions of the magnitude of surge responses using SPAROpt, and it may indicate the simplified aerodynamic model used in SPAROpt does not capture the same trends as SIMA, and some effects due to the simplified mooring system may also increase the difference observed. SPAROpt underestimates the surge response and overestimates the pitch response, which may indicate a larger aerodynamic damping in pitch for the linearized model. For the tower and hull bending, the same overestimation is seen for SPAROpt.

9.5.1 Surge

Figure 9.17 shows the combined wave and wind PSD for surge motion, for the two spars, for both SIMA and SPAROpt. The spectral density function S(ω) is plotted against the angular frequency in Figure 9.17. As depicted, there is variation between the two analyses, showing the same underestimation for all conditions. Condition 3 indicates a significantly larger surge resonance peak in SIMA, and a resonance peak at pitch natural frequency; this may be because the fairleads are not placed in the COG of the system, increasing the coupling between the surge and pitch motion for larger environmental conditions.

Certain limitations were also noted in accurately capturing low-frequency surge motion, which can be attributed to the inherent difficulty in modeling aerodynamics accurately and the possibility of instability in the control system at the surge's natural frequency. Additionally, the largest energy concentration was located to the left of Figure 9.17 for frequencies $\omega = 0 - 0.06$ rad/s, which are wind frequencies. This indicates that the primary excitation source in surge is wind excitation. LC2 is the condition closest to rated wind speed and is observed and expected to have the most considerable excitation. For all conditions and structures, the highest peak was located near the natural period in surge ($\omega = 0.036$ rad/s and $\omega = 0.034$ rad/s). LC3 also displayed an energy accumulation from $\omega = 0.12 - 0.20$ rad/s, which are also from wind, especially for higher wind speeds. Finally, there were also small energy accumulations from $\omega = 0.3 - 0.7$ rad/s due to wave frequencies (not seen in Figure 9.17).

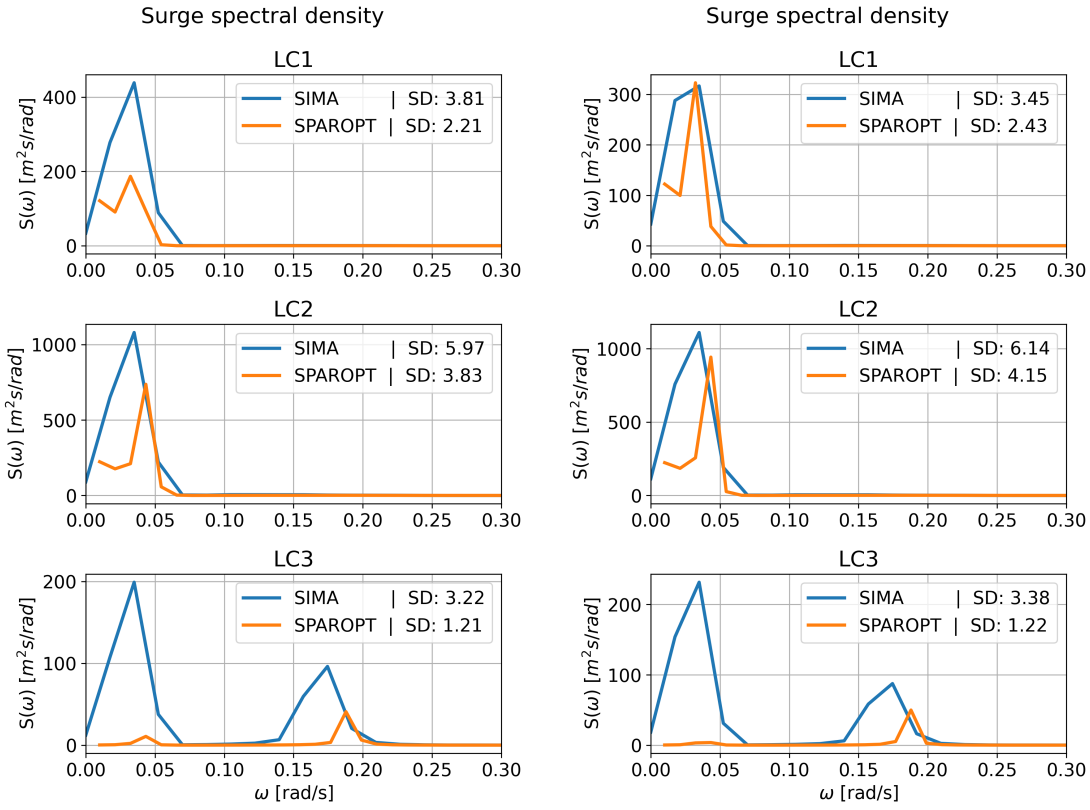

(a) Spar 1

(b) Spar 2

Figure 9.17: Analysis of Spectral Characteristics in Surge for Spar 1-2 for all LC

9.5.2 Pitch

The pitch spectral analysis was conducted in the same manner as in surge, and only the combined wind and wave spectra are shown in Figure 9.18. It is observed greater peaks for low frequencies ($\omega = 0 - 0.2$ rad/s) are observed, indicating larger energy accumulation from the wind. LC3, which has the largest wind velocity, exhibited the most excitation in this region, and with a maximum peak at $\omega = 0.17, 0.186$ rad/s for SIMA and SPAROpt, respectively, which are close to the corresponding structure's natural period in pitch.

Similar to surge, the pitch spectrum has low energy in the wave excitation region, within the range of ($\omega = 0.3 - 0.8$ rad/s). Once again, LC3 is the most significant in this region. Overall, LC1-2 indicates that SIMA and SPAROpt exhibit reasonable similarities but with a larger deviation for higher wind that may suffer from the same limitations discussed in surge.

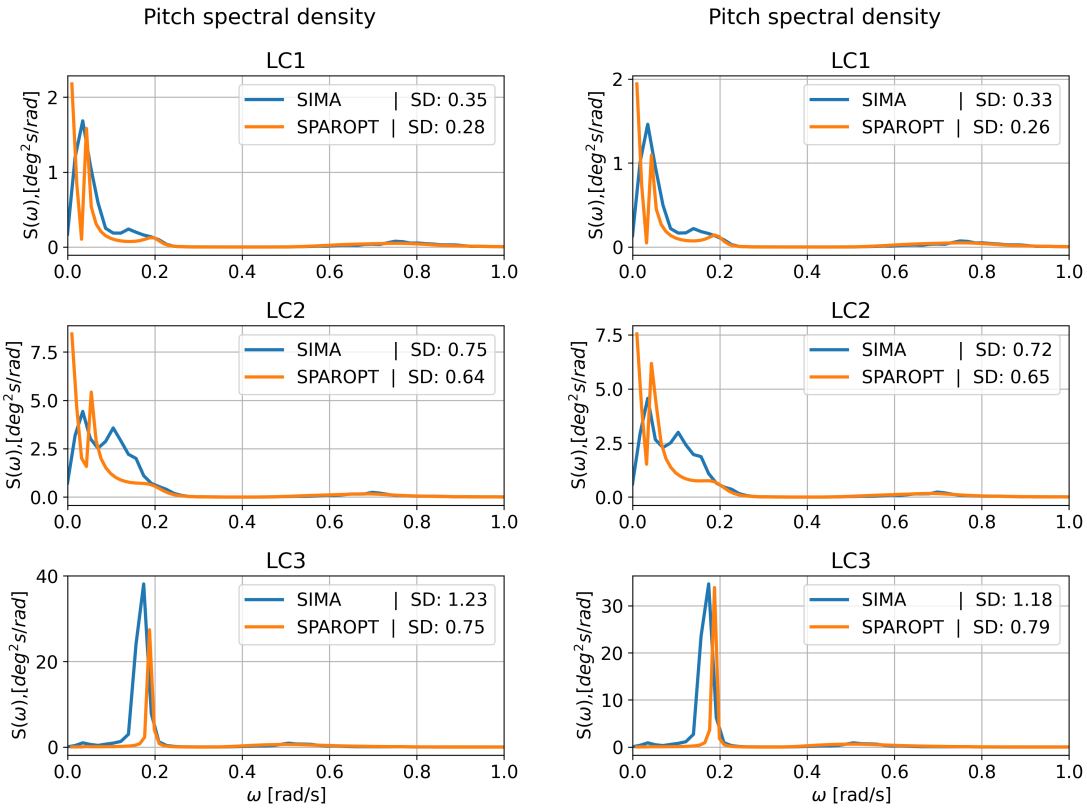

(a) Spar 1

(b) Spar 2

Figure 9.18: Analysis of Spectral Characteristics in Pitch for Spar 1-2 for all LC

9.5.3 Tower

A spectral analysis is conducted for the tower bending moment at the base, middle, and top to investigate the tower excitation. Due to similarities in base and middle, the middle part is illustrated in Figure 9.19. Wind and waves excited the middle of the tower, and bending moments are clearly related to pitch excitation. The bending moment spectrum essentially replicates the pitch spectrum in the wind and wave frequency regions, resulting in similar behavior in bending moment for the different load cases for both SIMA and SPAROpt.

For larger frequencies outside the range of wind and wave excitation, the bending moment experiences concentrations of energy for all models. They are smaller than values for wind and waves but not insignificant. These concentrations represent the tower fore-aft bending natural periods estimated in the decay test earlier (Section 9.3.3). It is observed that the first bending natural periods for LC1-2 are in the blade passing region (3P) except for LC3. However, it is observed that SIMA and SPAROpt have excitation in different parts of the spectrum. This is because the blades in SIMA are not modeled as rigid and have some elastic properties, while for SPAROpt, the blades are modeled as rigid, so some deviations in this area are expected. But the structures should not experience resonance for both models due to the rotational frequency (1P).

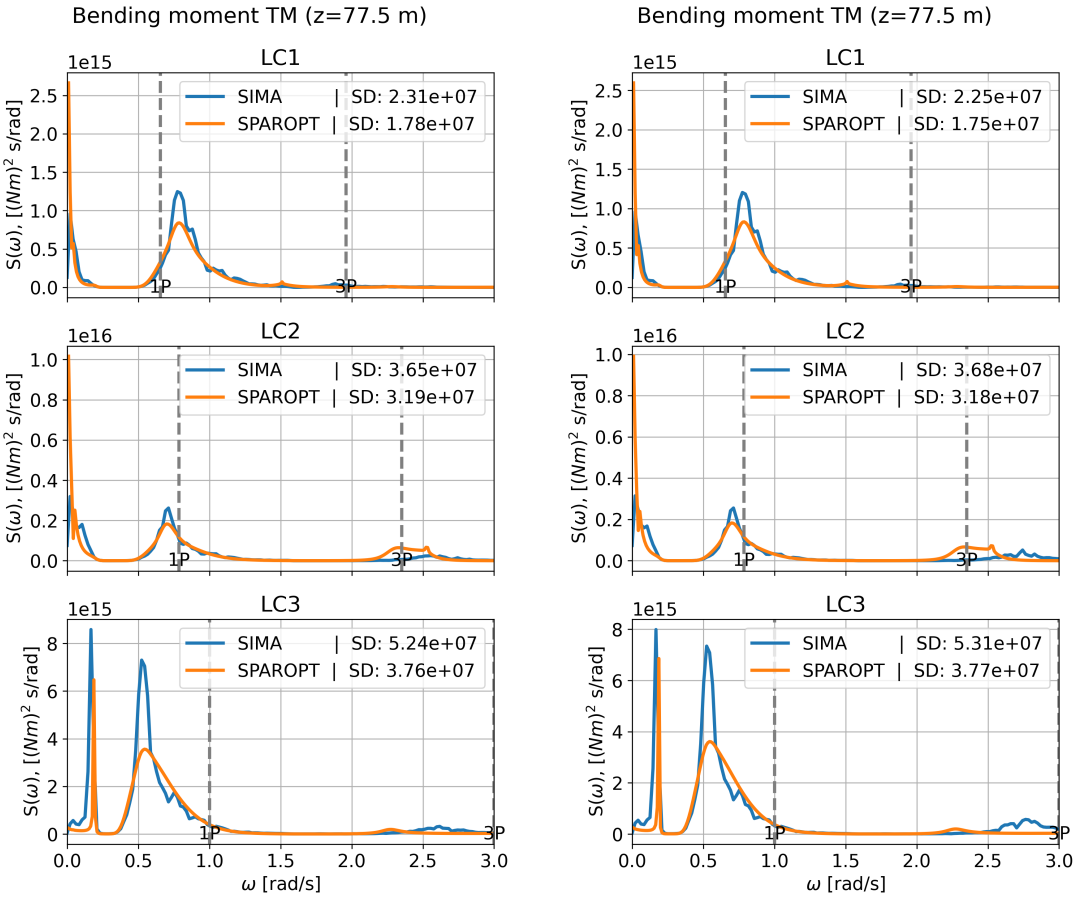

(a) Spar 1

(b) Spar 2

Figure 9.19: Analysis of Spectral Characteristics in Tower Bending for Spar 1-2 for all LC

9.5.4 Spar Hull

Spectral analysis was carried out at several sites, including the transition (z = 8 m), fairleads (z = -22 m), and the top ballast (z = -98 m) areas, to examine the excitation of the concrete hull. Mainly, it was discovered that the connection between the concrete and tower (z = 25 m) and the top of the ballast were especially sensitive to curvature and positioning, leading to deviations in the excitation of bending moments. This may be a result of the mismatch of splines fitted at the transition from spar to the tower in SPAROpt. Unsurprisingly, the highly different mode forms in the connection point and the resulting aberrant consequences may be driven by variances in material behavior and properties between concrete and steel. To resolve this disparity, additional research is required, especially regarding the modeling in SPAROpt.

Due to similarities between the transition region and the mooring, the transition area is shown in Figure 9.19. Pitch excitation were closely connected to the bending moments in the transition region, which were primarily caused by wind and waves. Pitch behavior for various load scenarios in SIMA and SPAROpt, as seen in the tower, was comparable because the bending moment spectrum in the wind and wave frequency areas resembled the pitch spectrum. The hull illustrates similar patterns to the tower at higher frequencies outside the range of wind and wave stimulation, projecting the fore-aft bending natural period. However, it was shown that SPAROpt showed agreement in terms of the size and shape of the response spectra when compared to SIMA, despite tending to overestimate the excitation at high wind speeds.

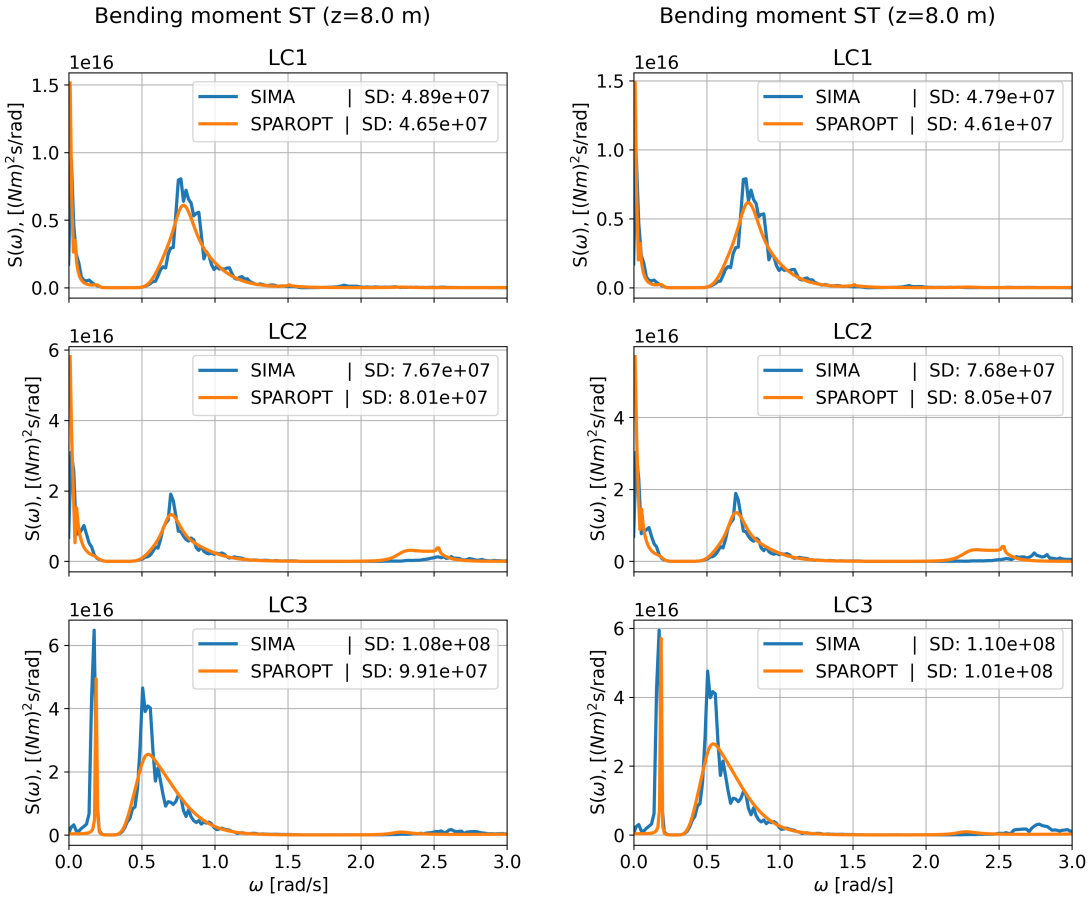

(a) Spar 1

(b) Spar 2

Figure 9.20: Analysis of Spectral Characteristics in Spar Bending for Spar 1-2 for all LC

9.6 Structural Design

To analyze the internal forces acting along the total length of the two flexible spars, the same set of six environmental conditions listed in Table 9.3 was utilized. Each simulation had a duration of one hour. To process the data obtained from the dynamic analysis, a post-processing tool was developed. This tool allowed for the extraction of the maximum and minimum values of the internal forces for each section along the spars and tower across all six load cases, providing a comprehensive overview of the forces experienced during the entire one-hour duration.

9.6.1 Internal Forces

Figure 9.21 illustrates the observation of the most significant shear force at the ballast COG. This abrupt increase in force can be attributed to the ballast being modeled as a point load rather than an evenly distributed load. The effect of the ballast on the shear force is slightly decreasing to around z=-75 m before it enters an area where it slightly changes. Additionally, an indentation in the shear force is evident at the mooring position before it rises along the water line, before decreasing in the transitional area where the concrete spar and steel tower meet. Finally, a linear reduction is seen towards the tower top for the tower.

Between the two spars, there are little differences between the internal loads, but it's seen that spar two experiences a larger negative shear stress and less positive shear stress. Moving over to the tower, it is observed that the negative shear force is larger for SPAR 1 and is the same for the positive shear force. However, when comparing to Oh et al., the same trend and patterns are observed.

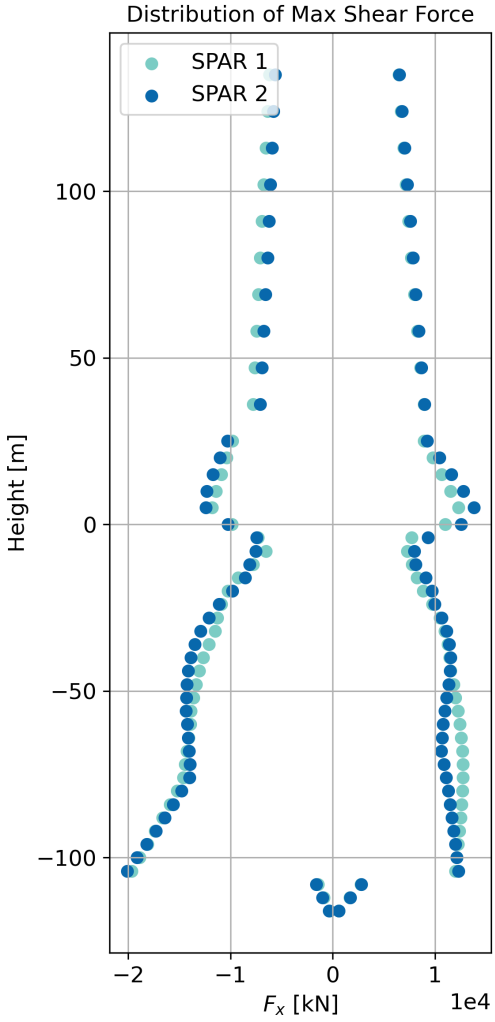

Figure 9.21: Distribution of the max- and minimum values of shear force for SPAR 1 and 2

The bending moment pattern observed for all maximum and minimum values is coherent with the results found by Oh et al. The maximum moment occurs at approximately at height z=-8 m for both structures. It exhibits a steeper decline in moment values below zero in the submerged part compared to the tower stretch. It is worth noting that the expected behavior at the tower and bottom parts descends to zero, indicating the expected behavior of the structure.

The maximum moment values for SPAR 1 and 2 are 1.18e+06 kNm and 1.23e+06 kNm, respectively, leading to a 4% difference between the two structures. However, a more significant deviation is observed for the compressive moment, corresponding to 10e5 kNm and 9.1e5 kNm, resulting in a 10% deviation. This can be explained by the fact that SPAR 2, with its greater cross-sectional area, experiences less compressive moment than the smaller one due to its larger radius of curvature. The resistance of a cylindrical shell to compressive loads is proportional to its cross-sectional area and the square of its radius of curvature, which means that a larger radius of curvature makes the body less susceptible to collapse under compressive loads. This behavior is mainly attributed to the geometry of the structures, and the same trend is observed on the compressive side of the tower at z = 36 m.

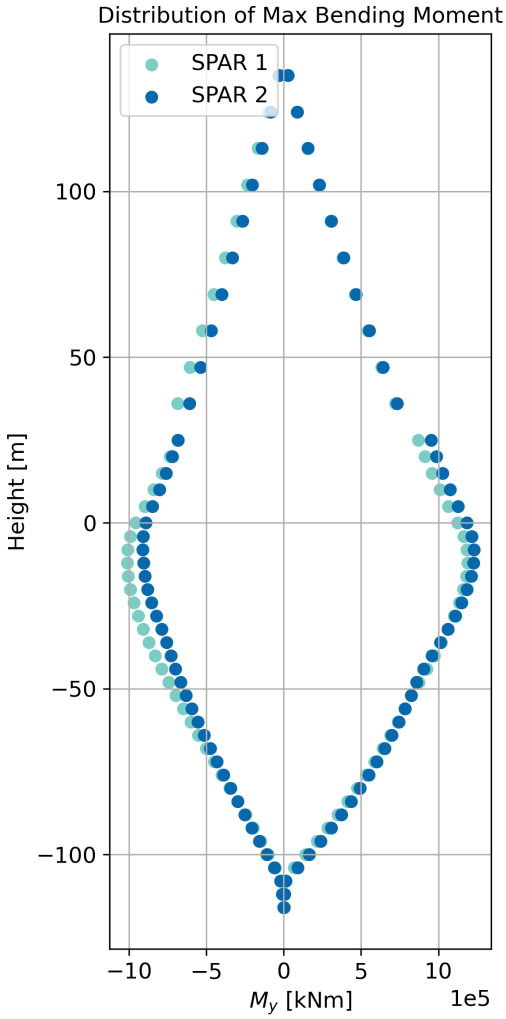

Figure 9.22: Distribution of the max- and minimum values of bending moment for SPAR 1 and 2

Figure 9.23a displays a noticeable deviation in the axial stress profile at the $COG_{ballast}$ location (z = -108 m). The axial stress initially increases towards the mooring position and then decreases towards the turbine tower. At the base of the tower, the axial stress experiences an increase and curves towards the top of the tower. This trend indicates that the bending moment significantly influences the axial stress, as the shape of the axial stress curve resembles that of the moment curve shown in Figure 9.22.

Moreover, it is evident that spar 1 exhibits higher axial stress within the hull compared to SPAR 2. This discrepancy can primarily be attributed to variations in thickness. SPAR 1 has the smallest thickness, amplifying the pressure effect on the cylinder and reducing the distribution area and moment of inertia, thereby leading to higher axial stress.

Regarding the shear stress profile depicted in Figure 9.23b, it follows a similar pattern to the shear force distribution, with the highest shear stress occurring at the minimum shear force values. Similar to the axial stress, there is a consistent indentation at the mooring point, followed by an increase at the SWL and the splash zone. The disparity in shear stress between the two spars can also be attributed to geometric differences. SPAR 1 has a smaller cross-sectional area and moment of inertia, resulting in less resistance to shear stress.

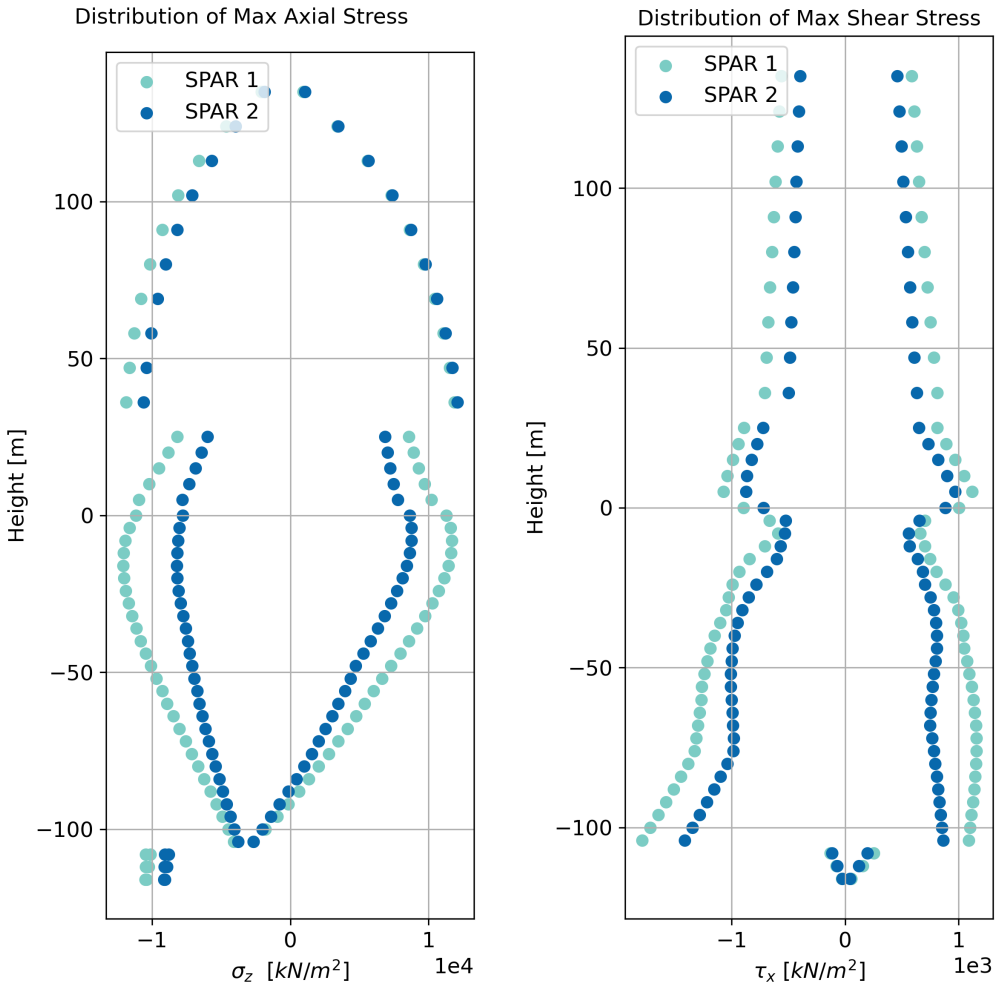

(a) Axial stress

(b) Shear stress

Figure 9.23: Distribution of the max- and minimum values along SPAR 1 and 2 for DLC1.6

9.6.2 Concrete Capacity

PC Steel Yielding

The ratio between necessary pretension and yielding strength of the rebar indicates the stress capacity of the prestressed concrete steel compared to its maximum limit. The yielding strength of the rebar is utilized instead of the tension wire strength to ensure that the rebar steel does not exceed its yield point in the structure. The resulting curve depicted in Figure 9.24 illustrates the outcome of subtracting the moment values from Figure 9.22 from the axial stress values, as shown in Figure 9.23a. An analysis of the results revealed negative pretension values at depths below -80 m to -120 m. For these sections, the pretension was set to zero to better understand the stress requirements for each cross-section. The negative values occurred because the axial stresses surpassed the tensile stresses caused by the moment, resulting in a naturally compressed set of sections. This phenomenon is due to the decrease in moment forces along the length of the structure and the substantial inertia and weight of the substructure, which justify this behavior.

For SPAR 1 and 2, the ratio consistently remains below the failure threshold across the entire height of the structure. Comparing the two methods used, SPAROpt tends to overestimate the ratio, indicating a greater need for prestress deeper into the structure. This can be attributed to the overestimation observed in the spectral compression. The peak above z=-20 m may be a consequence of the mooring connection, where additional forces are introduced into the system. These forces lead to localized increases in tension, but they remain below the yielding strength of the PC steel. Such behavior is expected since the mooring connection point represents a critical area with heightened stress concentrations. The total number of required pretension wires amounts to approximately 1650, which aligns well with the findings obtained by Oh et al.

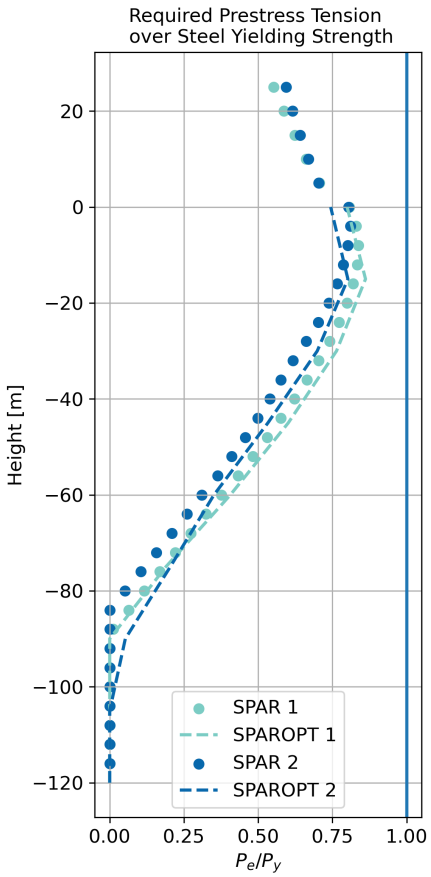

Figure 9.24: The ratio between the required prestress tension and the yielding strength of steel.

Concrete Bending Cracks

Figure 9 presents the ratios of the axial stress in concrete to the allowable long-term and short-term compressive stresses. The graph reveals that both SPAR 1 and 2 maintain short-term axial stresses within the permissible limits, as shown in Figure 9.25a. Compressive stress is mainly due to the large bending stress in the region around z = -20 m for the short-term.

When considering the long-term axial stress, it is important to note that SPAR 1 and 2 consistently maintain values below the allowable stress threshold for all heights. This indicates that the concrete components of the structure operate safely and reliably over an extended period. The longer axial stress utilization at the bottom part could be attributed to the increase in the axial stress due to ballast materials.

The most significant difference between SPAROpt and SIMA is located in the ballast region, where SPAROpt predicts a more smoothed descent. Since SIMA uses a point load compared to the SPAROpt, which uses a distributed load, the SPAROpt portrays a more realistic distribution of ballast mass. The difference is therefore believed to be caused by modeling differences mainly.

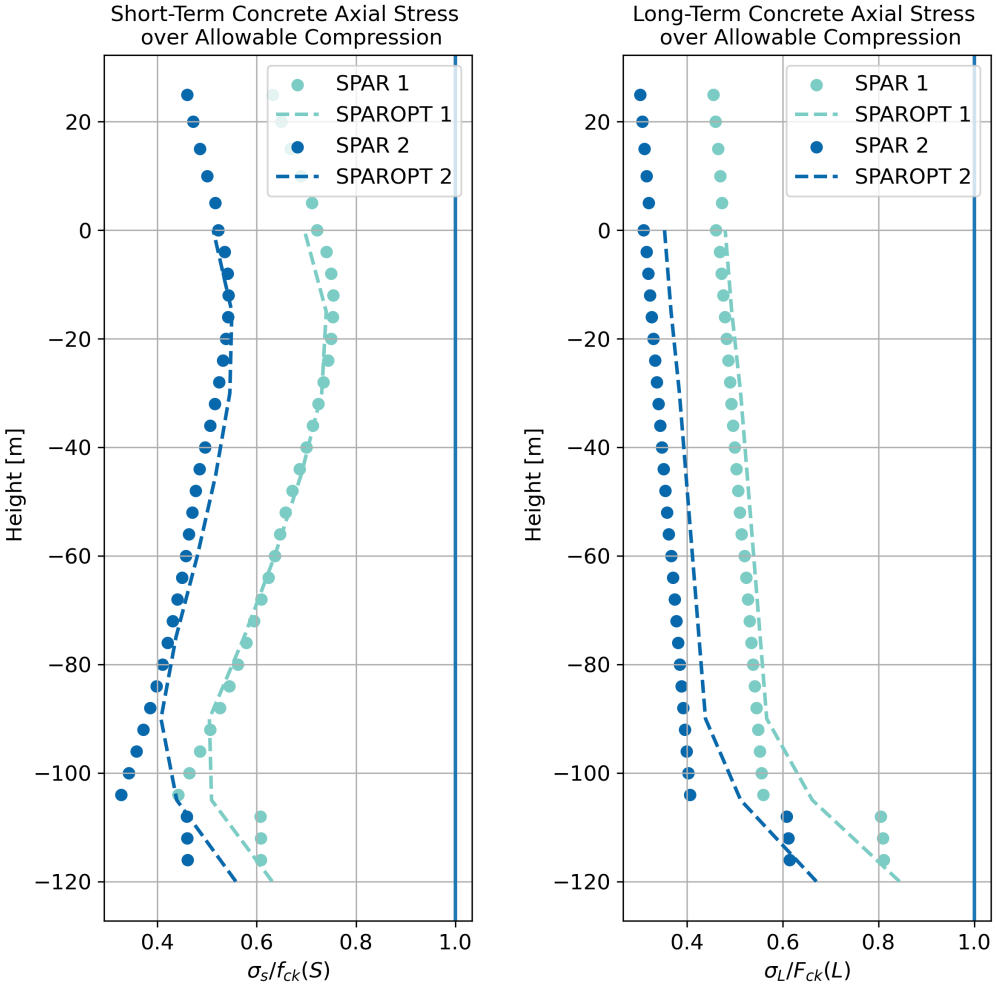

(a) Short-term

(b) Long-term

Figure 9.25: Short-and long-term ratios of concrete axial stress to allowable compressive stress

Concrete shear cracks

Figure 9.26 depicts the stress ratio σ_1 over the concrete tensile strength. The graph demonstrates that σ_1 values remain below the concrete tensile strength for SPAR 1 and 2. When comparing the two methods, there is a noticeable shift close to the surface. The SPAROpt method predicts a greater compressive ratio, which can be attributed to the overestimation of pretension in that specific area, resulting in a higher degree of compression in the cross-section. This deviation is also observed along the length of the structure, aligning with the increased pretension requirements in the same region. Overall, it can be observed that the structure is predominantly in a compressive state, which is expected due to the significant pretension force. However, a slight positive stress is observed towards the SWL for SIMA, which gradually decreases towards the tower. This may be caused by the bending moment in that particular area.

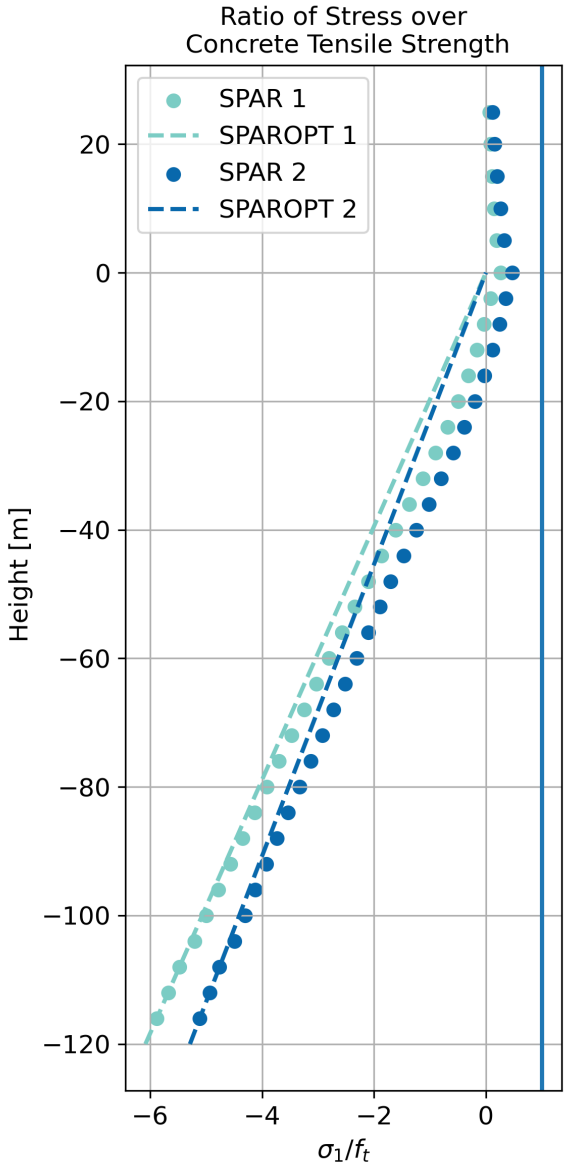

Figure 9.26: The ratio between the first principal stress σ_1 and the tensile strength of concrete.

Shell Buckling

Figure 9.27 depicts the concrete buckling capacity resulting from hydrostatic pressure. Since this capacity represents a static load, both SIMA and SPAROpt methods show good agreement. The deviation observed on the water surface is a result of calculations using water density above zero, and the negative capacity should be interpreted as null values. As anticipated, the capacity at the bottom of the structure is slightly over 75% for SPAR 1 and 50% for SPAR 2. A desired capacity between 80% and 90% is sought to ensure the structure is not excessively oversized. Therefore, it is recommended to reduce the thickness of SPAR 2 to optimize material costs.

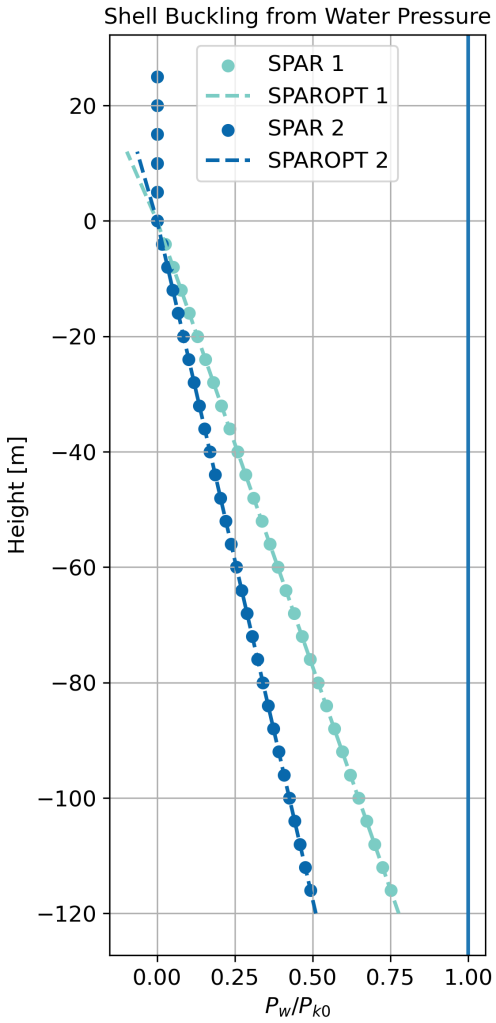

Figure 9.27: Buckling due to water pressure

Figure 9.28a shows the occurrence of shell buckling due to axial stress. As expected, the axial stress increases with depth, and additional axial stress is present at the bottom of the ballast. However, the risk of buckling due to axial stress is considered minimal. A small shift is observed at the SWL and up to the transition area from concrete to spar. This region will experience a higher axial force due to the wind turbine tower and ballast.

Figure 9.28b illustrates the buckling caused by shear stress. The capacity for shear stress is noted to be very high along the structure. However, it appears that SPAROpt underestimates the shear stress. Whether this is, a persistent issue in the analysis model or a unique problem with the reference design is uncertain. However, the risk of shell buckling due to shear stress is considered minimal.

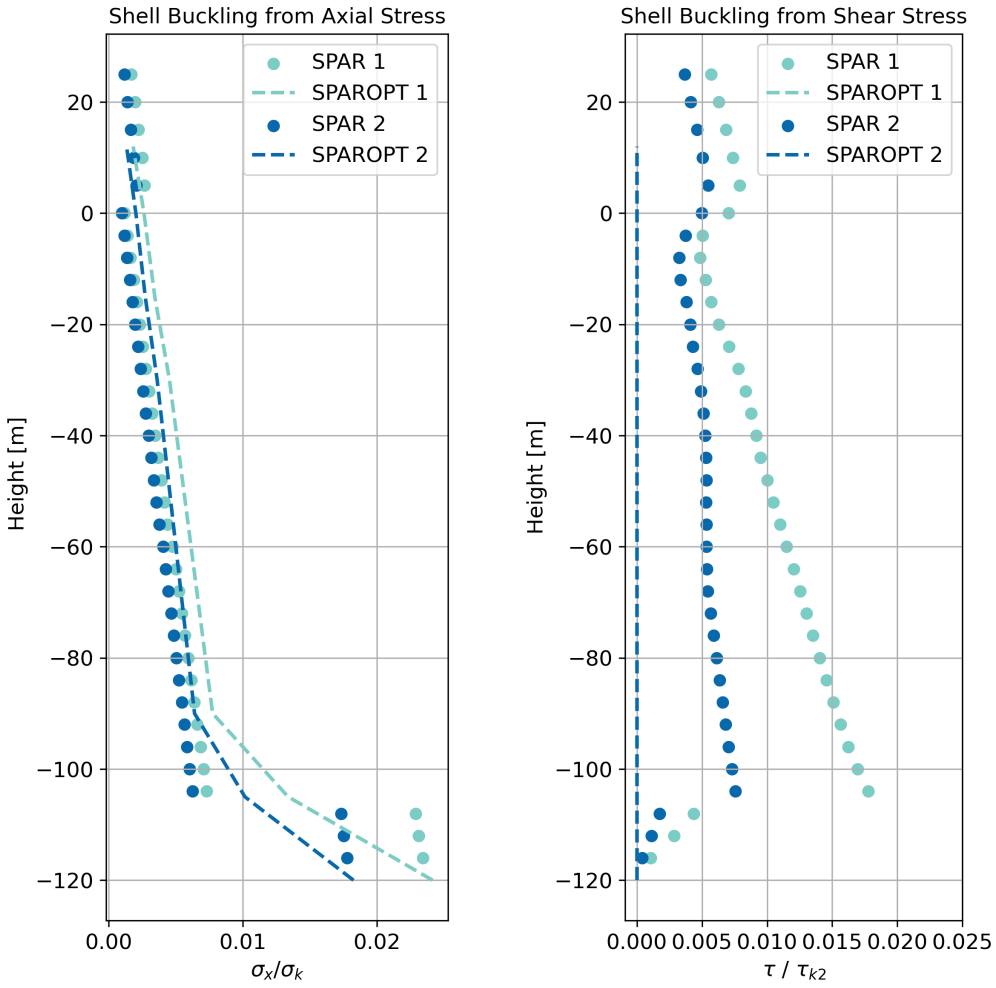

(a) Shell buckling due to axial stress

(b) Shell buckling due to shear stress

Figure 9.28: Findings for stress-induced shell buckling due to axial (a) and shear (b) stresses.

9.7 Fatigue

Fatigue is widely recognized as a critical factor in the design of wind turbines. Therefore, a fatigue analysis is conducted to evaluate the tower and hull's ability to withstand the loads exerted by environmental conditions and operational activities throughout its anticipated lifespan. Time-domain Rainflow-counting method is employed for the fatigue analysis. Stresses and bending moments experienced by the tower and hull under various environmental conditions are employed for the fatigue calculations. In this fatigue analysis, the same environmental stresses described by Oh et al.,(Table 9.3) are used.

9.7.1 Calculation Parameters

Each fatigue condition in the study is simulated with a unique seed value. Consequently, the analysis is based on a total of six one-hour simulations, each representing a different environmental condition form Table 9.3. Axial forces and bending moments are recorded for each of the ten tower segments and thirty-five hull segments, enabling a comprehensive fatigue analysis of the entire structure. RIFLEX software outputs the forces and moments sorted in the local RIFLEX coordinate system. The following transformation from the local RIFLEX coordinate system to the calculation coordinate system for the tower and hull, illustrated in Figure 9.29, with the following definition:

N_x : DOF1 Axial force form RIFLEX

M_y : $-1\cdot$ DOF3 Moment about local y-axis, from RIFLEX

M_z : DOF 5 moment about local z-axis form RIFLEX

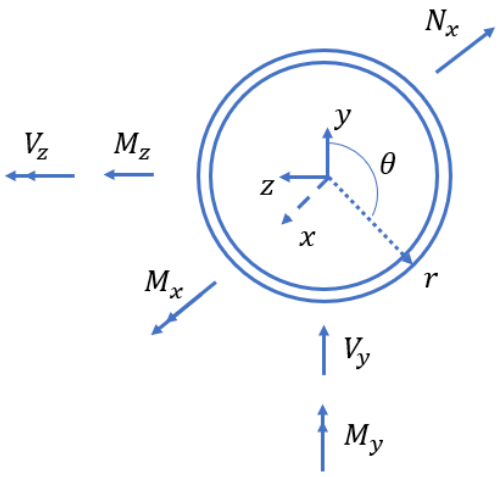

Figure 9.29: Tower Base Fatigue Calculation Coordinate Systems

The SN curve parameters for the steel tower are provided in Table 9.6, to be used in Equation 5.55.

Table 9.6: S-N Curve: D class values

$N \leq 10^7$ cycles		$N > 10^7$ cycles		Fatigue limit at		
m	$\log \bar{a}$	m	$\log \bar{a}$	10^7 cycles	k	t_{ref}
3.0	12.164	5.0	15.606 MPa	52.63	0.20	25 mm

In the analysis of fatigue in the concrete hull, the DNV-GL Offshore Concrete Structures - DNV-0S-C502 rule, described in Section 5.4.3, will be used. These equations requires the correct application

of stress variation range criteria to evaluate fatigue damage in concrete accurately. It should be noted that the scope of this study is limited to examining concrete fatigue life, without assessing reinforcement damage. This limitation is attributed to the early design phase of the structure.

One crucial parameter in concrete calculations is the C_1 factor, which is highly dependent on the variation of structural stress. The value of C_1 is determined by whether the stress blocks exhibit variation in the compression-tension or compression-compression ranges. It is worth mentioning that in the fatigue assessment, none of the stress blocks fell within the compression-tension range. This outcome is unsurprising due to the presence of pre-tension wires that maintain the structure in a constant compressive state. Despite the absence of compressive-tension behavior, a conservative assumption will be made, setting C_1 to 8 instead of 10. This adjustment accounts for the loss of pre-tension in the wires over time.

Furthermore, it is important to recognize that, unlike steel, fatigue in concrete is influenced by the mean stress level. Standard Reinflow counting algorithms typically provide the mean cycle in conjunction with the cycle amplitude and the number of cycles. Consequently, σ_{min} and σ_{max} can be computed by subtracting and adding the amplitude to the mean, as demonstrated in the following equation:

$$\sigma_{max_{i,j}} = \sigma_{i,j} + \sigma_{amp_{i,j}} \tag{9.1}$$

$$\sigma_{min_{i,j}} = \sigma_{i,j} - \sigma_{amp_{i,j}} \tag{9.2}$$

where j refers to the jth stressblokk , i is refferd to the different simulated relaxation, $\sigma_{i,j}$ is the mean stress level and $\sigma_{amp_{i,j}}$ is the cycle amplitude.

The axial force and bending moments are extracted at the base of each element. Since the damage is assessed for each segment, it is possible to represent the fatigue as a function of the structural length.

9.7.2 Fatigue Results

SPAR 1

In Figure 9.30, the 1-hour fatigue damage along the 10 MW tower and hull is presented for six environmental conditions. The most significant damage occurs at z = 36 m, corresponding to the start of segment 2 in the turbine tower. This location exhibits pronounced curvature, consistent with the mode shape shown in Figure 9.16a, as well as slightly higher curvature in the standard bending profile depicted in Figure 9.31. Condition 4 exhibits the highest fatigue damage for the tower. When considering the fatigue life of the concrete hull, distinct differences are observed at different measured positions. For the 270-degree case, the damage is registered above the morning connection point, whereas for the 90-degree case, it occurs at the $COG_{ballast}$. This difference can be attributed to the higher compression experienced in the front region due to elevated average tension and significant weight-bearing. Among all the conditions in Figure 9.30, condition 3 causes the most significant fatigue damage in the hull, characterized by the smallest wind speed but the largest waves.

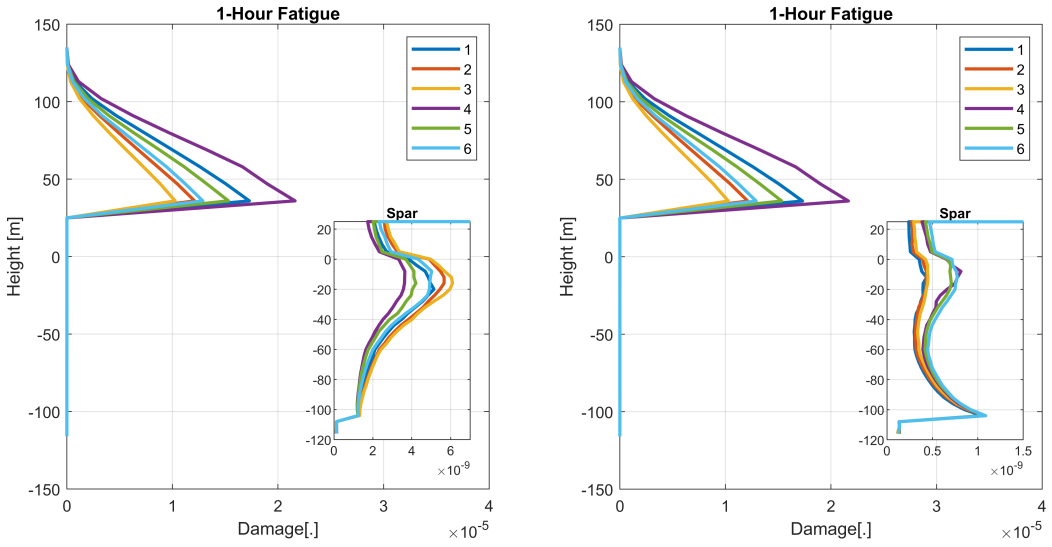

(a) 270 deg (b) 90 deg

Figure 9.30: 1-hour fatigue damage for SPAR 1

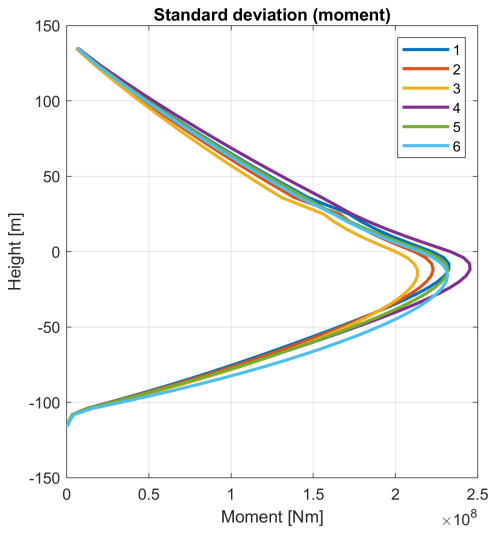

Figure 9.31: Standard deviation of bending moment

SPAR 2

The same trend can be observed for SPAR 2; however, the damage expectancy for the tower remains unchanged. For the concrete hull, it is still LC3 that has the highest damage, and that position 270-degree is the largest.

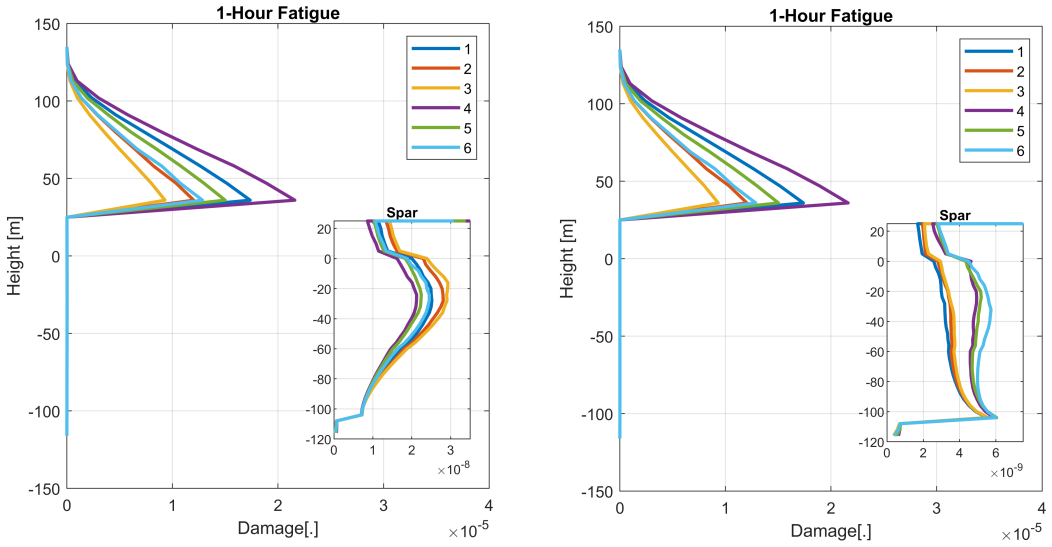

(a) 270 deg (b) 90 deg

Figure 9.32: 1-hour fatigue damage for SPAR 2

Table 9.7 presents the fatigue damage and the fatigue life for the two structures. When comparing the two structures, the steel tower for the two spars predicts the same damage and life expectancy. This is, however, not the case for the SPAR 2 hull, as it appears to experience 4.7 times higher fatigue damage than its smaller counterpart, SPAR 1. Since SPAR 1 and 2 require the same pretension, this factor may strongly influence fatigue life. In addition, with SPAR 2 having a larger cross-section, the pretension force is distributed over a larger area, resulting in lower axial stresses. Consequently, the structure is more prone to experiencing significant compression-compression variations compared to SPAR 1.

Table 9.7: Fatigue Result for SPAR 1 and SPAR 2

	SPAR 1		**SPAR 2**	
	Hull	**Tower**	**Hull**	**Tower**
1- Hour fatigue	6.581e-09	2.164e-05	3.106e-8	2.162e-05
Fatigue Life [Years]	17346	5.28	3675	5.28

9.8 OpenMDAO

The SPAROpt model offers a wide range of potential optimization problems. In this study, the objective of the optimization is to minimize the total weight of the concrete spar hull. The design variables are chosen to represent the hull structure, while the tower remains constant. Constraints are implemented to ensure feasible designs and to prevent failures under extreme conditions. However, it's important to note that the current model only evaluates the dynamic response in a single environmental condition.

9.8.1 Design Variables

In the simplified model, the geometry of the substructure is defined by the design variables, while the tower dimensions remain fixed. The number of design variables is reduced by employing B-splines for the diameter parameters to ease computational efforts. B-splines utilize a fixed number of control points, which in this case is set to 4, to create a smooth distribution for the parameter.

This study's original representation of the diameter parameters consists of 11 design points. However, through the implementation of B-splines, these 11 points are effectively reduced to four, thereby simplifying the computational process. The chosen design variables for the hull design are the spar draft, which represents a single variable, and the outer diameter, which is represented by four variables. This results in a total of five design variables for the hull design. For a concise overview of these design variables, refer to Table 9.8.

Table 9.8: Design variables implemented in the SPAROpt model.

Variable	Unit	**Meaning**
L_{draft}	[m]	Draft of spar (measured vertically)
D_{spar}	[m]	Vector (4 x 1) of outer diameter of hull

9.8.2 Constraints

Constraint functions are essential in determining a design's practicability while guiding the optimizer toward feasible solutions. Crucially, these constraint functions should abstain from dictating any preconceived notions about the optimal design, thereby granting the optimizer maximal flexibility. The current rendition of SPAROpt employs simplified response constraints.

In the existing framework, the capacity control initially applied to concrete is utilized as a constraint, averting designs that could lead to concrete failure. The hydrostatic pitch constraint must possess a positive value to guarantee stability consistently. Moreover, buoyancy and ballast height limitations are set in place to ensure the structure's buoyancy and prevent exceeding the ballast's available space. An additional constraint requiring consideration is to avoid connecting the mooring position beyond the actual length of the structure, with a proposed modification to situate the mooring at the structure's total COG.

Additionally, it is of utmost importance to prevent the optimizer from producing designs with concrete wall thicknesses incapable of withstanding external loads. This promotes appropriate mass distribution and penalizes designs with larger drafts, leading to amplified external pressure loads and increased material usage. Furthermore, constraints are implemented on the surge and pitch to avert excessive loading on the power cable and the turbine/hull, setting a 1-hour expected maximum value of 20 meters and 15 degrees, respectively. The diameter of the hull segments is constrained to avoid abrupt changes and ensure manufacturability by limiting the taper angle of each segment to 20 degrees. It's worth mentioning that this first approach abstains from incorporating any cost constraints in the optimization process. A representation of the primary constraints is provided in Table 9.9

Table 9.9: Design constraints in SPAROpt

Design constraint	**Value**
Prob max surge [m]	< 20
Prob max pitch [deg]	< 15
T_{11} [s]	> 50
T_{33} [s]	> 25
T_{55} [s]	> 25
T_{77} [s]	> 2.0
Hydrostatic pitch	> 0.0
COG and COB ratio	> 0.0
M_{ball} [kg]	> 0.0
Taper angle hull [deg]	< 20

9.8.3 Exploring the Design Space

Before an optimization can take place, a design space exploration is performed. This implies that a set of different designs is generated. This aims to identify errors in the design and calibrate the constraints that were set. For this exploration, a constant diameter is used. As mentioned in Section 7.3, DOE does not guarantee constraint satisfaction in all cases. From this test, it was noted the following:

1. Drafts over 120 m seem to cause large normalized mode shapes, which in SPAROpt is set to a maximum of 1.0. The values SPAROpt generated were much larger than the maximum allowed. This may indicate some conflicts in the design space above this draft that may lead to inefficient buoyancy.
2. Drafts under 85 meters often caused NaN values for probabilistic maximum pitch, surge, and the same for first bending. This is caused by negative pitch stiffness leading to insufficient stability for the considered design.
3. Diameters under 10 meters lead to hydrostatic instability in pitch, giving designs with larger pitching due to not enough buoyancy.
4. The probabilistic maximum of surge in most cases was between 35-40 meters. This is strongly affected by the mooring design, which is not a part of the objective, and more attention to reducing the surge offset must be studied.

Adjusting these constraints significantly reduces faulty designs and errors and enables a broader design space. Figure Figure 9.33, illustrates the distribution of mass and wall thickness throughout the design space. As expected, an increase in draft and diameter leads to a corresponding increase in weight. Similarly, considering the thickness, depth, and diameter is anticipated to increase the wall thickness to ensure the wall's capacity to withstand external loads.

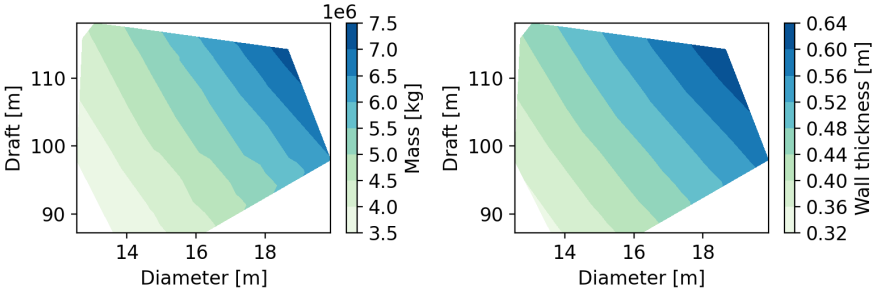

Figure 9.33: Design exploration when considering mass and thickness of the structure.

Several observations can be made when evaluating the structural performance in terms of natural periods. Firstly, the surge natural period (T_{11}) is primarily influenced by the mooring system, which remains unchanged in the design exploration. It is evident that the natural period increases with draft and diameter, resulting in a larger structure, increased added mass, and a slower response to external forces. This same trend can be observed for the natural period in heave (T_{33}) due to increased added mass.

For the pitch natural period (T_{55}), a larger diameter spar generally exhibits a longer natural period. This phenomenon can be attributed to the larger diameter providing greater inertia. In the lower-left corner of the graph, a constraint violation is observed, indicating that a smaller diameter leads to a pitch natural period towards 100 seconds, which is not the case. Additionally, the increasing draft and diameter influence the first bending moment (T_{77}), which tends to prolong the pendulum period.

Based on these findings, it can be deduced that the probabilistic maximum displacement in surge follows a similar trend, primarily influenced by the weight of the structure. A smaller structure is more easily displaced than a heavier one. Similarly, the probabilistic maximum pitch displacement demonstrates that larger diameters and drafts contribute to increased restoring forces, leading to reduced pitching motion.

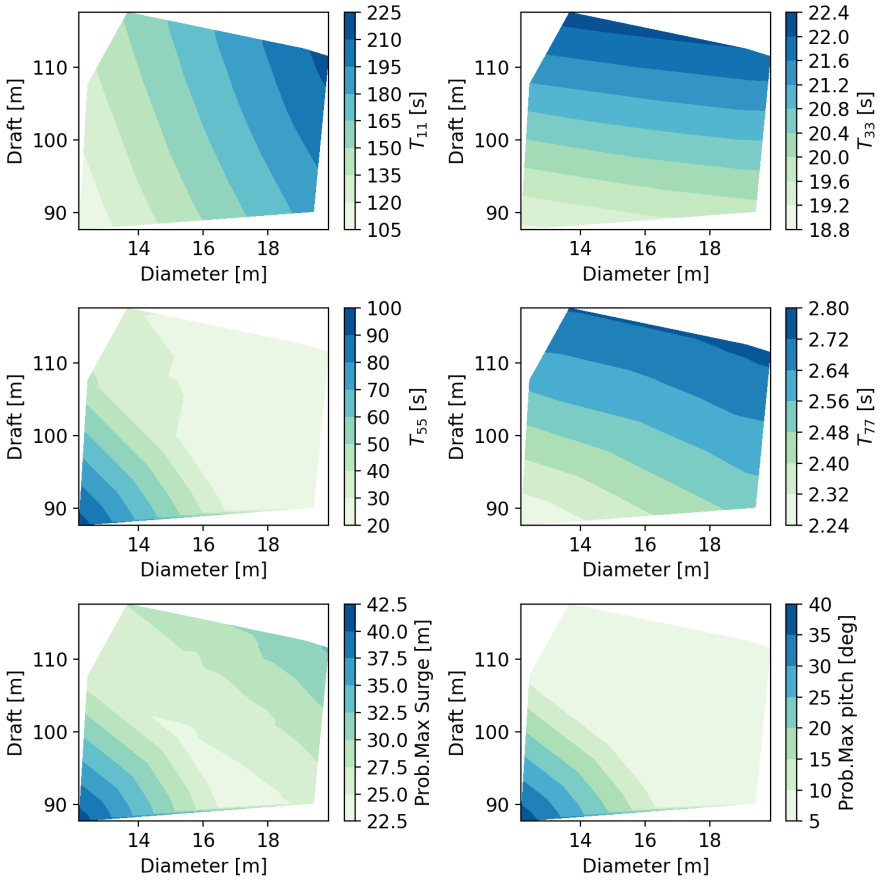

Figure 9.34: Design exploration when considering Natural periods and probabilistic max response.

A contour plot illustrating the concrete capacity control, conducted from Section 9.6.2 to Section 9.6.2, reveals an expected behavior. However, it is crucial to recognize that these capacity contours are strongly influenced by the hull's thickness. DOE generates larger thickness values based on depth and diameter. Consequently, in some cases, the capacity at the bottom of the structure may be greater than that closer to the surface, primarily due to reduced wall thickness requirements higher up. The findings of this study can be found in Appendix Section B.

The following environmental conditions used in the optimization are presented in Table 9.10.

Table 9.10: Environmental conditions for extreme response calculations. (Hegseth, [34])

Condition	**1**	**2**	**3**
Mean wind speed at hub height, U [m/s]	13.0	21.0	50.0
Significant wave height, H_s [m]	8.1	9.9	15.1
Spectral peak period, T_p [s]	14.0	15.0	16.0

9.8.4 Optimized Designs

In this study, two optimization approaches were performed to reduce the weight of the hull structure. The first optimization utilized the necessary thickness Equation 5.40, derived in Section 9.6.2, while the second optimization employed a constant minimum thickness (t = 0.35 m). The aim of both optimizations was to find an optimal hull design that minimizes weight while satisfying the given constraints. The results of these optimizations will be presented and analyzed in the following sections.

Concrete Capacity Based Thickness

The primary focus of optimization is determining the optimal thickness of the structure, taking into account the hoop stress induced by water pressure. This calculation considers the depth and diameter of the section. The results of this optimization are presented in Figure 9.35, which illustrates a three-dimensional illustration for three extreme load cases.

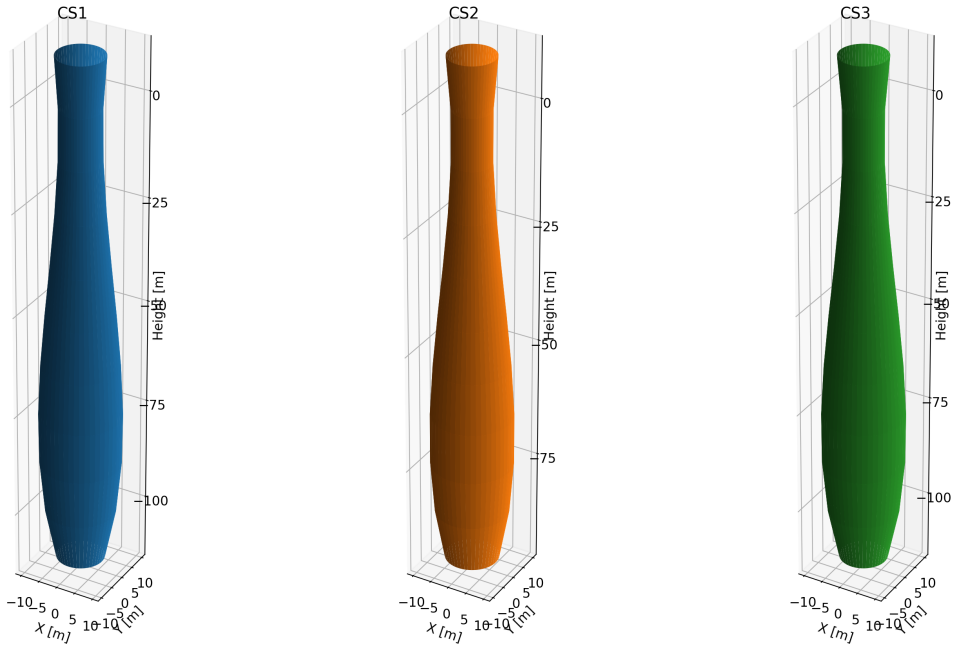

(a) $U = 13, H_s = 8.1, T_p = 14$ (b) $U = 21, H_s = 9.9, T_p = 15$ (c) $U = 50, H_s = 15.1, T_p = 16$

Figure 9.35: Geometrical representation of the CS1-3

In Figure 9.36, the distribution of diameters along the length of the structure is illustrated. The platform beneath the wave zone adopts a vase-like shape, increasing the distance between the COB and the COG. This enhances pitch restoring stiffness. On the other hand, for CS2, a smaller draft and a relatively larger bottom diameter are observed, leading to increased added mass and a natural period in heave. In comparison to the original spars denoted with (*), notable modifications are evident, prominently influenced by factors such as water pressure at the bottom, ensuring buoyancy through the increased diameter, and reducing diameter near the surface to mitigate environmental

exposure. These changes represent a significant departure from the original design and reflect careful consideration of key factors to enhance performance and adaptability. The intriguing behavior observed at the top, characterized by an enlargement of the spar's diameter, suggests a potential need for increasing the diameter to enhance structural strength near the turbine's connection point. This enlargement specifically reinforces the spar's integrity in the critical region where it interfaces with the turbine. By augmenting the diameter in this area, it is anticipated that the structural capacity will be maintained to effectively withstand the loads and stresses exerted by the turbine, thereby ensuring a robust connection between the spar and the turbine. This deliberate design modification demonstrates a particular approach to optimizing the spar's performance and safeguarding its structural integrity at the crucial junction with the turbine system.

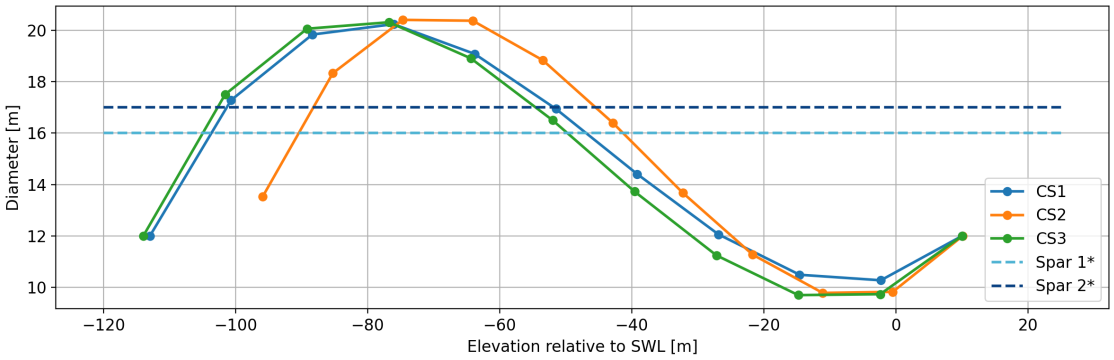

Figure 9.36: Diameter distribution for CS1-3

The thickness distribution is presented in Figure 9.37, as a function of the draft. It is evident in all models that the lower part of the structure requires a larger wall thickness to withstand the external pressure, considering the suggested diameter. The spar's wall thickness adheres to the minimum allowable thickness (0.35m) from approximately -80m. Since the objective is to reduce spar weight, the optimization directs the design towards this specific thickness, which is determined based on the spar's draft and diameter. Compared to the original spars denoted with (*), a larger reduction in wall thickness leads to less material use. The reason for this reduction is based on the concrete capacity discussed in Section 9.6.2, where the capacity usage for this particular area is low, enabling the possibility of reducing the thickness. As the structure starts to approach the water surface, the water pressure decreases, allowing for an increased diameter while maintaining the same wall thickness. The larger wall thickness at the bottom lowers the COG, and with the decreasing pressure, the hull becomes lighter, and the diameter increases, resulting in an increased distance between COG and COB, as mentioned earlier. Approaching the surface, the structure curves inwards, reducing the overall exposed area and minimizing environmental loading. These trends align with the specified objectives and constraints and show similar trends observed by Hegseth [34]. It is also important to note that all concrete capacity requirements have been met, demonstrating that the structure complies with the design criteria.

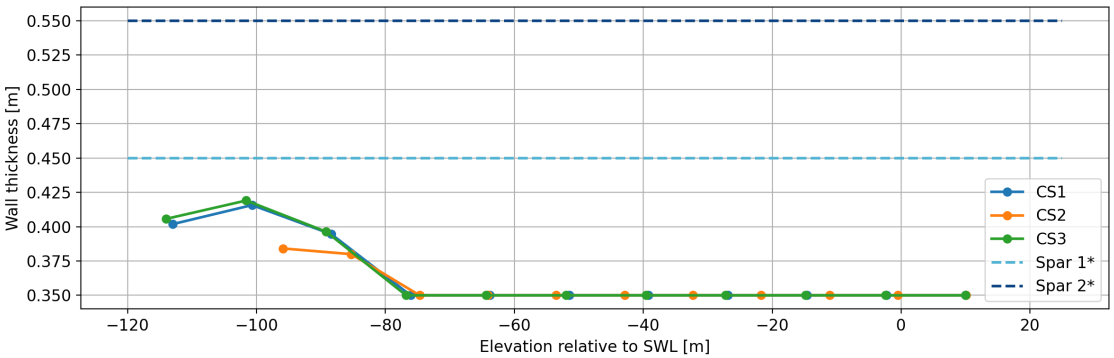

Figure 9.37: Thickness distribution for CS1-3

Table 9.11 presents the performance of each model. Draft and surge, differences are observed among the different structures. Increasing the length of the spar can result in larger environmental forces due to excitation from waves. These forces need to be absorbed by the mooring system, as indicated by the probabilistic maximum surge displacement, where the larger structure experiences greater offsets. Regarding pitch, significant differences are observed in the probabilistic maximum pitch. CS1 experiences the largest pitching, while CS2-3 exhibits similar responses. This discrepancy may be attributed to the larger waterplane, which increases hydrodynamic forces in this region. It should also be noted that CS3's wind turbine is not operative at this wind speed, resulting in less force exposure on the turbine and reducing overall pitching. The heave period for all models falls within the same range. Differences may arise due to longer drafts, increased added mass, or decreased waterplane area. Since CS1 and CS3 share the same heave period, the disparity for CS2 may be attributed to variations in the SWL area and draft. However, the differences among all models are relatively minor, making it challenging to determine the exact cause.

Table 9.11: Preformance for CS1-3

	CS1	CS2	CS3
Draft [m]	113	95.9	114
Prob.Max Surge [m]	37.7	24.4	33.4
Prob.Max Pitch [deg]	12.9	7.23	7.96
T_{11} [s]	132	145	149
T_{33} [s]	25.6	24.4	25.6
T_{55} [s]	30.4	35	31.2
T_{77} [s]	2.66	2.44	2.68
$tot_{M_{spar}}$ [tonnes]	4.8759e+03	4.1415e+03	4.8608e+03

Constant Thickness

A subsequent optimization attempt was conducted, this time introducing a constant thickness constraint with a value of 0.35 m while allowing for changes in the diameter. The optimized support structure for CS4-6 is presented as three-dimensional figures in Figure 9.38. The platform beneath the wave zone still generates a vase-like shape, which still increases the distance between the COB and the COG, consequently enhancing pitch and restoring stiffness.

(a) $U = 13, H_s = 8.1, T_p = 14$ (b) $U = 21, H_s = 9.9, T_p = 15$ (c) $U = 50, H_s = 15.1, T_p = 16$

Figure 9.38: Geometrical representation of the CS4-6

Figure 9.39 shows a more noticeable difference in diameter compared to CS1-3. However, the same pattern can be observed, where reducing the structure's depth decreases water pressure and allows for a larger diameter. The thickness of the structure plays a role in driving the diameter variation, so it is expected to have a larger difference. One noticeable difference is that CS4-6 has smaller diameters, which results in slimmer and smoother structures. As the structure gets closer to the surface, it curves inward, reducing the exposed area and minimizing the impact of the environmental loads. These trends align with the objectives and constraints set for the design. It's important to note that all the required concrete capacity standards have been met, indicating that the structure performs according to the design criteria.

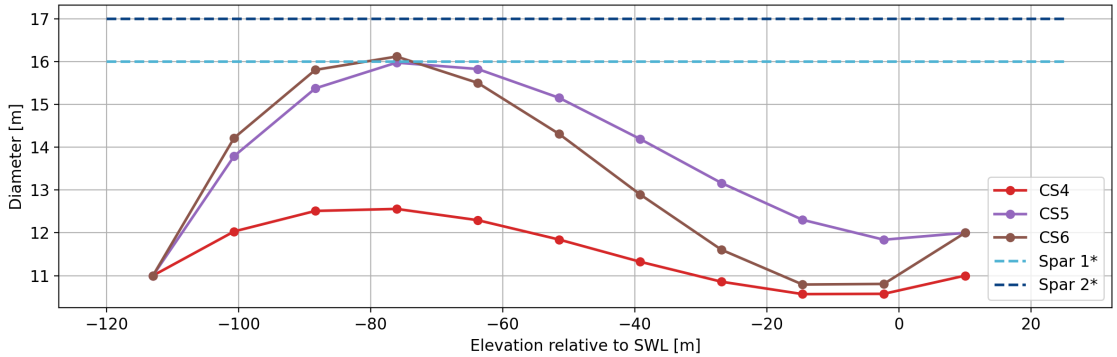

Figure 9.39: Diameter distribution for CS4-6

In Table 9.12, the performance for CS4-6 is presented. It is seen that all models take the same draft. Compared to CS1-3, similar trends are noticed, with minor differences.

Table 9.12: Preformance for CS4-6

	CS4	**CS5**	**CS6**
Draft [m]	113	113	113
Prob.Max Surge [m]	35.2	26.4	32.7
Prob.Max Pitch [deg]	11.6	6.44	9.1
T_{11} [s]	127	148	133
T_{33} [s]	30.4	31.7	36.4
T_{55} [s]	25.9	25.6	25.6
T_{77} [s]	2.63	2.64	2.66
$tot_{M_{spar}}$ [tonnes]	4.3829e+03	4.3178e+03	4.0704e+03

A noticeable distinction in geometry is observed when comparing the case studies. In CS1-3, there is a significant variation in diameter and thickness throughout the structure, while in CS4-6, the diameter remains smaller due to a constant thickness. From a practical perspective, constructing geometries with such complex variations can present challenges and potentially lead to higher construction costs. The feasibility and manufacturability of the designs should be carefully considered, taking into account the practical limitations and cost implications associated with the chosen geometry.

When examining the total spar mass of SPAR 1 and 2 compared to the six new structures, it is evident that SPAR 1 and 2 have an average mass 1.8 and 2.3 times greater, respectively, compared to the new designs. However, while there are some performance differences, the significance of these differences is debatable, and it may be challenging to draw conclusive results. Nevertheless, based on the weight difference of the structures, the optimization process appears to have achieved a potential cost objective.

Additionally, other objectives were explored, including material cost and maximum pitch in a probabilistic sense. Not surprisingly, the cost follows a similar trend to the total mass objective, as they increase proportionally. Minimizing the probabilistic maximum pitch results in slimmer designs with larger drafts, as shifting the COG further down in the water enhances overall stability by increasing the distance between the COG and the COB.

It is important to note that the current optimization model does not yet consider the cost of reinforcement, tension wires, and manufacturing. These factors could have a more significant influence and potentially alter the geometry of the design. Furthermore, it is crucial to ensure that there is an available port capable of accommodating structures with larger drafts, as spars typically require suitable port facilities.

10 Conclusion and Recommendations for Further Work

The conclusion of this thesis highlights the key findings and implications of the study. The investigation aimed to explore the implementation of concrete structures into a simplified linearized frequency domain optimization model for offshore wind turbines. The analysis focused on comparing nonlinear and linearized models, evaluating natural periods, potential flow results, spectral comparisons, internal forces, concrete capacity, fatigue analysis, and design optimization using the OpenMDAO framework.

The potential flow analysis revealed a noticeable distinction between the nonlinear and linearized spar opt models. In the surge motion, wave excitation was lower for sParopt models at higher wave frequencies ($\omega > 0.6$), while pitch excitation was overestimated for lower frequencies ($\omega < 0.4$). This outcome was expected since SPAROPT enables MCF. The added mass is greater for SPAROpt models in surge, heave, pitch, and the coupled surge-pitch, and it remains frequency independent due to its reliance on the strip theory. Damping analysis revealed that the larger SPAR 2 exhibited greater damping attributed to its larger geometry. The constant wind test yielded reassuring results, and the rotor behaved as expected.

The decay test revealed similar surge, heave, and pitch outcomes, indicating consistent natural periods. However, the flexible spar exhibited lower yaw natural periods due to variations in mass distribution. At the tower base, the first pitch bending natural frequency demonstrated that all models had natural frequencies in the 3P range, with slight variations between them.

The spectral comparison results indicated that SIMA and SPAROpt exhibited similar response shapes under wave and wind conditions. Nevertheless, SPAROpt had certain limitations, consistently underestimating specific response parameters due to its simplified modeling approach. Despite this, the standard deviation of both models' responses suggests that the relative strengths and variances within the frequency components are preserved. This implies that while SIMA offers a more comprehensive analysis, SPAROpt remains a valuable tool for the initial assessment and comparison of different SPAR designs and environmental conditions. However, notable discrepancies in bending were observed during the transition from concrete to steel, resulting in significantly larger excitation in SPAROpt. This can be attributed to the substantial difference in curvature in this region and the abrupt change in cross-sectional size.

The analysis of internal forces in the structure reveals significant trends and stresses. The distribution of shear forces is influenced by the ballast load, while bending moments exhibit expected behavior, with the highest bending moment occurring in the fairlead regions. Variations in thickness and geometric differences impact axial and shear stresses. These findings underscore the importance of considering structural design in offshore structures.

The assessment of concrete capacity in the spar structures uncovers several important findings. The ratio between the required pretension and the yielding strength of the rebar indicates the stress capacity of the prestressed concrete steel. Negative pretension values are observed at depths below -80 m to -120 m, resulting from axial stresses surpassing tensile stresses caused by the moment, leading to naturally compressed sections. Both Spar 1 and Spar 2 maintain ratios below the failure threshold, with SPAROpt tending to overestimate the ratio. Short-term axial stresses remain within acceptable limits, and long-term axial stresses consistently remain below the allowable stress threshold, indicating safe and reliable operation over an extended period.

Concrete shear cracks and buckling are also evaluated. The stress ratios of axial stress to allowable compressive stress remain below the limits for both spars. SPAROpt predicts a higher compressive ratio, primarily due to the overestimation of pretension in certain areas. Concrete buckling capacity resulting from hydrostatic pressure demonstrates good agreement between the SIMA and SPAROpt methods, achieving the desired capacity range. Buckling due to axial stress and shear stress is considered minimal, with slight shifts observed in specific areas due to the wind turbine tower, ballast, and the transition from concrete to spar. Overall, the structures exhibit satisfactory concrete capacity and resilience against buckling.

The fatigue analysis of Spar 1 and Spar 2 revealed that both turbine towers had the same fatigue life, indicating that the size differences in the hull did not result in an extended life for the tower.

The expected life of the tower was slightly over five years, which aligns with its land-based design expectations. Regarding concrete hull fatigue, important findings emerged due to significant differences in fatigue life. The slightly larger Spar 2 exhibited a 4.7 times larger fatigue damage, suggesting that a larger cross-sectional area leads to less axial stress from retention, resulting in larger variations in compression fatigue and, ultimately, a shorter life. However, it is crucial to note that the expected lifetime of the concrete hull is much larger than what would be dimensioned for an expected hull. Therefore, the concrete's fatigue life is not the design's driving factor.

In this study, the OpenMDAO framework was employed to optimize the design of a concrete spar hull structure for offshore wind turbines. The objective was to minimize the total weight of the structure while considering various design variables and constraints. The use of B-splines for diameter parameters reduced the number of design variables and simplified the computational process. Constraint functions were incorporated to ensure feasible designs and prevent failures under extreme conditions.

The exploration of the design space yielded important insights into the behavior of the structure under different environmental conditions. Adjustments were made to the constraints to improve the design space and eliminate faulty designs. The optimized designs were evaluated based on performance metrics such as draft, surge, pitch, and natural periods. The results of the design exploration demonstrated the effect of each parameter. Two optimization approaches were employed: one considering the necessary thickness based on concrete capacity, and the other imposing a constant thickness constraint. Both approaches led to optimized designs with varying diameters and thicknesses along the structure. The designs exhibited vase-like shapes and demonstrated improved stability and performance characteristics. However, it is important to consider the complexity of the optimized geometries, as they may pose challenges in terms of manufacturability and cost. The optimized structures exhibited significant weight reductions compared to the reference designs, indicating potential cost savings. Although other objectives, such as material cost and maximum pitch, were explored, future analyses should incorporate considerations such as reinforcement, tension wires, and manufacturing costs.

Overall, this study showcased the effectiveness of the OpenMDAO framework in optimizing the design of offshore wind turbine structures. The results provide valuable insights for developing lightweight and efficient concrete spar hull designs, contributing to advancing offshore renewable energy systems.

Further Work

- Investigating alternative optimization algorithms to improve the efficiency and accuracy of the design optimization process.
- Incorporating a more comprehensive cost analysis to evaluate the economic viability of the optimized designs. In addition, evaluate the environmental impact of concrete spar structures, including their construction, operation, and decommissioning phases, to ensure sustainable development practices.
- Conducting experimental testing to validate the performance and structural integrity of the optimized concrete spar hull designs.
- Exploring different concrete qualities and their combinations for the construction of spar hulls to assess their impact on weight reduction, cost, and overall performance.
- Considering the dynamic response of the optimized spar structures under extreme loading conditions and assessing their long-term durability.
- Evaluating the environmental impact of concrete spar structures, including their construction, operation, and decommissioning phases, to ensure sustainable development practices in the offshore wind industry.

Bibliography

[1] NS-EN 1992-1-1:2004+A1:2014+NA:2018. *Eurokode 2: Prosjektering av betongkonstruksjoner*. Del 1-1: Allmenne regler og regler for bygninger. Lysaker: Standard Norge. 2018.

[2] C. Bak et al. *The DTU 10-MW Reference Wind Turbine*. URL: https://backend.orbit.dtu.dk/ws/portalfiles/portal/55645274/The_DTU_ (visited on 14th Nov. 2022).

[3] L. Liange et al. *Dynamic and structural performances of offshore floating wind turbines in turbulent wind flow*. 2019.

[4] M. Scheu et al. *Human exposure to motion during maintenance on floating offshore wind turbines*. Ocean Engineering, 2018.

[5] M. Yue et al. *Effects of heave plate on dynamic response of floating wind turbine Spar platform under the coupling effect of wind and wave*. Ocean Engineering, 2020.

[6] T. Burton et al. *Wind Energy Handbook*. John Wiley Sons, Ltd, 2011.

[7] T. et al. Ashuri. *Multidisciplinary design optimization of large wind turbines—technical, economic, and design challenges*. 2016.

[8] T. et al. Ashuri. *Multidisciplinary design optimization of offshore wind turbines for minimum levelized cost of energy*. 2014.

[9] E. E. Bachynski and T. Moan. *Design considerations for tension leg platform wind turbines*. 2012.

[10] E. E. Bachynski-Poli´c. *Basic aerodynamics for wind turbines*. Earthscan, 2022.

[11] E.E. Bachynski-Polić. *Integrated aero-hydro-servo-elastic analysis (Lecture notes)*. Department of Marine Technology Norwegian University of Science and Technology, 2022.

[12] E.E. Bachynski-Polić. *Introduction to offshore wind power and technology (Lecture notes)*. Department of Marine Technology Norwegian University of Science and Technology, 2022.

[13] Stig Berg and Sigmund kyrre Ås. *Fatigue and Fracture Design of Marine Structures, Third revised edition*. Berge,Stig, 2006.

[14] Norsk Betongforening. *Lavkarbonbetong, Publikasjon nr. 37*. 2020.

[15] Dr. Birol. *The DTU 10-MW Reference Wind Turbine*. URL: https://www.iea.org/reports/offshore-wind-outlook-2019.

[16] M. Bjerke. *Guidelines for Design and Construction of Slipformed Concrete Structures*. Norsk Betongforening, 2018.

[17] A. Camões and R.M. Ferreira. *Technological evolution of concrete: from ancient times to ultra high-performance concrete*. Department of Civil Engineering, University of Minho, Portugal, 2010.

[18] *Cement and Concrete*. URL: https://www.cement.org/cement-concrete (visited on 4th Oct. 2022).

[19] K.-H. et al. Chew. *Optimization of offshore wind turbine support structures using an analytical gradient-based method*. 2015.

[20] I. Holand E. Jersin and O. T. Gudmestad. *Design of Offshore Concrete Structures*. Spon Press, 2000.

[21] Equinor. *Neste fase i Hywind Tampen-prosjektet*. URL: https://www.equinor.com/no/news/archive/20210422-next-step-hywind-tampen (visited on 4th Dec. 2022).

[22] Equinor. *Starter byggingen av verdens største flytende havvindpark*. URL: https://www.equinor.com/no/news/archive/20201001-contruction-start-hywind-tampen (visited on 4th Dec. 2022).

[23] O.M. Faltinsen. *Sea Loads on Ships and Offshore Structures*. Cambridge University Press, 1993.

[24] A.E. Fiorato. *Inspection guide for reinforced concrete vessels, volume 2*. U.S.Department of Transportation: United States Coast Guard, 1981.

[25] Betong Fokus. *Lokal og kortreist verdiskapning.* URL: https://www.betongfokus.no/2022/03/10/kortreist-og-lokal-verdiskapning/ (visited on 4th Dec. 2022).

[26] K. T. Fosså. *Slipforming of Vertical Concrete Structures.* Norwegian University of Science and Technology, 2001.

[27] N. K. FOUGNER. *Seagoing and other concrete ships.* London, H. Frowde and Hodder Stoughton, 1922.

[28] I. Fuglestad. *Aker Solutions.* Personal communication. 16.11.2022.

[29] I. Fylling and P. A. Berthelsen. *WINDOPT: An optimization tool for floating support structures for deep water wind turbines.* 2011.

[30] G.F.Clauss and L.Birk. *Hydrodynamic shape optimization of large offshore structures.* 1996.

[31] GLOBAL.WIND.ATLAS. URL: https://globalwindatlas.info/en/download/high-resolution-maps/OFFSHORE.

[32] M. Greco. *TMR4215: Sea Loads, Lecture Notes.* DEPT. OF MARINE TECHNOLOGY, NTNU, 2021.

[33] Martin O. L. Hansen. *Aerodynamics of Wind Turbines, Second Edition.* Earthscan, 2008.

[34] J. M. Hegseth. *Efficient Modelling and Design Optimization of Large Floating Wind Turbines. PhD thesis.* NTNU, 2020.

[35] J. M. Hegseth and E. E. Bachynski. *A semi-analytical frequency domain model for efficient design evaluation of spar floating wind turbines.* 2019.

[36] IRENA. *Floating Foundations: A Game Changer for Offshore Wind Power, 2016.* URL: https://www.irena.org/publications/2016/Dec/Floating-foundations-A-game-changer-for-offshore%20wind.

[37] IRENA. *Nurturing offshore wind markets: Good practices for international standardisation, 2018.* URL: https://www.irena.org/publications/2018/May/Nurturing-offshore-wind-markets.

[38] A. L. Rogers J. F. Manwell J. G. McGowan. *Wind Energy Explained: Theory, Design and Application, Second Edition.* John Wiley Sons, Ltd, 2009.

[39] S. Jacobsen. *Concrete Technology 1.* Norwegian University of Science and Technology, 2009.

[40] E. Juliebø. *Betongfaget - Betongarbeid.* 2015.

[41] K. Kazer. *Here's where to see a concrete WWI ship built in Alabama.* URL: https://www.al.com/life/2020/02/heres-where-to-see-a-concrete-wwi-ship-built-in-alabama.html (visited on 4th Dec. 2022).

[42] I. Langen and R. Sigbjørnsson. *Dynamisk analyse av konstruksjoner.* TAPIR, 1979.

[43] C. M. Larsen and E.E Bachynski-Polić. *Dynamisk analyse av konstruksjoner.* Cambridge University Press, 1990.

[44] F. et al. Lemmer. *Optimization of floating offshore wind turbine platforms with a self-tuning controller.* 2017.

[45] *Marine concrete structures - Engineering services for concrete structures in hostile environments.* URL: https://www.multiconsult.no/assets/CONCRETE_brochure_ORIG.pdf.

[46] J. R. R. A. Martins and A. Ning. *Engineering Design Optimization.* Unpublished draft, 2020.

[47] A. Naess and T. Moan. *Stochastic dynamics of marine structures.* Cambridge University Press, 2012.

[48] Norcem. *God betong er bestandig, 2018.* URL: https://www.norcem.no/sites/default/files/assets/document/godbetongerbestandig%5C_web.pdf.

[49] Norcem. *Standardsement: Produksjonsinformasjon.* URL: https://www.betomur.no/file/filer-fra-uni-okonomi/1023500-standardsement-fa-datablad.pdf.

[50] Standard Norge. *NS-EN 206: Concrete Specification, performance, production and conformity.* Norsk Stander, 2021.

[51] Omib. *Principle of Prestressing.* URL: http://omibnotes.blogspot.com/2010/08/principle-of-prestressing.html.

[52] F. Ormel. *Presentation of Power Curve Uncertainty to PCWG*. Chief Specialist Product Performance, Vestas, 2015.

[53] L. Ramirez. *Ports: a key enabler for the floating offshore wind sector*. WindEurope, 2020.

[54] F. et al. Sandner. *Integrated optimization of floating wind turbine systems.* 2017.

[55] Hiroto Inoue Sho Oh and Yuya Takahashi. 'Structural Design of a Prestressed-Concrete Spar-type floater for 10 MW wind turbines'. In: (Oct. 2020). DOI: 10.1088/1742-6596/1669/1/012012. URL: https://dx.doi.org/10.1088/1742-6596/1669/1/012012.

[56] Aker Solutions. *Hywind Tampen – Floating Offshore Wind*. URL: https://www.akersolutions.com/what-we-do/projects/hywind-tampen/ (visited on 4th Dec. 2022).

[57] C.E.S.d. Souza and E.E. Bachynski-Polić. *Design, structural modeling, control, and performance of 20 MW spar floating wind turbines*. 2021.

[58] Jan van der Tempel. *Design of Support Structures for Offshore Wind Turbines*. PhD thesis. Delft, the Netherlands, 2006.

[59] C. Tracy. *Parametric design of floating wind turbines.* 2007.

[60] Det Norske Veritas. *DNV-ST-C502: Offshore concrete structures*. DNV, 2018.

[61] Det Norske Veritas. *ENERGY TRANSITION OUTLOOK 2022*. DNV, 2022.

[62] Det Norske Veritas. *Environmental conditions and environmental loads*. DNV, 2014.

Appendix

A Spectral Analysis

A.1 SPAR 1 Wind and Wave, Wave-only, Wind only

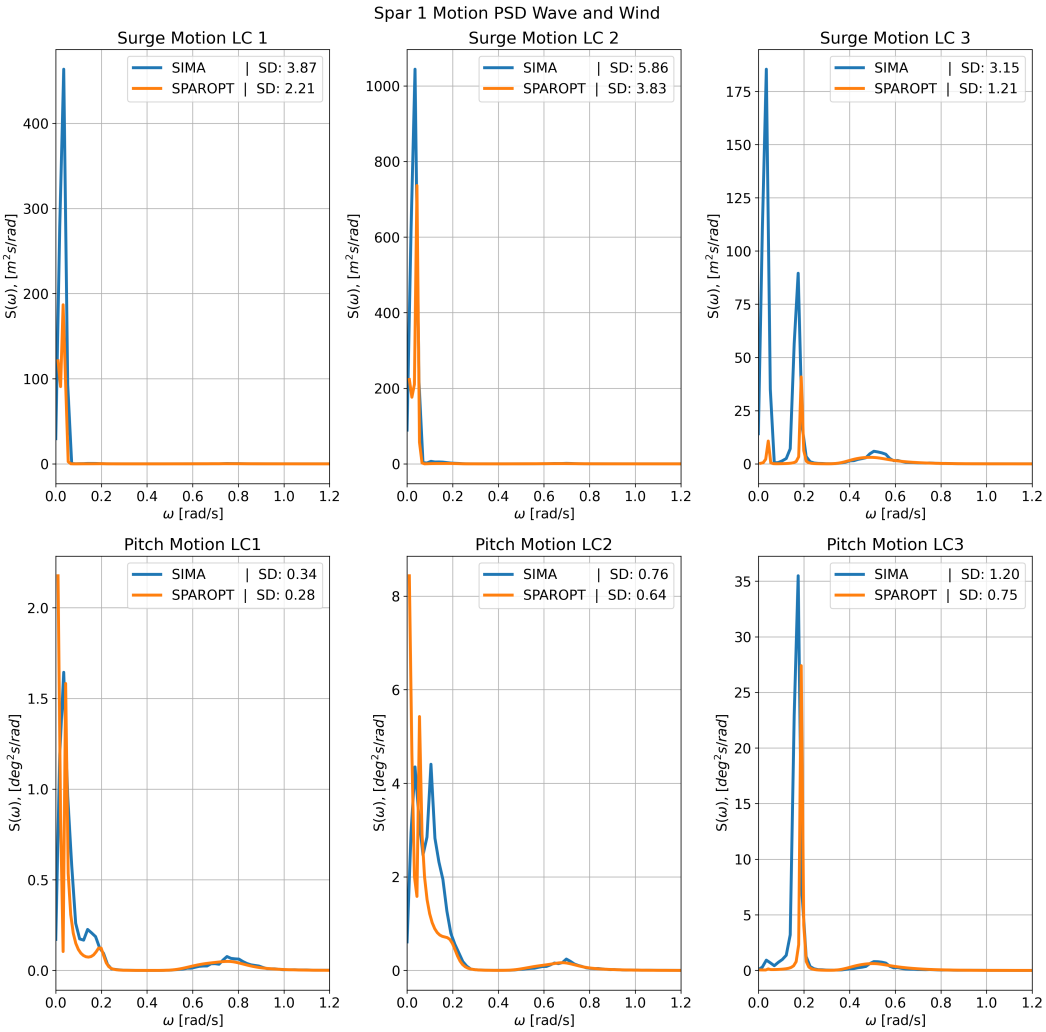

Figure .1: Spar 1 Motion PSD Wave and Wind

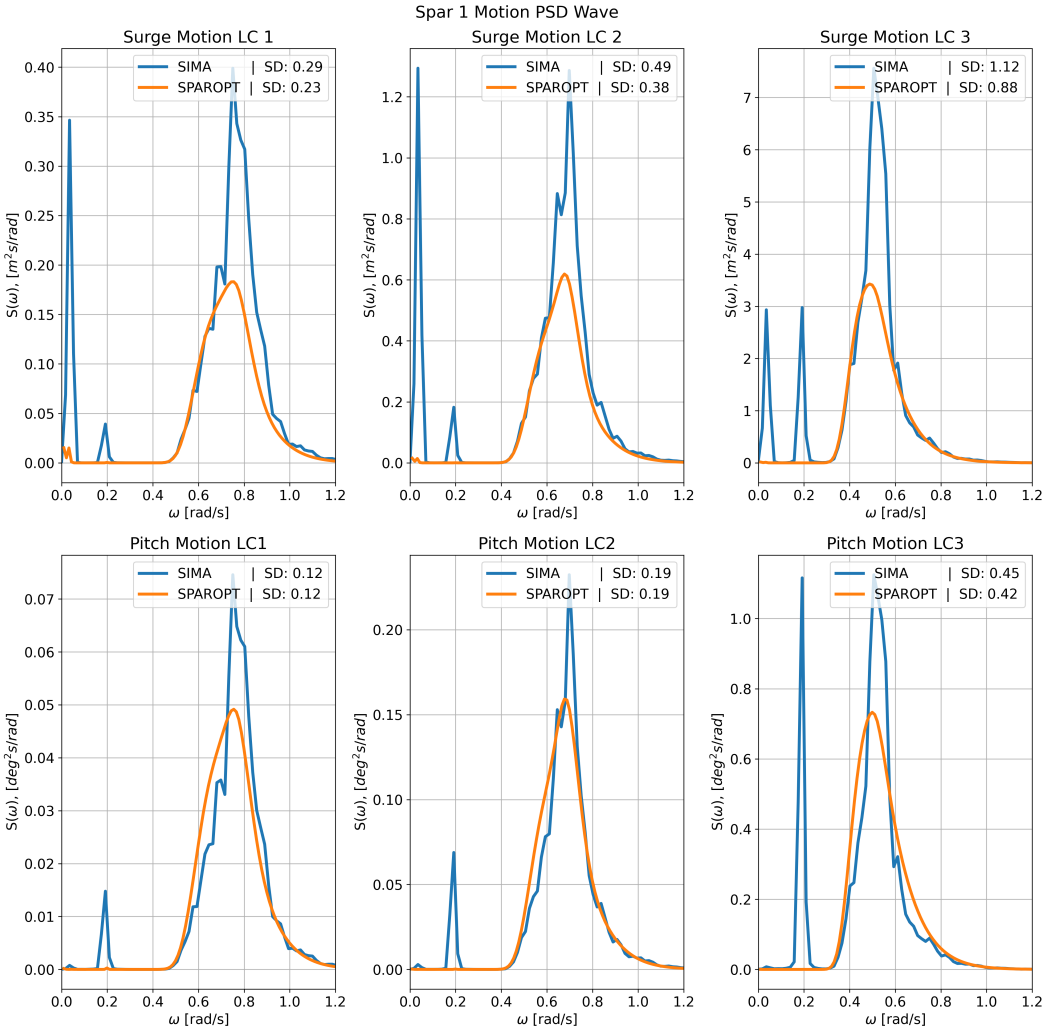

Figure .2: Spar 1 Motion PSD Wave

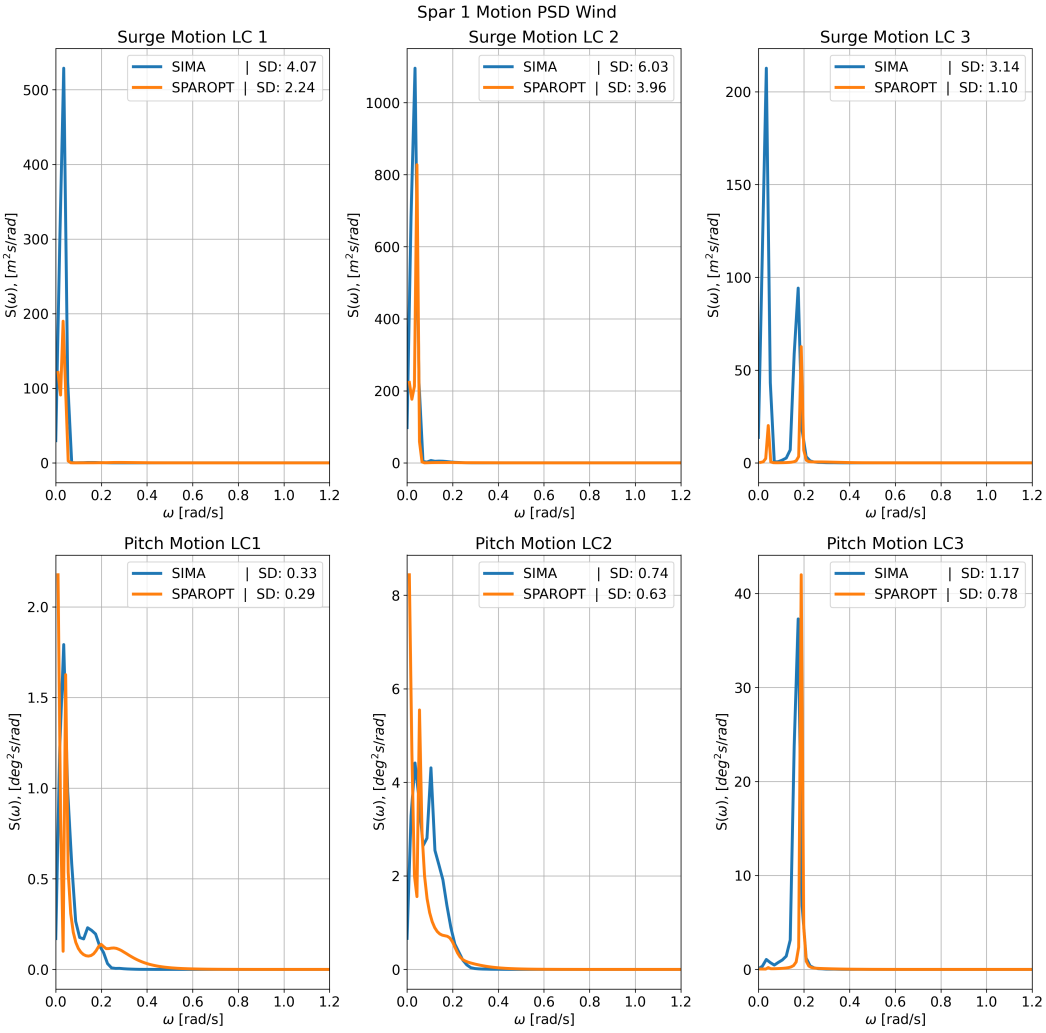

Figure .3: Spar 1 Motion PSD Wind

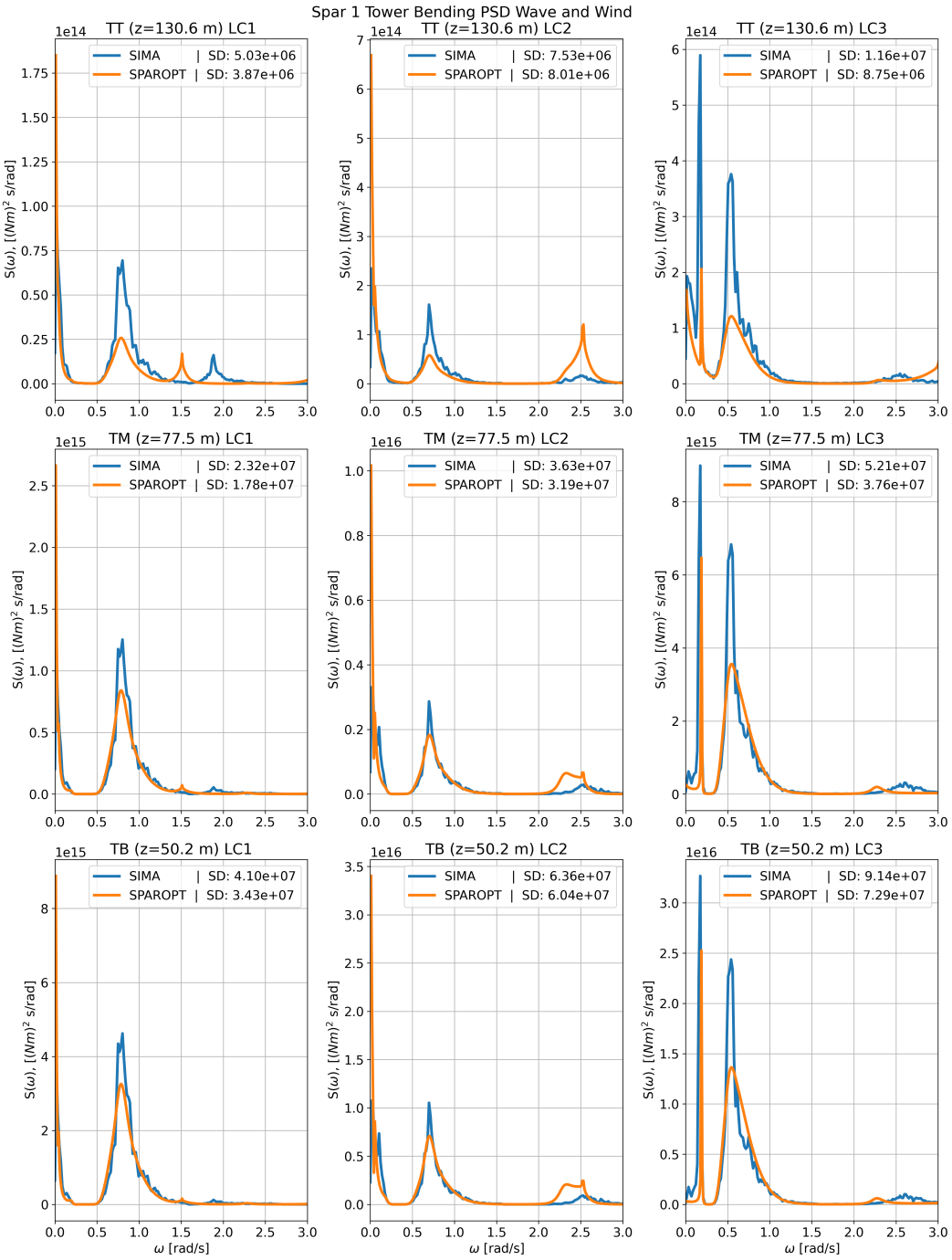

Figure .4: Spar 1 Bending Moment Tower PSD Wave and Wind

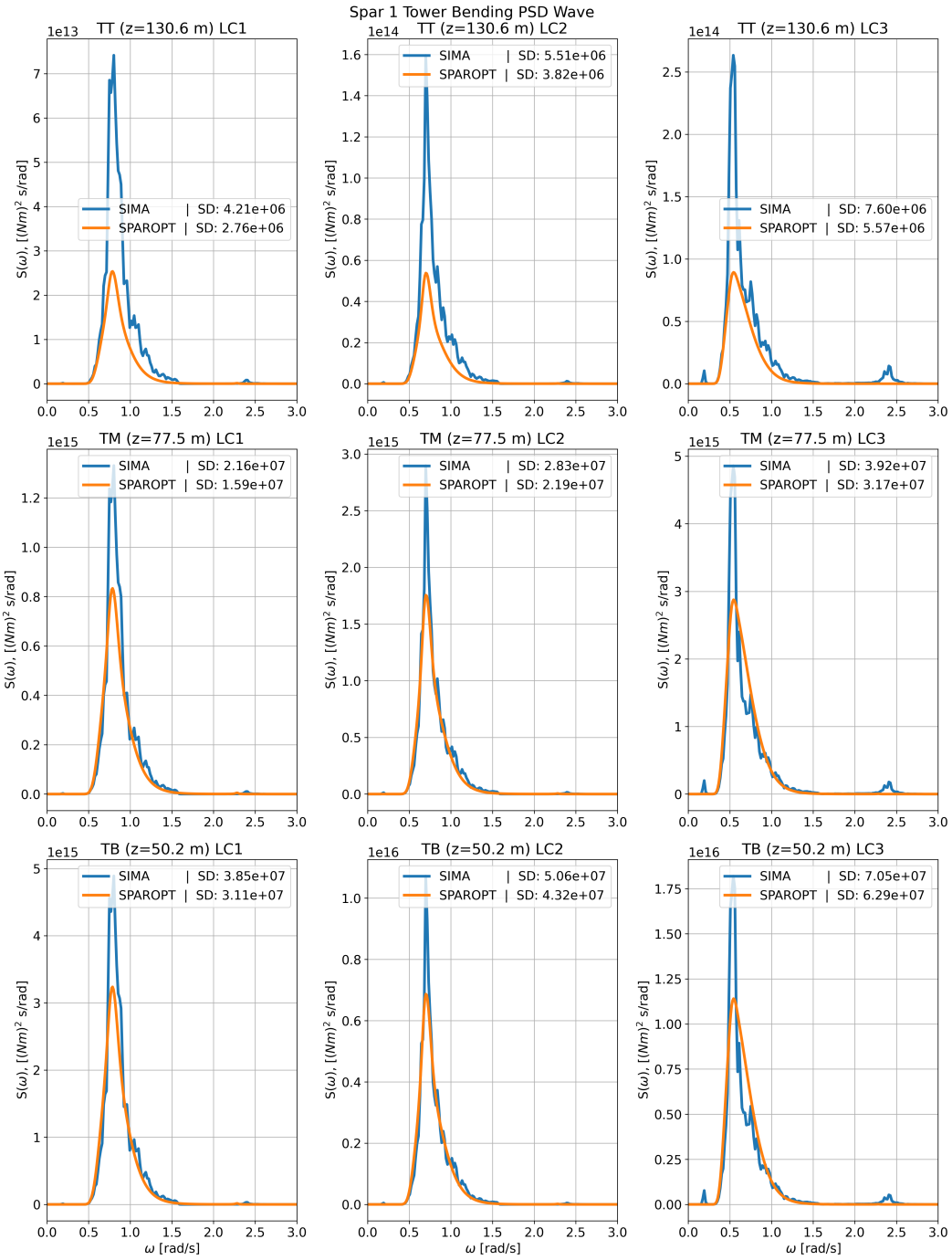

Figure .5: Spar 1 Bending Moment Tower PSD Wave

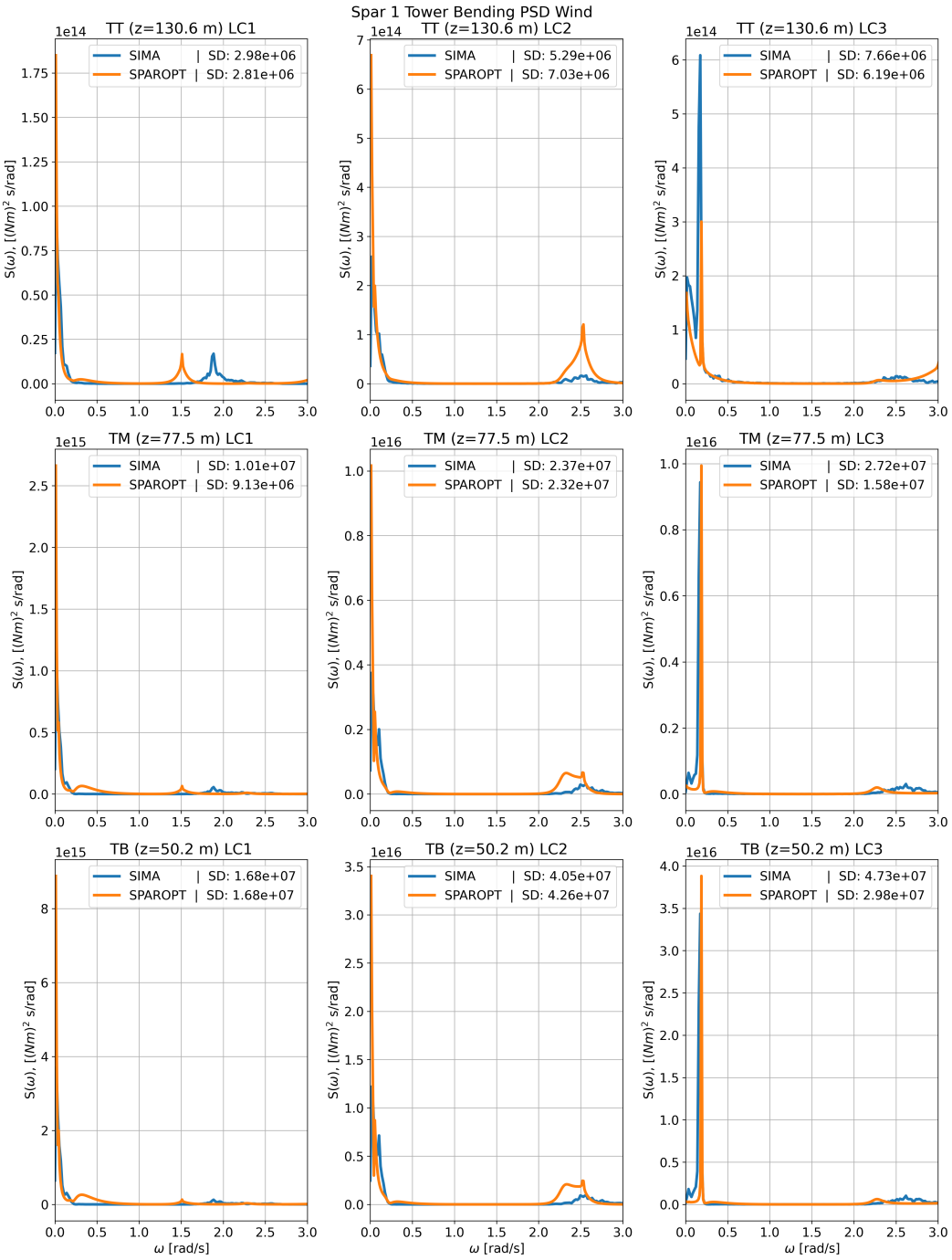

Figure .6: Spar 1 Bending Moment Tower PSD Wind

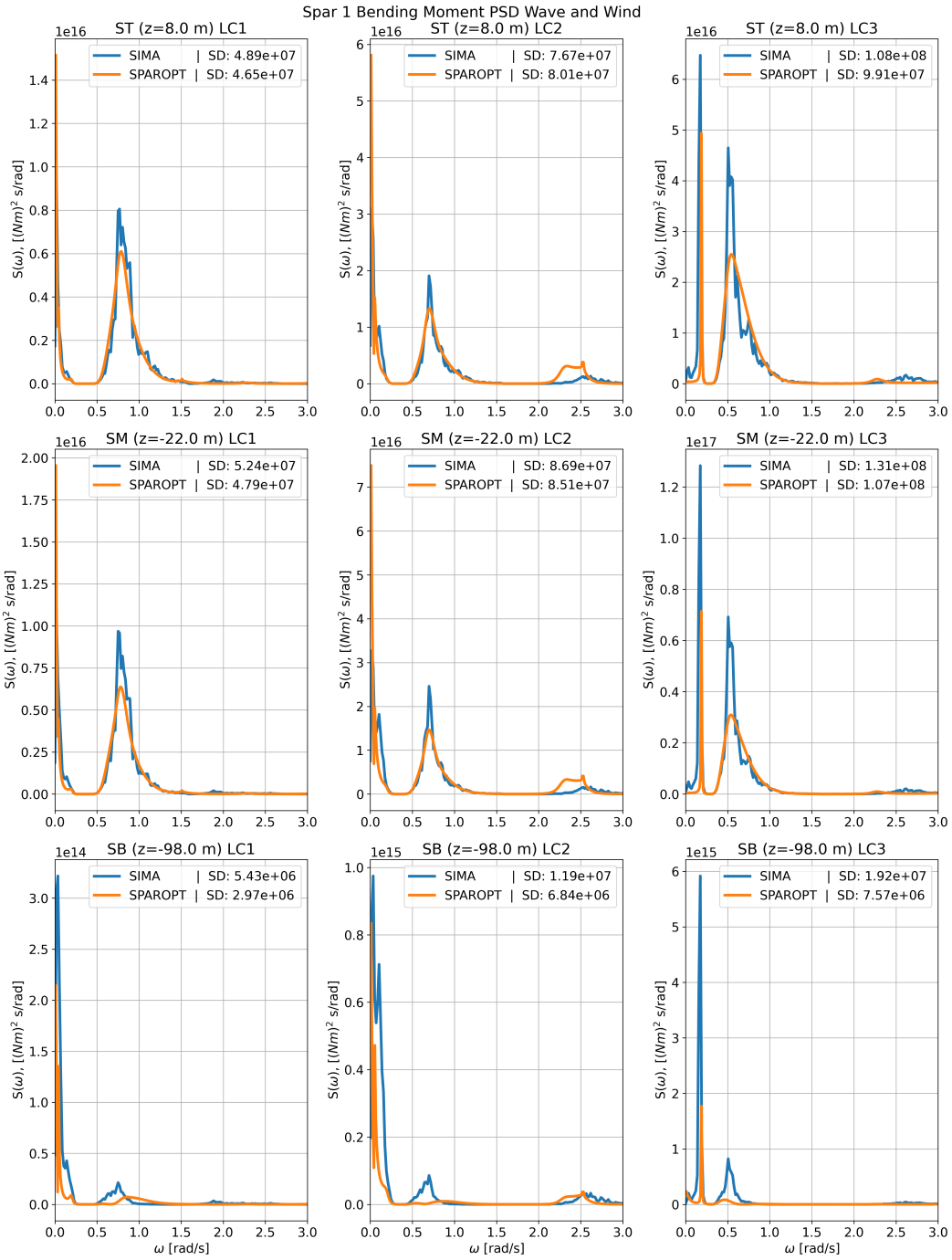

Figure .7: Spar 1 Bending Moment PSD Wave and Wind

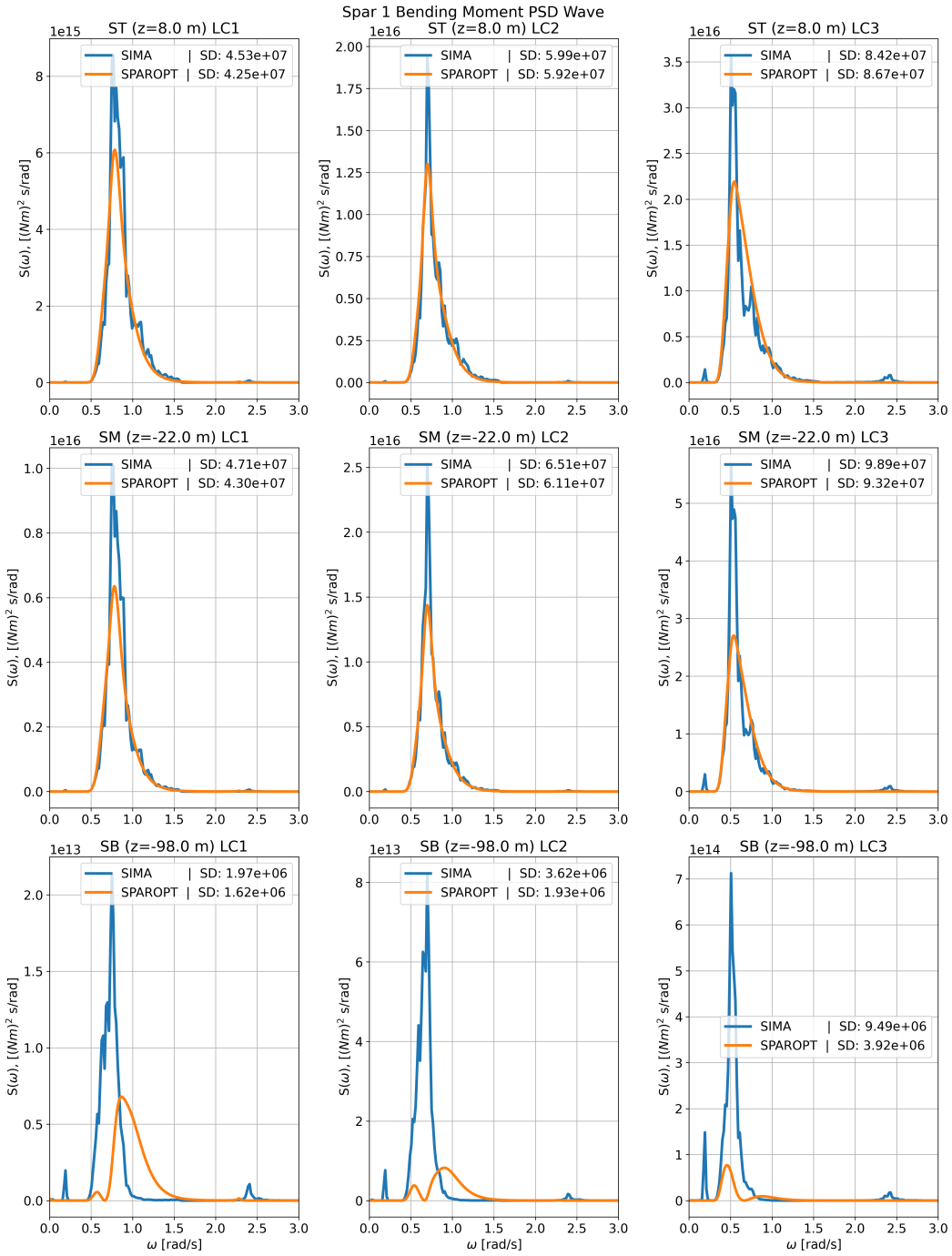

Figure .8: Spar 1 Bending Moment PSD Wave

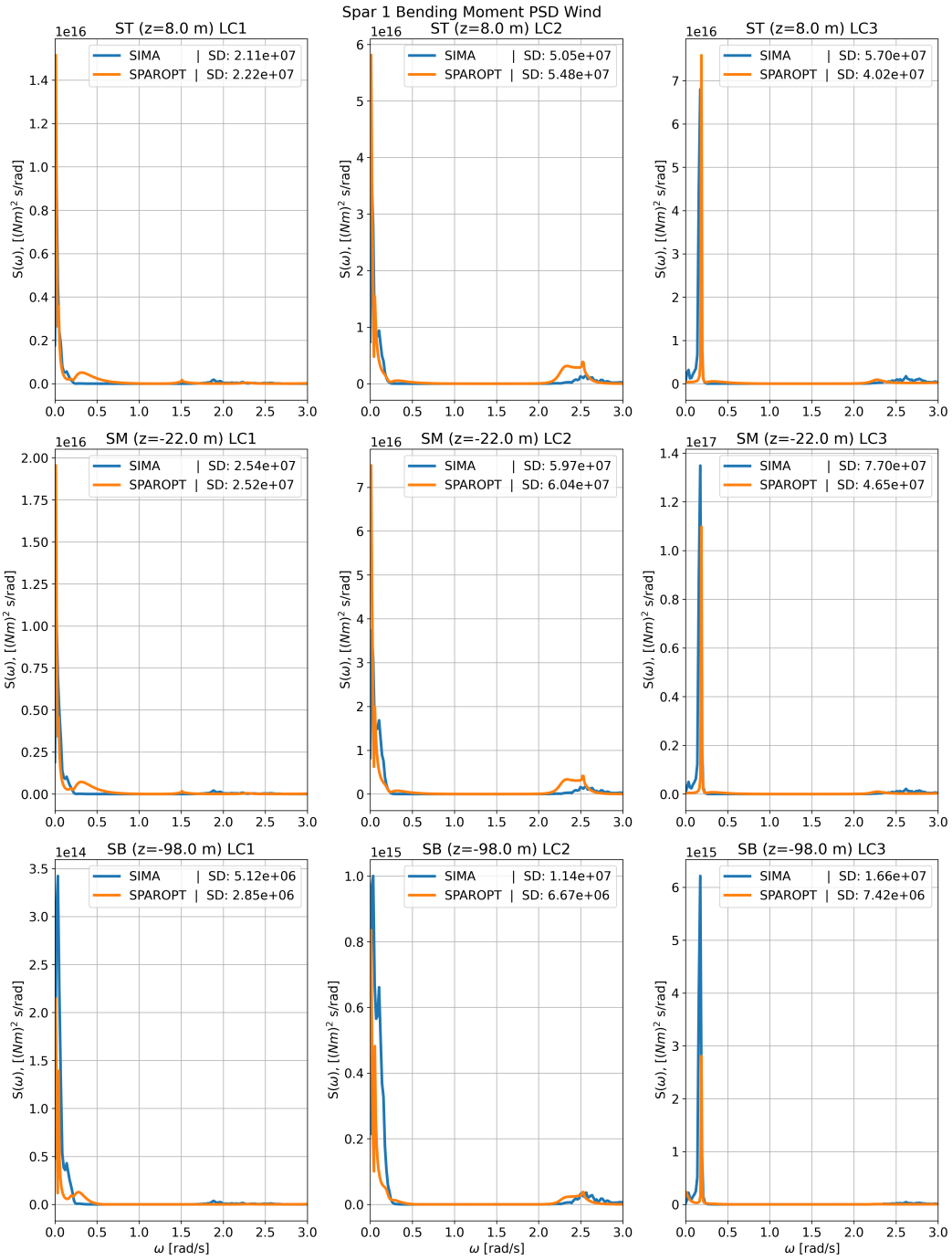

Figure .9: Spar 1 Bending Moment PSD Wind

A.2 SPAR 2 Wind and Wave, Wave-only, Wind only

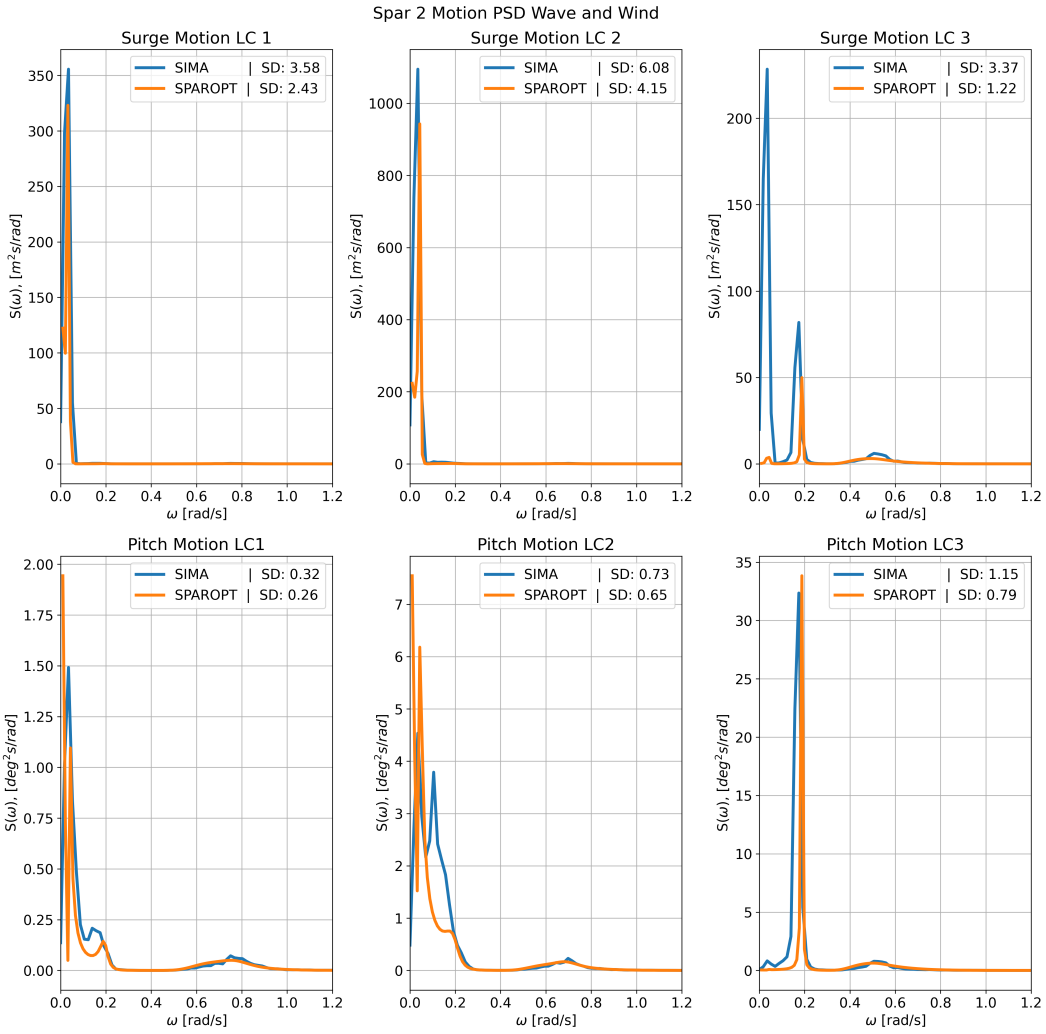

Figure .10: Spar 2 Motion PSD Wave and Wind

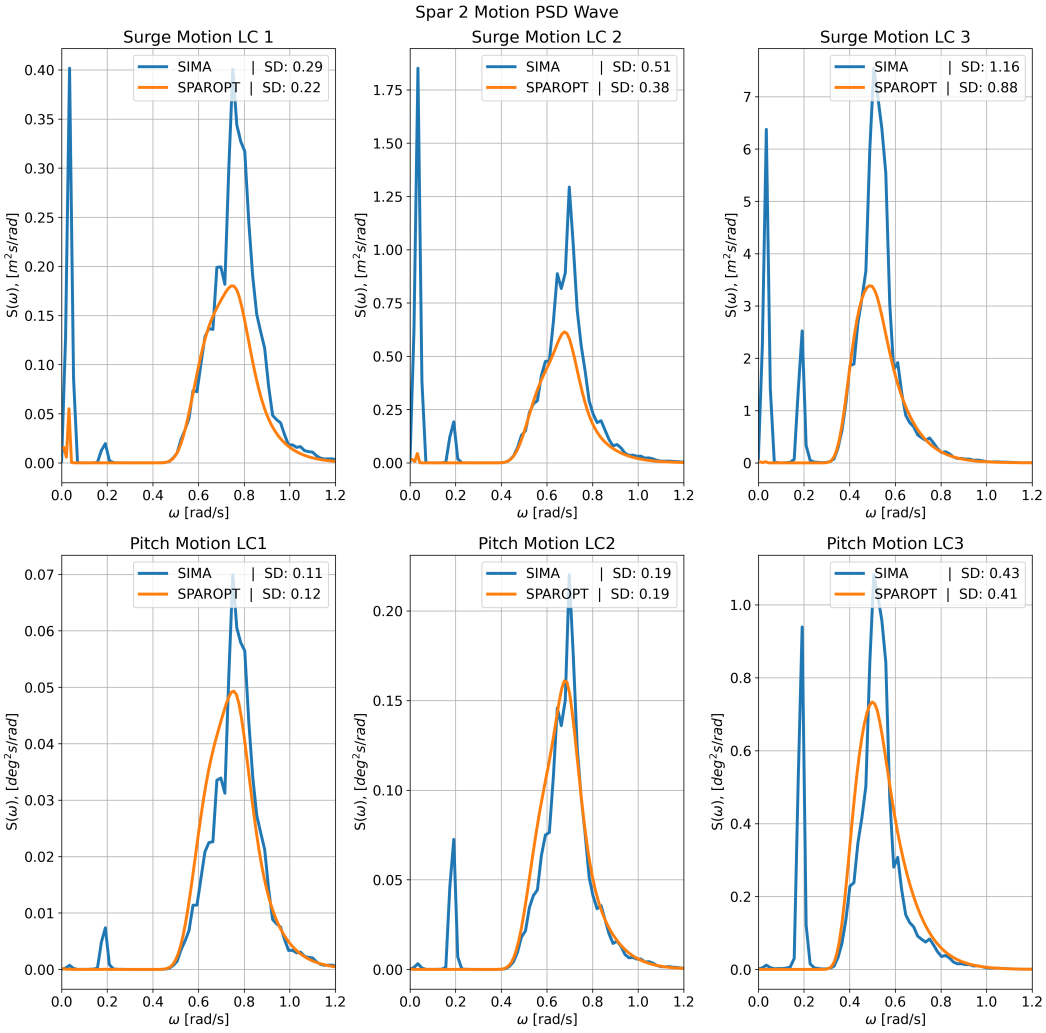

Figure .11: Spar 2 Motion PSD Wave

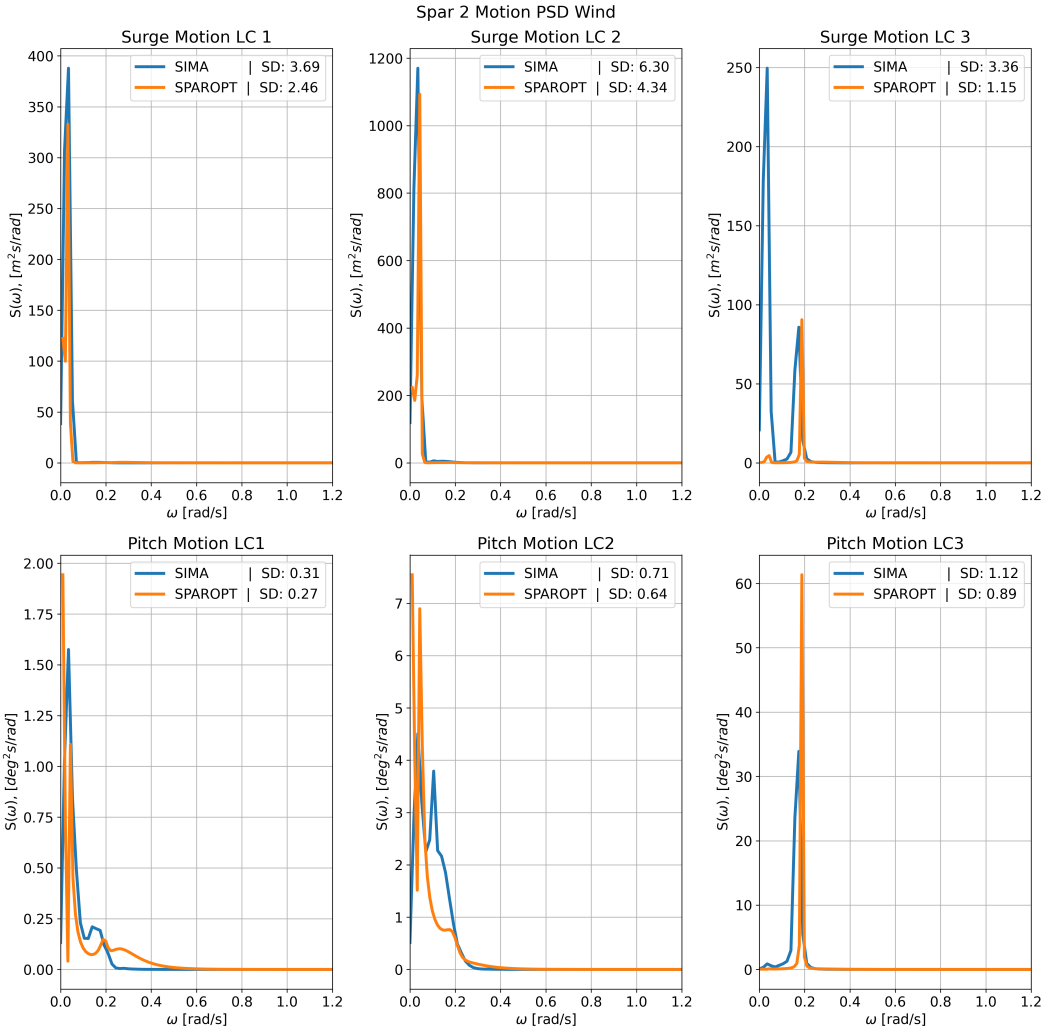

Figure .12: Spar 2 Motion PSD Wind

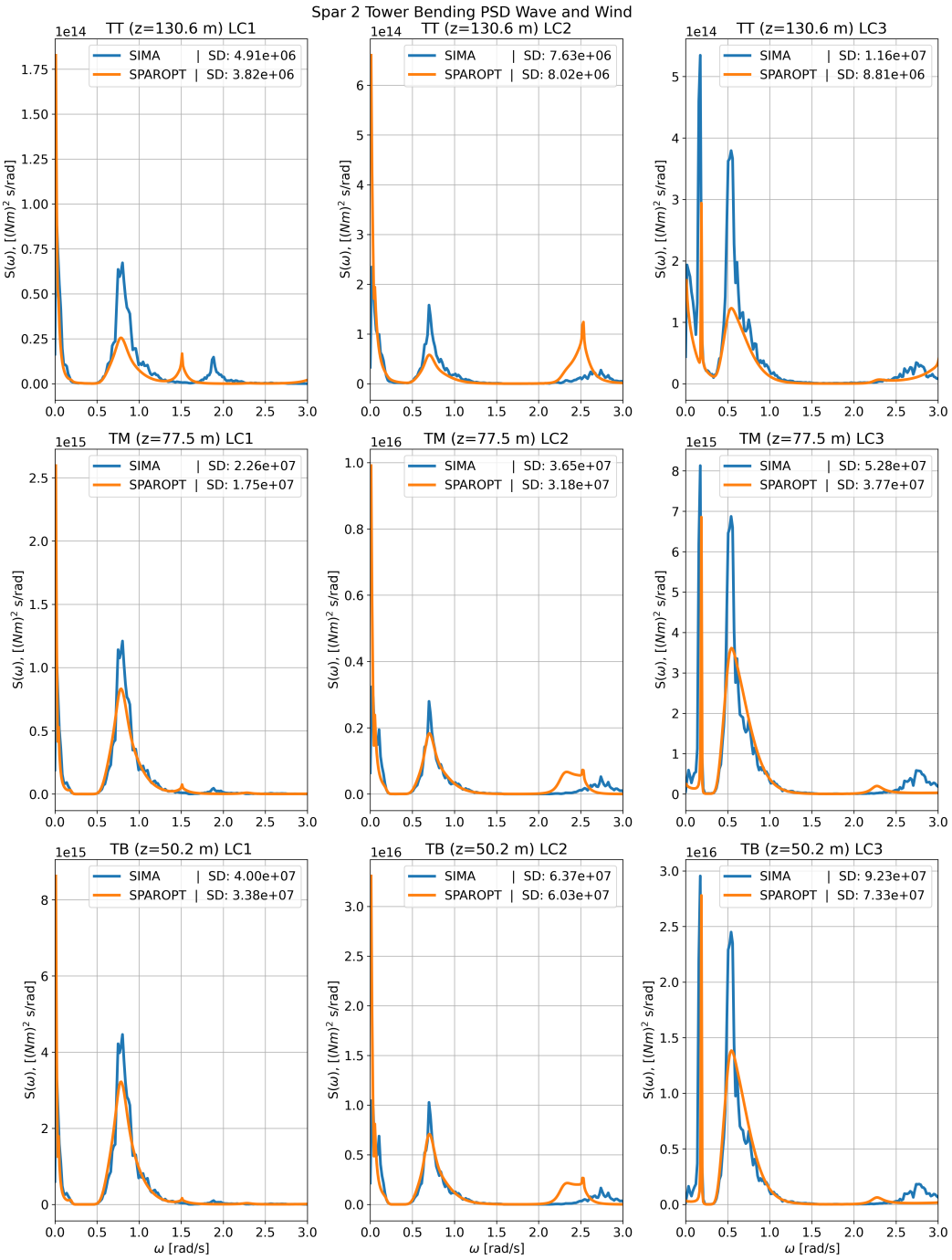

Figure .13: Spar 2 Bending Moment Tower PSD Wave and Wind

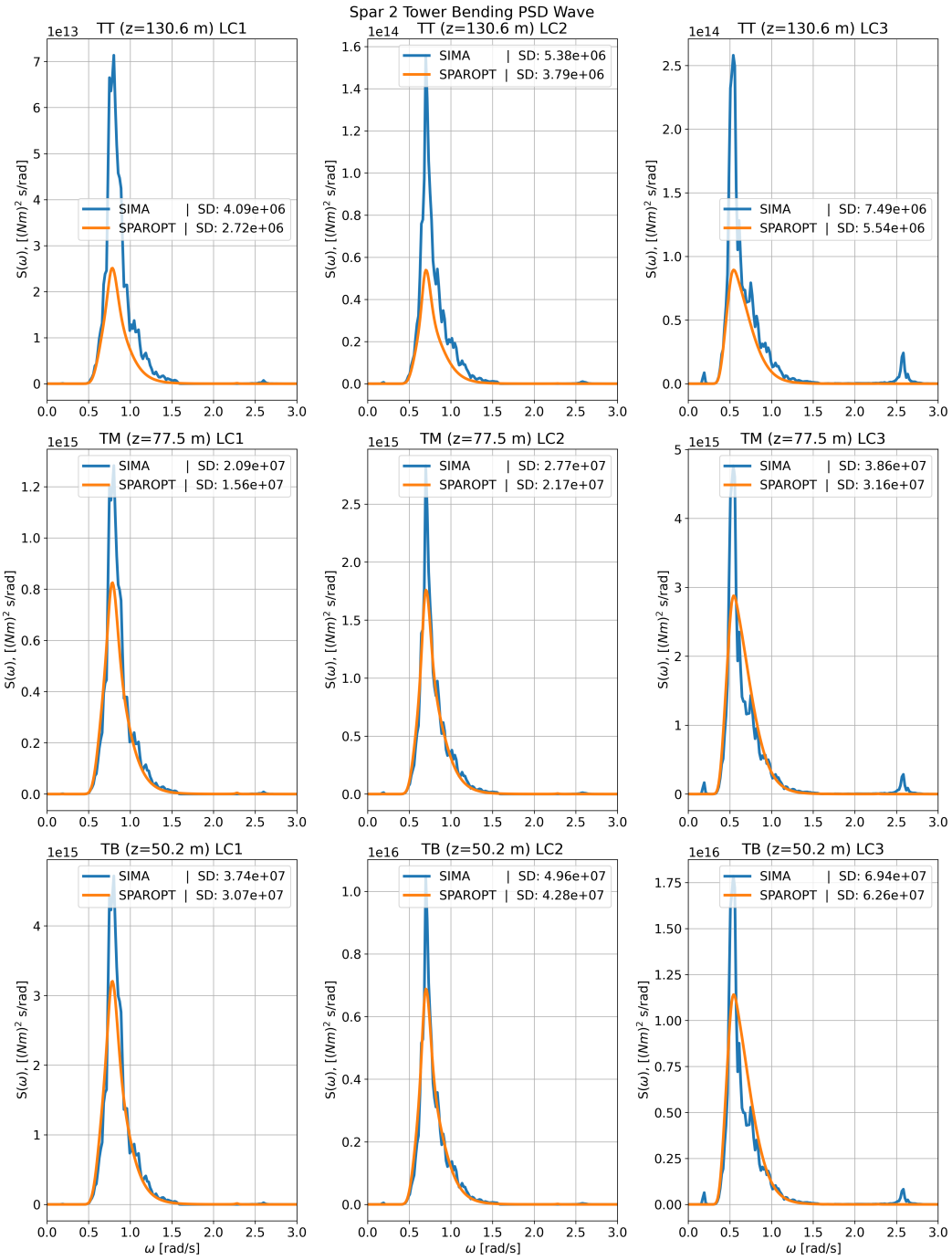

Figure .14: Spar 2 Bending Moment Tower PSD Wave

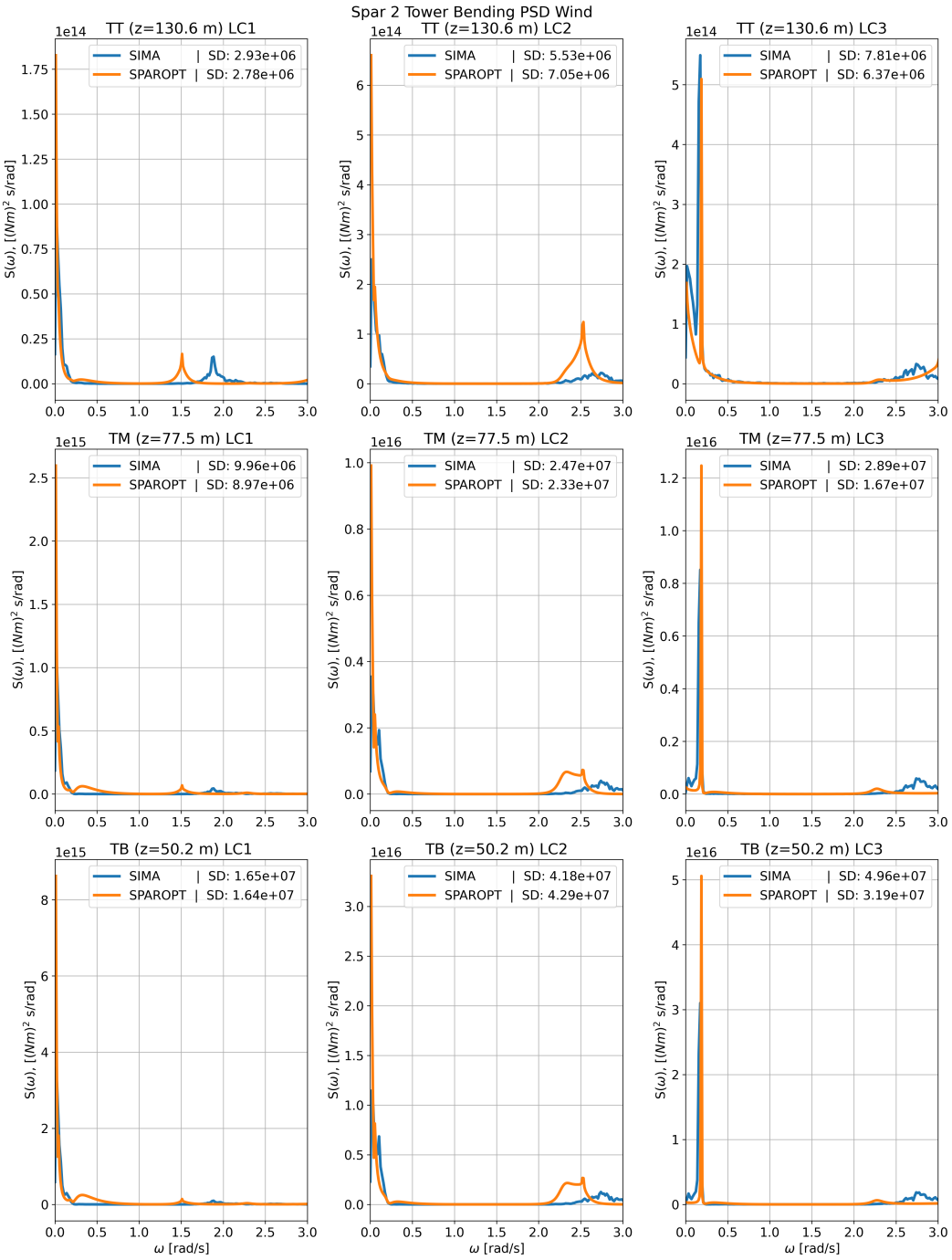

Figure .15: Spar 2 Bending Moment Tower PSD Wind

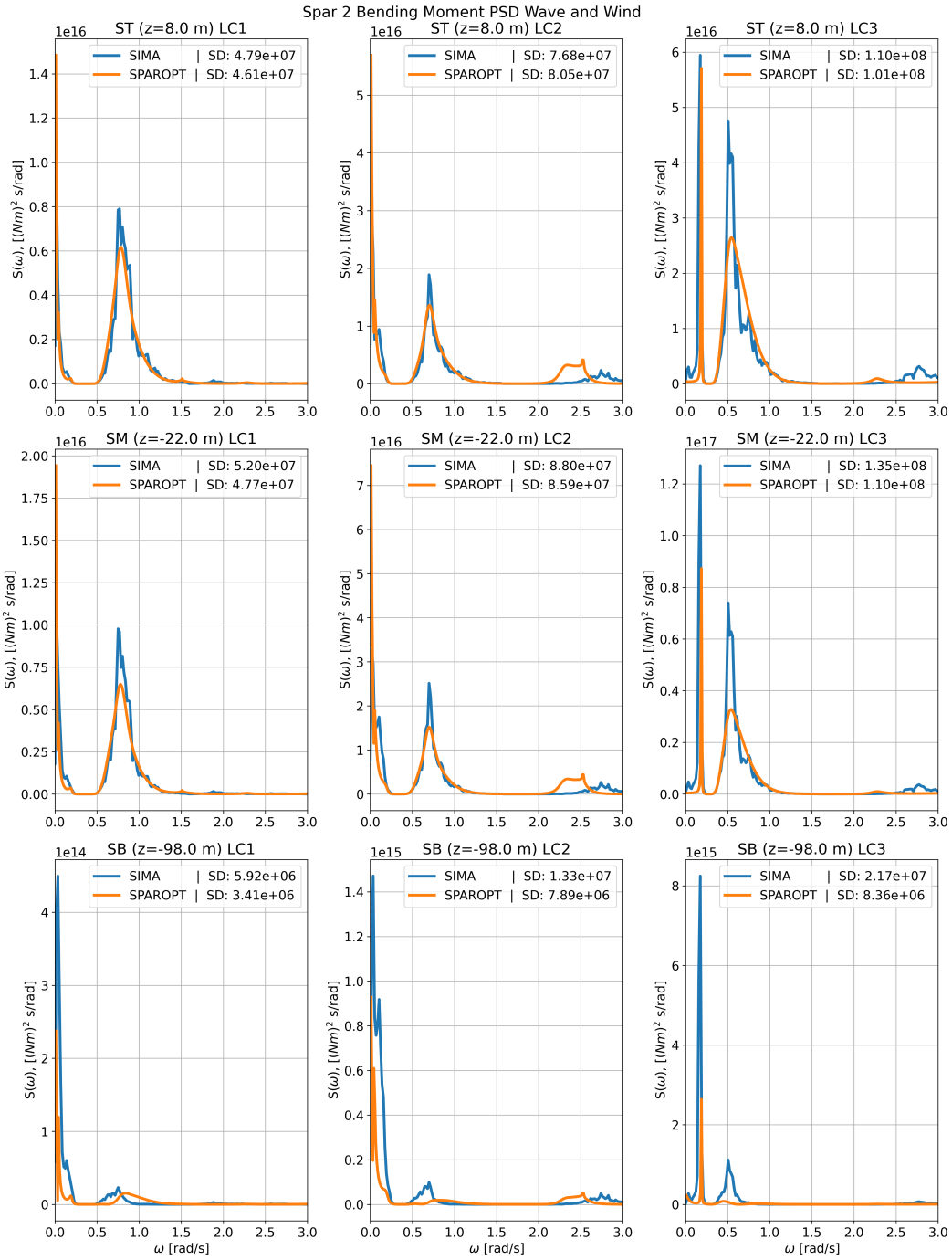

Figure .16: Spar 2 Bending Moment PSD Wave and Wind

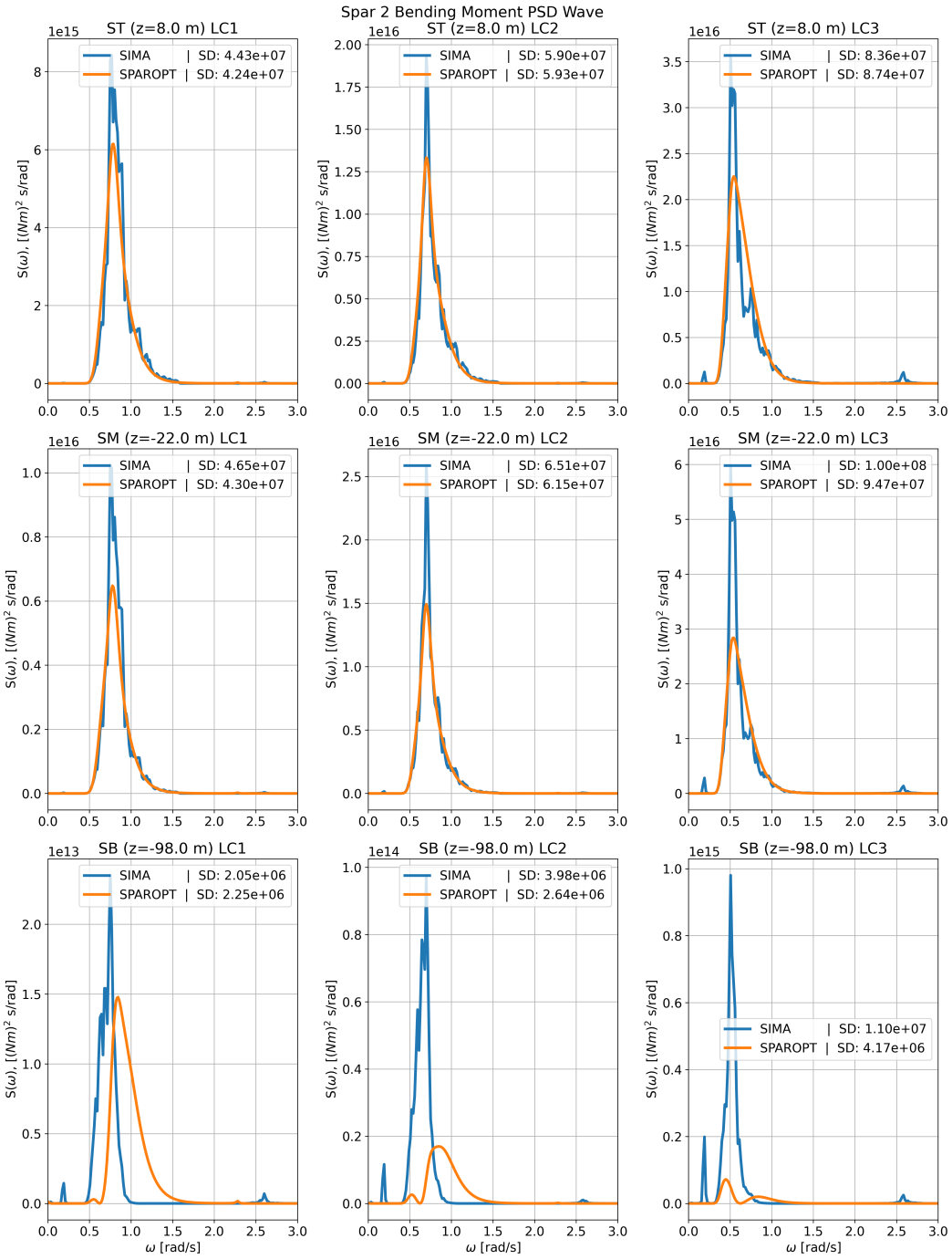

Figure .17: Spar 2 Bending Moment PSD Wave

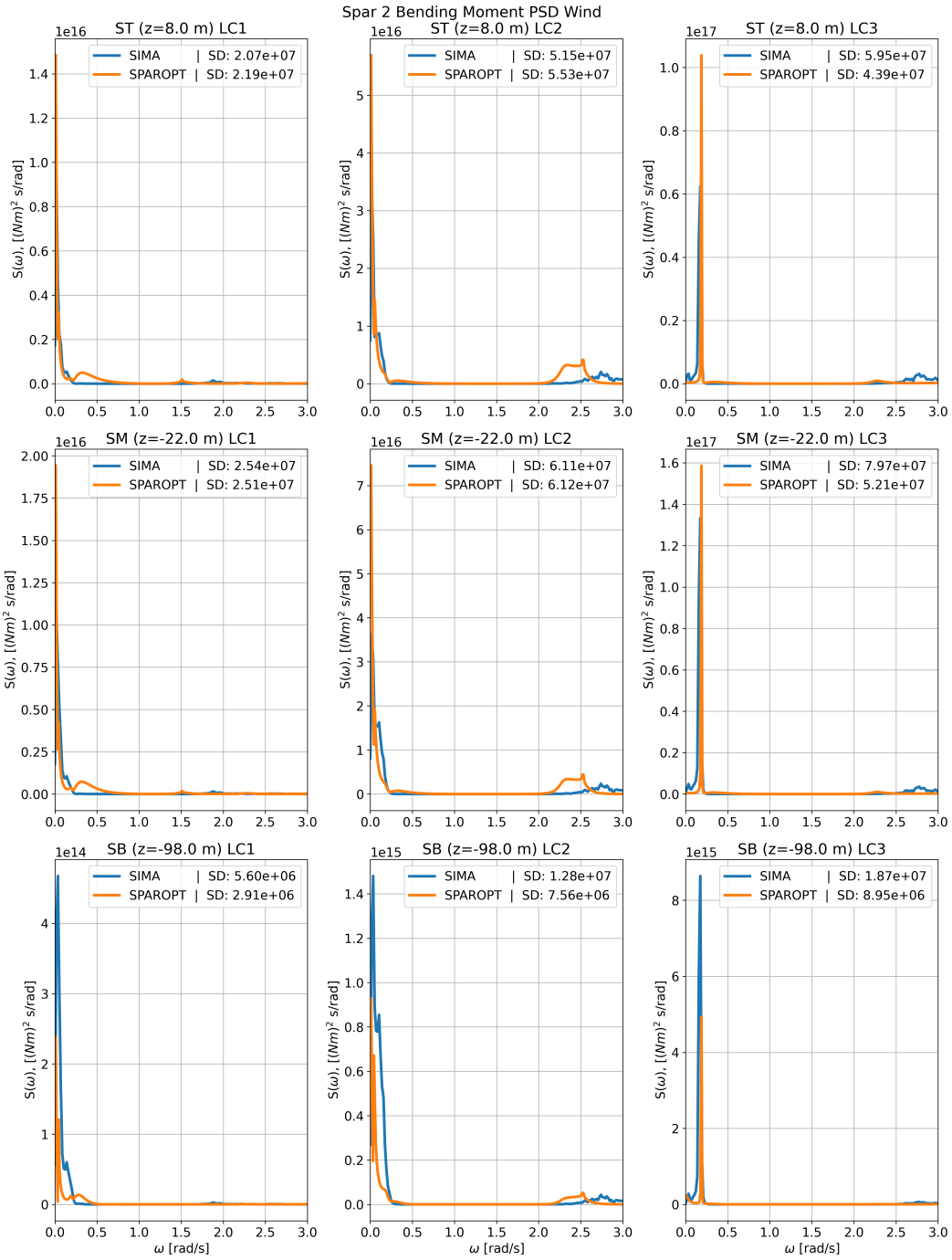

Figure .18: Spar 2 Bending Moment PSD Wind

B Concrete Capacity Contour Plots

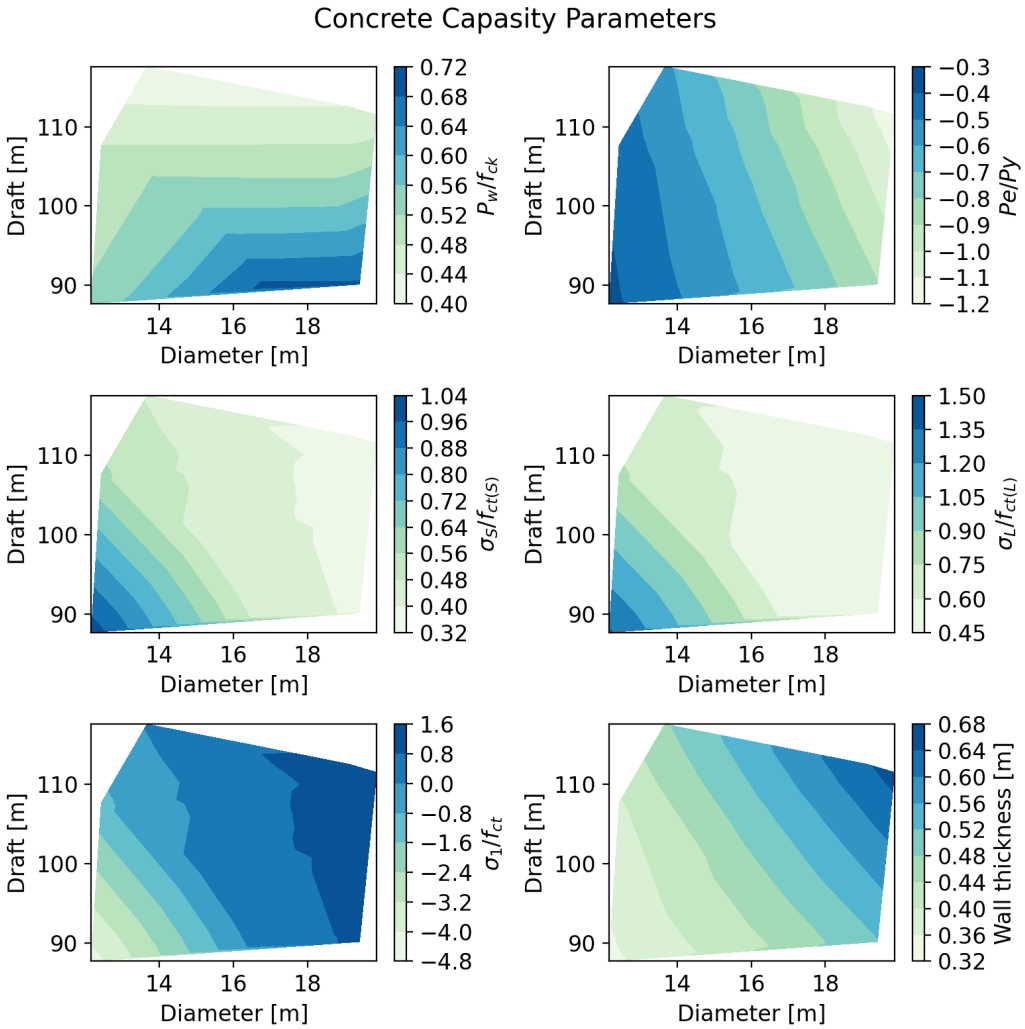

Figure .19: Design exploration when considering concrete capacity.

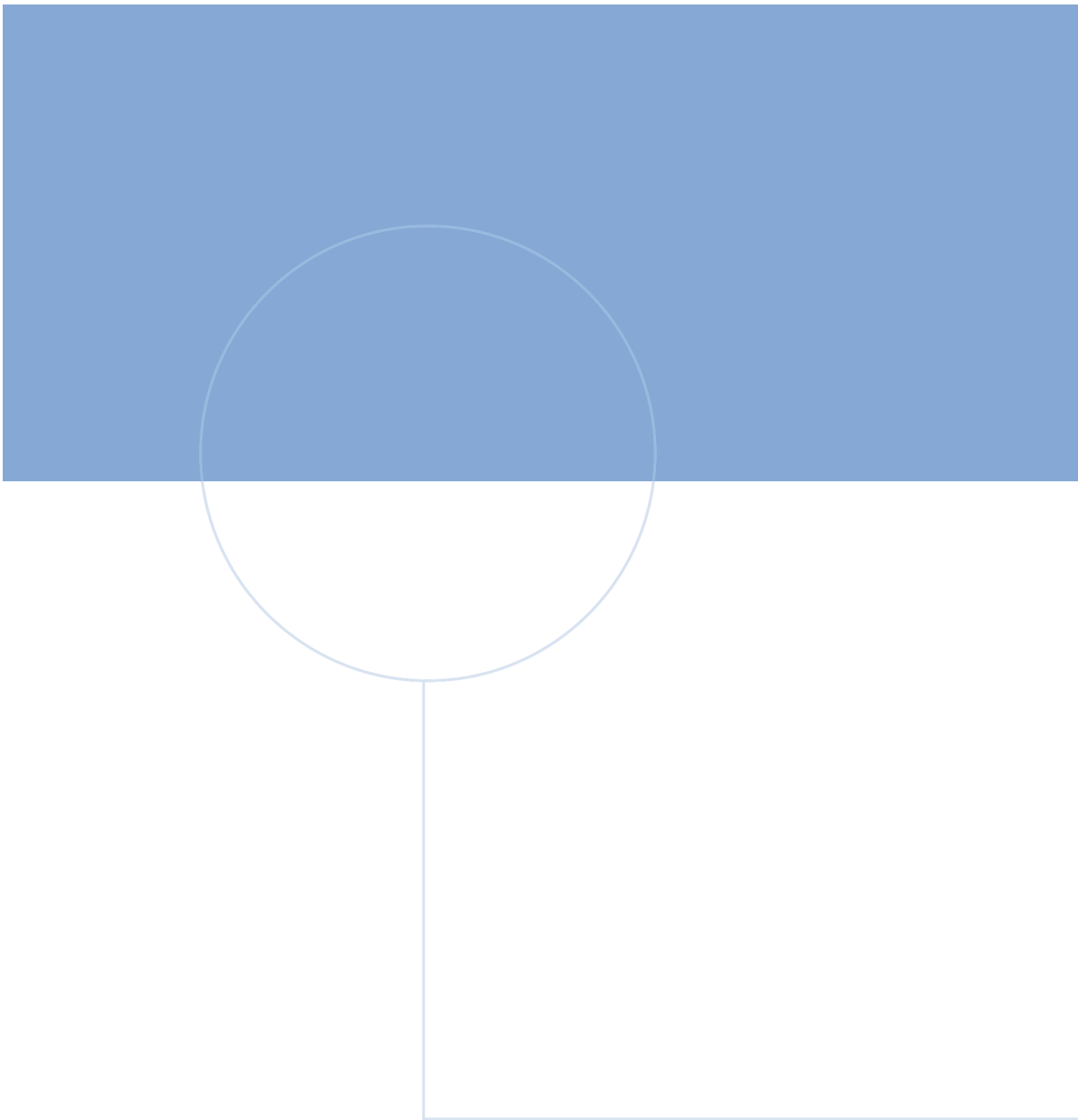

NTNU

Norwegian University of
Science and Technology